7-2021

An Enhanced Statistical Phonon Transport Model for Nanoscale Thermal Transport and Design

Michael P. Medlar
mpmmet@rit.edu

RIT

An Enhanced Statistical Phonon Transport Model for Nanoscale Thermal Transport and Design

By

Michael P. Medlar

A dissertation submitted in partial fulfillment of the requirements for the degree of Doctor of Philosophy in Engineering

Engineering PhD Program
Kate Gleason College of Engineering

Rochester Institute of Technology
Rochester, New York
July, 2021

An Enhanced Statistical Phonon Transport Model for Nanoscale Thermal Transport and Design
By
Michael P. Medlar

Committee Approval:

We, the undersigned committee members, certify that we have advised and/or supervised the candidate on the work described in this dissertation. We further certify that we have reviewed the dissertation manuscript and approve it in partial fulfillment of the requirements of the degree of Doctor of Philosophy in Engineering.

Dr. Edward C. Hensel (Advisor) Date
Director, PhD in Engineering

Dr. Risa J. Robinson Date
Department Head, Mechanical Engineering

Dr. Michael Schertzer Date
Associate Professor, Mechanical Engineering

Dr. Stefan Preble Date
Professor, Electrical and Microelectronic Engineering

Dr. Nathan Eddingsaas Date
Associate Professor, Chemistry and Materials Science

Certified by:

Dr. Edward Hensel Date
Director, PhD in Engineering

Curriculum Vitae

Michael P. Medlar
mpmmet@rit.edu

Professional Preparation

- Rochester Institute of Technology, Rochester, New York, Mechanical Engineering B.S. 2002
- Rochester Institute of Technology, Rochester, New York, Mechanical Engineering M.S. 2002

Appointments

- Senior Lecturer, Rochester Institute of Technology 2015 - Present
  - Taught classes in the areas of mechanics, materials, and thermal fluids.
  - Participated in department level service
- Lecturer, Rochester Institute of Technology 2010 - 2015
  - Taught classes in the areas of mechanics, materials, and thermal fluids.
  - Participated in department level service
- Adjunct Instructor, Hudson Valley Community College 2008 - 2010
  - Taught classes in materials science
  - Participated on industrial advisory board
- Engineer, Knolls Atomic Power Laboratory 2003 - 2010
  - Performed thermal/hydraulic analysis of nuclear reactors in support of nuclear reactor design. Sponsored thermal/hydraulic experiments and analyzed data. Improved the predictive capability of computational thermal/hydraulic tools. Prepared technical reports for government personnel. Prepared and gave technical presentations to the General Manager, government personnel and design review committees. Mentored new employees. Lectured to new employees in the area of thermal/hydraulic testing.
- Co-op Engineer, IBM 1999 - 2000
  - Developed productivity and capability improvements for Micro-via Mechanical Drilling Machines for the drilling of printed circuit boards. Prepared process specifications for various machines used in the production of printed circuit boards. Prepared and gave technical presentations to management.

Publications

- Medlar, M. P., and Hensel, E. C., 2020, "Validation of an Enhanced Dispersion Algorithm for Use with the Statistical Phonon Transport Model," Proc. ASME 2020 Heat Transfer Summer Conference collocated with the ASME 2020 Fluids Engineering Division Summer Meeting and the ASME 2020 18th International Conference on Nanochannels, Microchannels, and Minichannels, ASME 2020 Heat Transfer Summer Conference.
- Medlar, M. P., and Hensel, E. C., 2020, "Validation of a Physics Based Three Phonon Scattering Algorithm Implemented in the Statistical Phonon Transport Model," Proc. ASME 2020 International Mechanical Engineering Congress and Exposition, Volume 11: Heat Transfer and Thermal Engineering.

- Medlar, M.P., 2002, Analysis of the Droplet Size Reduction in a PMDI Due to the Addition of a Turbulence Generating Nozzle. Master's Thesis. Rochester Institute of Technology.

Synergistic Activities/Awards

- Curriculum development for the MMET undergraduate curriculum.
- Supported students at department level events and open houses.
- CAST Distinguished Lecturer 2015.

Technical Abstract

Managing thermal energy generation and transfer within the nanoscale devices (transistors) of modern microelectronics is important as it limits speed, carrier mobility, and affects reliability. Application of Fourier's Law of Heat Conduction to the small length and times scales associated with transistor geometries and switching frequencies doesn't give accurate results due to the breakdown of the continuum assumption and the assumption of local thermodynamic equilibrium. Heat conduction at these length and time scales occurs via phonon transport, including both classical and quantum effects. Traditional methods for phonon transport modeling are lacking in the combination of computational efficiency, physical accuracy, and flexibility. The Statistical Phonon Transport Model (SPTM) is an engineering design tool for predicting non-equilibrium phonon transport. The goal of this work has been to enhance the models and computational algorithms of the SPTM to elevate it to have a high combination of accuracy and flexibility. Four physical models of the SPTM were enhanced. The lattice dynamics calculation of phonon dispersion relations was extended to use first and second nearest neighbor interactions, based on published interatomic force constants computed with first principles Density Functional Theory (DFT). The computation of three phonon scattering partners (that explicitly conserve energy and momentum) with the inclusion of the three optical phonon branches was applied using scattering rates computed from Fermi's Golden Rule. The prediction of phonon drift was extended to three dimensions within the framework of the previously established methods of the SPTM. Joule heating as a result of electron-phonon scattering in nanoscale electronic devices was represented using a modal specific phonon source that can be varied in space and time. Results indicate the use of first and second nearest neighbor lattice dynamics better predicted dispersion when compared to experimental results and resulted in a higher fidelity representation of phonon group velocities and three phonon scattering partners in an anisotropic manner. Three phonon scattering improvements resulted in enhanced fidelity in the prediction of phonon modal decay rates across the wavevector space and thus better representation of non-equilibrium behavior. Comparisons to the range of phonon transport modeling approaches from literature verify that the SPTM has higher phonon fidelity than Boltzmann Transport Equation and Monte Carlo and higher length scale and time scale fidelity than Direct Atomic Simulation. Additional application of the SPTM to both a 1-d silicon nanowire transistor and a 3-d FinFET array transistor in a transient manner illustrate the design capabilities. Thus, the SPTM has been elevated to fill the gap between lower phonon fidelity Monte Carol (MC) models and high fidelity, inflexible direct quantum simulations (or Direct Atomic Simulations (DAS)) within the field of phonon transport modeling for nanoscale electronic devices. The SPTM has produced high fidelity device level non-equilibrium phonon information in a 3-d, transient manner where Joule heating occurs. This information is required due to the fact that effective lattice temperatures are not adequate to describe the local thermal conditions. Knowledge of local phonon distributions, which can't be determined from application of Fourier's law, is important because of effects on electron mobility, device speed, leakage, and reliability.

Acknowledgements

First and foremost I would like to thank my wife Erin and my children Zackary and Nicholas for their patience and never-ending support throughout this entire endeavor. They have been there on the frustrating days with encouragement and on the exciting days with celebration. They have pretended to listen with interest to my discussions on phonon transport.

I would like to thank my parents for instilling in me the value of hard work and lifelong learning. They have promoted education throughout my life and always been my biggest fans.

I would like to express my gratitude to Dr. Hensel, my advisor, for not only his valued technical guidance but also for his career advice and willingness to take on a non-traditional graduate student. I look forward to our continued interactions.

Thank you to my committee for their time and effort in reviewing this work and providing helpful suggestions for its continued advancement.

To Rebecca Ziebarth for her help with keeping me on track and ensuring completion of all of the administrative tasks to finish my degree.

In addition, I would like to thank useful e-mail communications with Dr. Esfarjani, Dr. Sabatti, Dr. Rhyner, and Dr. Chhabria.

Table of Contents

List of Figures

List of Tables

List of Variables

a	Lattice constant, acceleration, phonon creation/annihilation operator	A	Area, amplitude, dynamical matrix element
c	Specific heat, electron creation/annihilation operator	B	Dynamical matrix element
e	Exponential function	C	Constant, silicon body thickness, dynamical matrix element
f	Body force, electron occupation number	D	Drain to source length, dynamical matrix element, deformation potential constant
g	Electron-phonon matrix element, acceleration due to gravity	E	Energy, dynamical matrix element
i	Imaginary number, unit Cartesian direction	F	Force, fin dimension, dynamical matrix element
j	Unit Cartesian direction	G	Reciprocal lattice vector, dynamical matrix element
k	Phonon wavevector, thermal conductivity, thermal diffusivity, unit Cartesian direction, Boltzmann constant	H	Hamiltonian, height, dynamical matrix element
l	Lattice vector	I	Dynamical matrix element
m	Mass, three phonon scattering partner, final electron state	K	Wavevector
n	Phonon occupation number, initial electron state	L	Gate length, point in wavevector space, dynamical matrix element
p	Pressure, order of perturbation	M	Atomic mass, dynamical matrix element
q	Electron wavevector, heat generation rate	N	Nanowire diameter, number of atoms or unit cells, normal modes, dynamical matrix element, number of phonons
r	Position vector	O	Dynamical matrix element
s	Phonon polarization	P	Probability
t	Time	Q	Heat flux, heat generation rate
u	Fluid velocity component, atomic displacement	S	Spacer thickness
v	Fluid velocity component, phonon group velocity	T	Temperature
w	Fluid velocity component	V	Velocity vector, volume, interatomic potential
x	Cartesian coordinate direction	W	Width, point in wavevector space

y	Cartesian coordinate direction
z	Cartesian coordinate direction

X	Point in wavevector space, Cartesian coordinate direction
Y	Cartesian coordinate direction
Z	Cartesian coordinate direction

α	On site or first nearest neighbor force constant
β	Second nearest neighbor force constant
δ	Second nearest neighbor force constant, delta-Dirac function
ε	Emissivity
ϕ	State vector
γ	Gruneisen-like parameter
$\hbar$	Modified Plank's constant
λ	Second nearest neighbor force constant
μ	Second nearest neighbor force constant, dynamic viscosity
ν	Second nearest neighbor force constant
ρ	Density
σ	Stefan-Boltzmann constant
τ	Shear stress
ω	Angular frequency
ψ	State vector

Φ	inter-atomic force constant (~ second derivative)
Γ	Point in wavevector space
K	Point in wavevector space
Π	inter-atomic force constant (~ first derivative)
Σ	Summation
Ψ	inter-atomic force constant (~ third derivative)

1 Introduction

Managing thermal energy generation and transfer within the nanoscale devices (particularly transistors) of modern microelectronics is an important consideration as increased device temperatures can lead to degradation or limiting of performance and failure. High temperatures can degrade performance due to decreased carrier mobility and interconnect resistivity but can also lead to premature device failure or reliability issues [1, 2]. Thermal related issues arise from the continued scaling in transistor geometries. Data on the minimum transistor feature sizes over time is illustrated with Fig. 1.

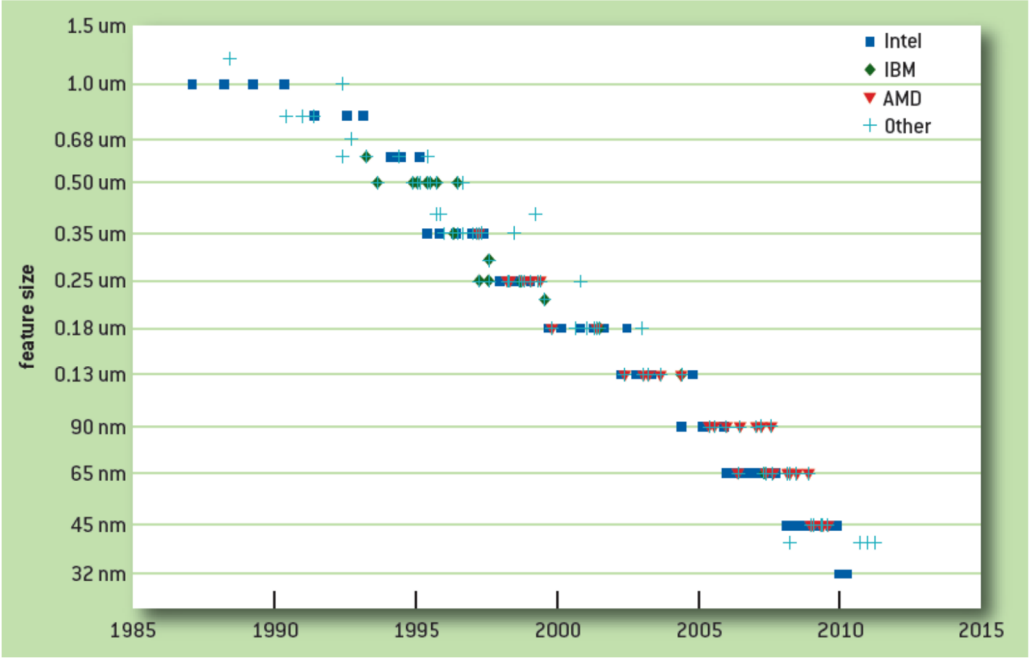

Fig. 1. Minimum transistor feature size from 1990 – 2010. Reproduced from [3].

The minimum feature size in 2010 was approximately 32 nm and according to the 2017 International Roadmap for Devices and Systems (IRDS) [4], the minimum feature size by 2027 will be 3 nm. The 1000x decrease in feature size, since the 1980's, has increased number densities of components on a given microprocessor. This increase has been in accordance with Moore's Law [5], the observation that the number of components within an integrated circuit doubled every year [6]. While initially just an observation, this trend has continued for almost 50 years. This is best illustrated with the data compiled by K. Rupp [7] shown in Fig. 2.

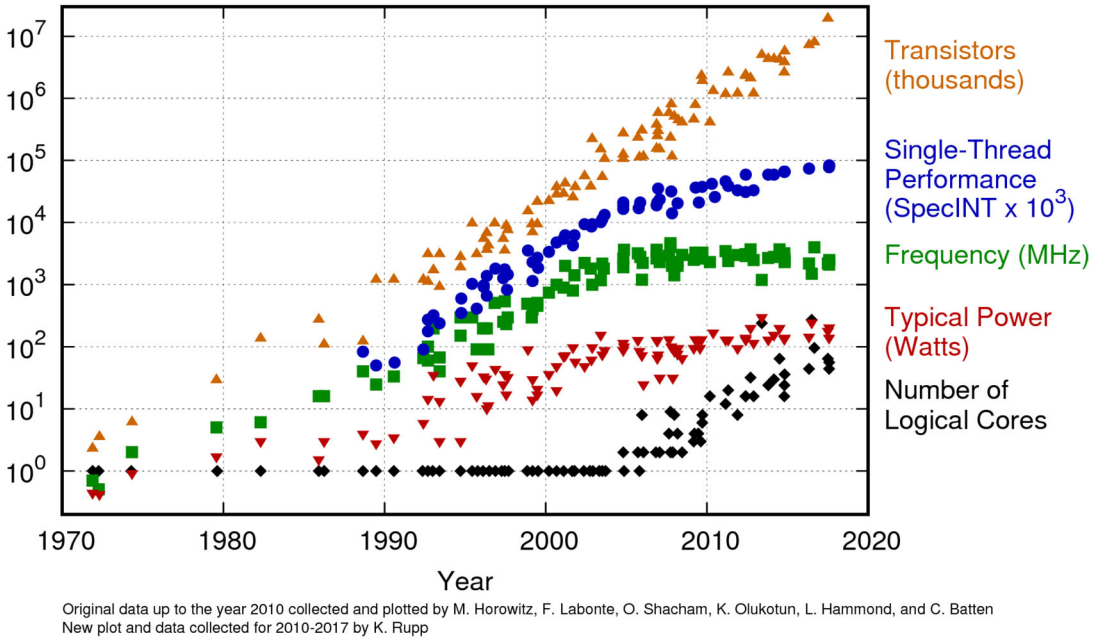

Fig. 2. Microprocessor tend data. Reproduced from [7]. Note that the units of each data set are illustrated in parentheses next to the label.

Fig. 2 demonstrates that the number of transistors has increased in accordance with Moore's Law since the 1970's. However, Single-Thread Performance, Frequency, and Typical Power has leveled off since about the late 2000's. According to the 2017 International Roadmap for Devices and Systems (IRDS), the continued scaling of transistor sizes was to the point where concurrently increasing the number of transistors and frequency of operation was no longer thermally feasible [4, 8]. Thus, operating frequency was selected as the sacrificial victim and has remained relatively constant since 2005. If operating frequency had not been artificially limited and continued to increase at the rates seen up to the late 2000's, it is estimated that current frequencies would be well over 10 GHz instead of around 2.5 - 3 GHz [4]. Mitigation of artificial frequency (and therefore) performance degradation may be achievable if accurate, flexible, and efficient design related information existed on local non-equilibrium thermal conditions. This would allow engineers to make informed decisions on sizing and material modification specifically for limiting hot spots in the basic transistor design. Information is available for engineers when it comes to simulation of charge transport on the nanoscale, but engineering design tools for nanoscale thermal transport are lacking in a high combination of accuracy, flexibility, and efficiency. It is the goal of this work to extend the Statistical Phonon Transport Model (SPTM) [9-11] to be able to fill this gap and meet the needs of designers.

1.1 Transistors

As transistors are seen as the most logical initial application of the work described in this document, their basic operation, geometry, and future evolution will be discussed. The most basic device at the heart of microelectronics is the Metal Oxide Semiconductor Field Effect Transistor (MOSFET). A typical planar MOSFET may look as is shown in Fig. 3,

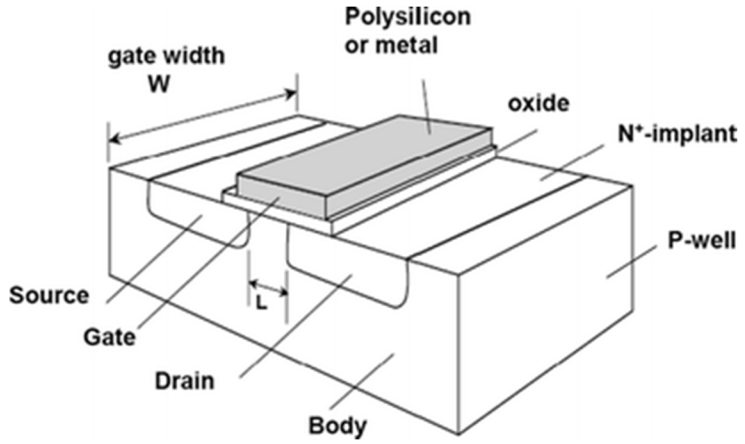

Fig. 3. Schematic of a basic N-Channel MOSFET. Reproduced from [12].

where the source and drain are N-doped (N^+-implant) silicon regions and the body of the transistor is P-doped (P-well). This implies that impurity atoms are added to the silicon in those regions to increase the charge carrier concentration. P-doping implies that the added elements creates positive charge carriers and N-doped implies negative charge carriers. Centered in between the source and drain regions is the channel (length is denoted by L) and directly above the channel is an insulating material, usually silicon oxide followed by an electrically conductive material known as the gate. When an electric potential is applied to the gate, an electric field will cause the charge carrier concentration to increase in the channel region and will allow charge to flow from the source to the drain. This switching ON/OFF characteristic of the transistor, achieved by cycling of the gate electric potential, is the building block of all digital computers. As charge carriers are transported from the source to the drain, some of their energy is transferred, as parasitic loss, to the material lattice. The parasitic loss is manifested as local heat generation and leads to hot spots in the vicinity of the channel (L) and particularly the drain region (discussed more in section 4.9.2). The geometry of the device has a direct effect on this process and the modeling discussed in this work. Changes to the basic transistor geometry are expected to occur over the next several years. The 2017 International Roadmap for Devices and Systems logic roadmap [4] predicts transition of transistor geometries from what was shown in Fig. 3 to what are termed Fully Depleted Silicon on Insulator (FD-SOI), FinFET, Lateral Nanowire, and Vertical Nanowire transistors. A schematic of this evolution is shown in Fig. 4. The critical domain for phonon transport modeling is illustrated with the text box annotations associated with each of the transistor geometries of Fig. 4. The domain is expected to evolve from a planar geometry with the FD-SOI to a rectangular rod-like geometry of the FinFET and eventually led to the cylindrical nature of the Nanowires. Different geometries pose the need for a flexible, efficient, and accurate phonon transport modeling tool.

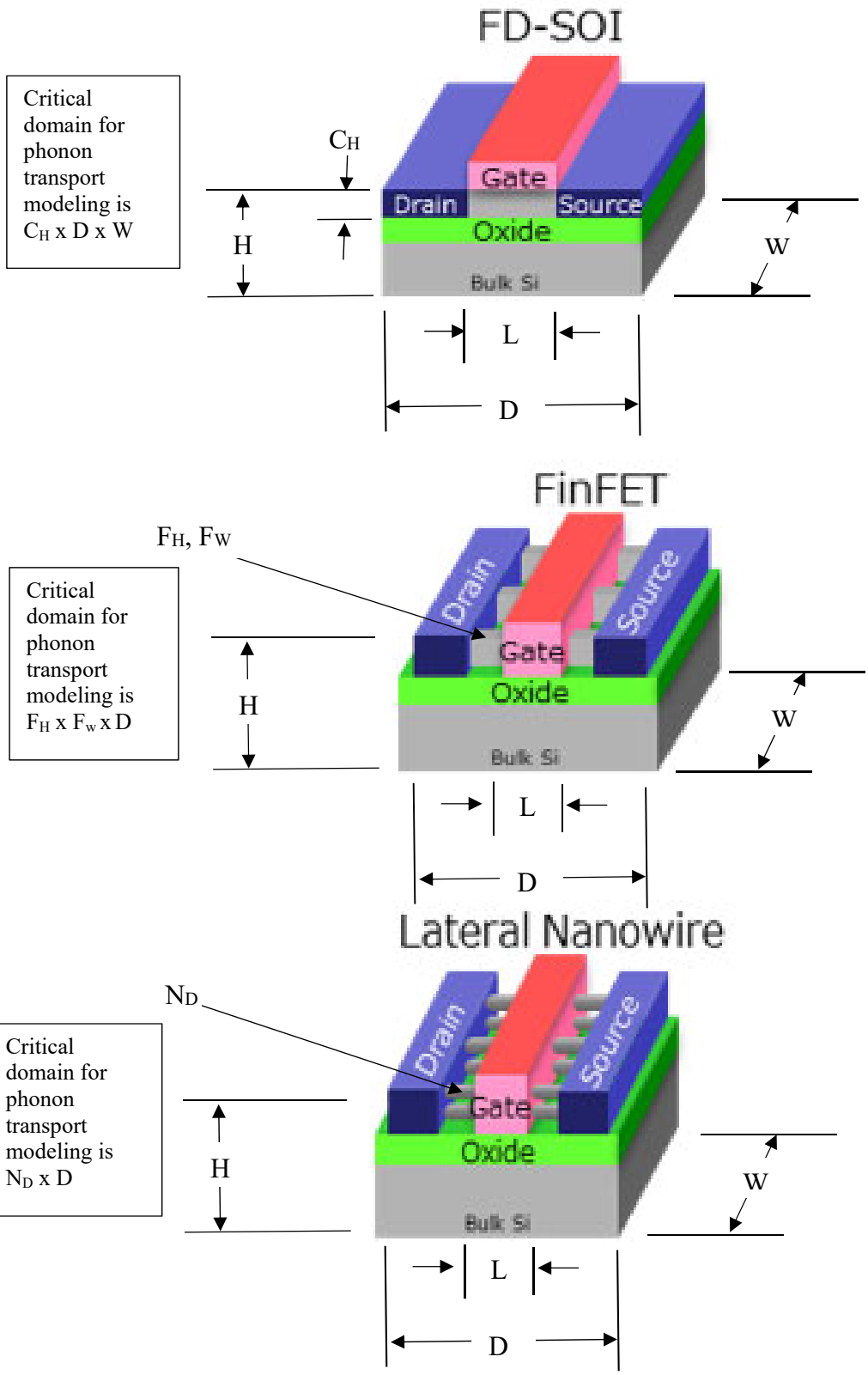
FD-SOI
Critical domain for phonon transport modeling is C_H x D x W
C_H
H
Gate
Drain
Source
Oxide
Bulk Si
W
L
D
FinFET
F_H, F_W
Critical domain for phonon transport modeling is F_H x F_w x D
H
Drain
Source
Gate
Oxide
Bulk Si
W
L
D
Lateral Nanowire
N_D
Critical domain for phonon transport modeling is N_D x D
H
Drain
Source
Gate
Oxide
Bulk Si
W
L
D

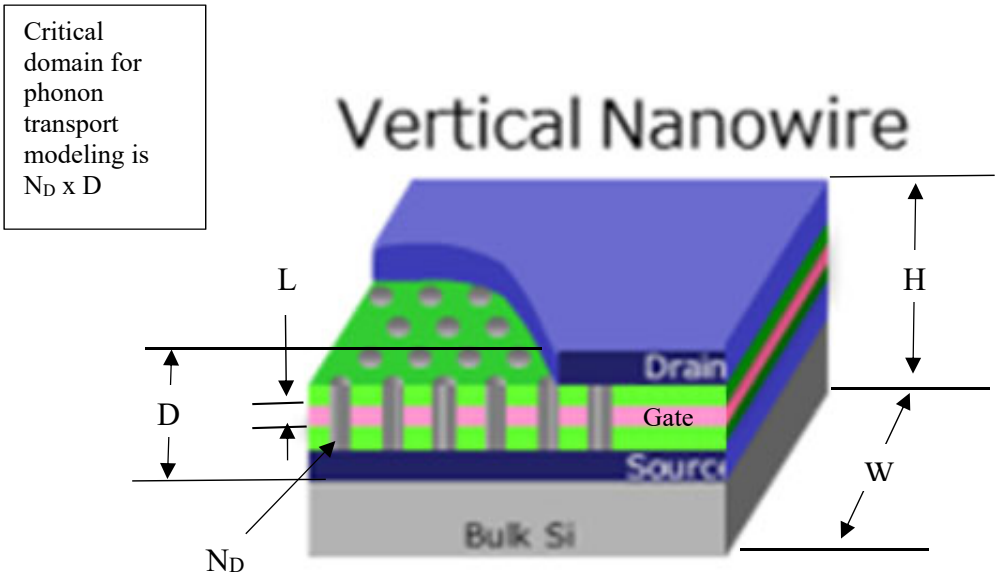

Fig. 4. Illustration of predicted transistor geometry evolution from 2017 – 2027. Adapted from [4].

In addition to changing geometries, feature sizes are projected to continue decreasing. Various feature sizes are discussed in [4] and feature dimensions are shown in Table 1.

Table 1. Predicted transistor feature sizes from 2017 - 2027 [4]

	FD-SOI	FinFET	Lateral Nanowire	Vertical Nanowire
Year of Mainstream	2017	2019	2021	2030
L_G, Gate Length, nm (Direction of Current)	20	18	16	14
D, Drain to Source Length, nm	54	48	42	24
W, Device Effective Width, nm	98	107	72	96
H, Device Effective Height, nm	45	50	47	63
C_H, Silicon Body Thickness, nm	8			
S_H, Spacer Height, nm	8	7	6	5
F_W, Fin Width, nm		7		
F_H, Fin Height, nm		50		
N_D, Nanowire Diameter, nm			7	6
Single Device Volume, nm^3	42,336	16,800	1616	678
Number of Silicon Atoms in Single Device Volume	2.11E6	8.39E56	8.07E4	3.39E4
Number of Phonons (Temperature of 500 K)	6.63E6	2.63E6	2.53E5	1.06E5

Table 1 Notes: Silicon body thickness of FD-SOI estimated from [13], Single device volume is calculated from drain to source length multiplied by a cross sectional area (either rectangular for FD-SOI and FinFET or cylindrical for nanowires), Number of silicon atoms is estimated from the number in a cubic unit cell with lattice constant of 0.5431 nm, Number of phonons is based off of SPTM calculations of 1.57E8 phonons in 100 nm cube of silicon

In addition to the relevant feature sizes, an estimate of the number of silicon atoms in the domain and the number of phonons is provided in Table 1 for later reference as they will have a direct impact on the choice of the modeling technique and motivation for the SPTM.

1.2 Macroscale Heat Transfer: Conduction, Convection, and Radiation

This dissertation deals with the modeling of heat transfer associated with the length and time scales of modern transistor geometries like those shown in section 1.1. The primary mechanism of heat transfer within solid devices, such as transistors, is conduction. A brief review of the macroscale models used to predict conduction and the other mechanisms of heat transfer will be presented. Shortcomings of these models (particularly conduction) at nanoscale sizes and picosecond time scales will be discussed as the motivation for a different modeling approach.

Conduction is the transport of thermal energy within a given medium where there is no bulk motion of the medium itself [14]. Macroscale conduction is modeled with Fourier's Law of Heat Conduction and the Heat Conduction Equation. An example application of these models in one-dimension will be detailed below as applied to heat transfer through a solid rectangular, rod-like geometry.

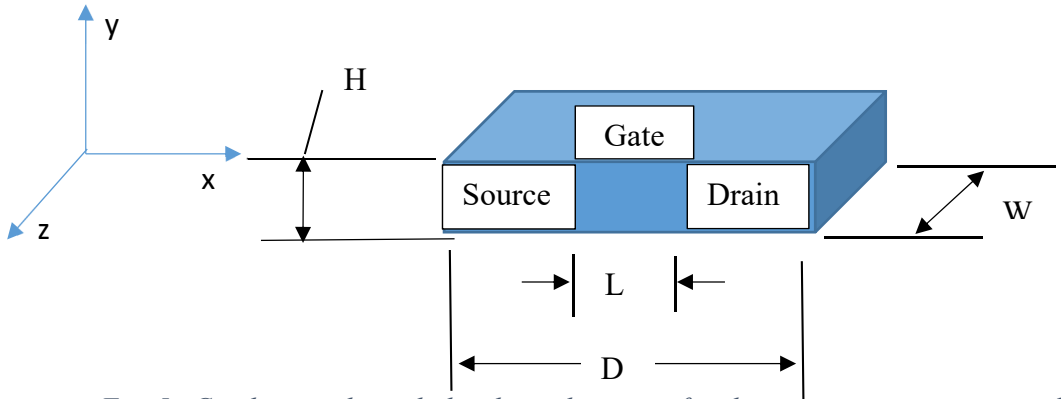

Fig. 5. Conduction through the channel region of a planar transistor represented as a solid, rectangular domain.

The rectangular geometry of Fig. 5 is similar to the geometry of the charge carrier channel in planar N-type MOSFET of Fig. 3. The left hand side of the rod is the source, the right is the drain, and the distance between is the gate length. If the transistor has a gate length on the order of 1 μm it is indicative of the scale associated with transistor dimensions representative of those produced around 1990 (See Fig. 1) and the Fourier heat conduction equation is well equipped to predict temperature distributions and heat fluxes at this length scale. If the transistor is subject to a temperature difference between the source and the drain, thermal energy will be transported through the transistor. The rate of heat transfer is directly proportional to the temperature gradient and this rate is predicted using Fourier's Law. This is shown with equation 1,

$$\dot{Q} = -kA\frac{dT}{dx} \quad , \tag{1}$$

where $\dot{Q}$ is the rate of heat transfer through the transistor in the x-direction, A is the cross sectional area, k is the thermal conductivity, and $\frac{dT}{dx}$ is the temperature gradient in the x-direction. If combined with the conservation of energy to produce the heat conduction equation, transient thermal responses can be predicted. The heat conduction equation is illustrated in one dimension with Cartesian coordinates and isotropic thermal conductivity with equation 2 [15],

$$k\frac{\partial^2 T}{\partial x^2} + \dot{q} = \rho c\frac{dT}{dt} \quad , \tag{2}$$

where $\dot{q}$ is the volumetric heat generation rate, ρ is the density of the material and c is the specific heat (for an incompressible fluid or a solid, $c = c_v = c_p$). As mentioned, the movement of charge carriers from the source to the drain leads to the generation of thermal energy within this transistor geometry. This results in a time varying internal heat generation that is a result of the transistor switching from the "on" to "off" state at the operating frequency. This is similar in nature to electrical resistance or Joule heating. At the macroscopic level it is calculated from knowledge of the current and the electric field [16]. Pop et al. [16] has shown that most of the heat generation in the transistor occurs near or in the drain. A simple method to model this effect is with a time varying heat flux boundary condition, imposed at the drain, in the form of a square wave. Equation 2 is able to predict the temperature variation as a function of time. The solution to equation 2 by means of Laplace transform (with the conditions of no heat generation, constant properties, imposed heat flux at x=L, and insulated at x=0), is shown with equation 3 [17],

$$\frac{T(x,t)-T_L}{T_H-T_L} = \sum_{n=0}^{\infty} erfc\left(\frac{C_n-x}{2\sqrt{tk_D}}\right) - erfc\left(\frac{C_n+x}{2\sqrt{tk_D}}\right), \quad (3)$$

where $T(x,t)$ is the temperature at any x location as a function of time (t), T_H is the high temperature and T_L is the low temperature, k_D is the thermal diffusivity, $C_n = (2n+1)L$, L is the length of the device, and erfc is the complementary error function. A graphical solution is shown with Fig. 6,

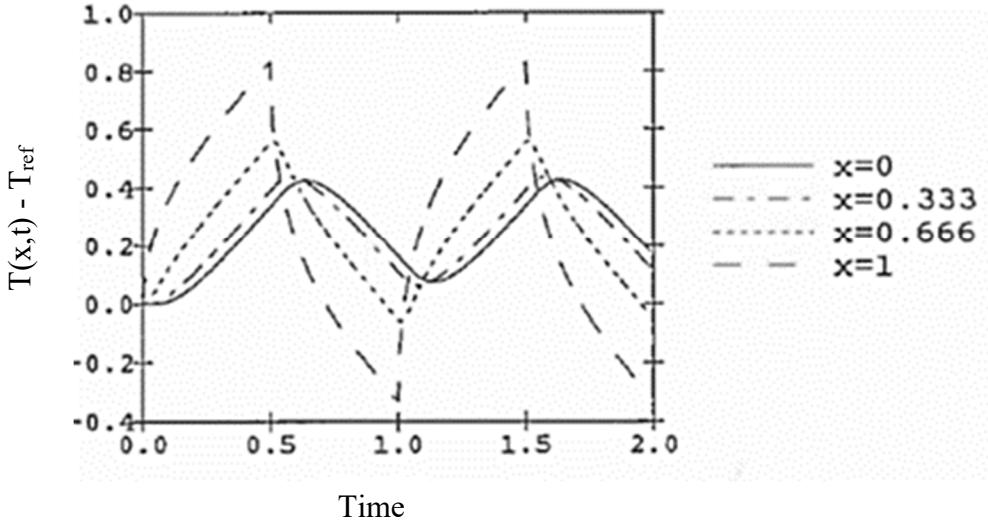

Fig. 6. 1-d transient temperature response of a rectangular rod subject to a square wave heat flux boundary condition at x=L and insulated at x=0 from solution of the heat conduction equation [9, 18, 19].

where the temperature difference as a function of time is plotted at four locations along the length of the rod. The heat flux boundary condition is implemented at a switching rate of 1 cycle per second at the x=L location. The temperature response illustrates the expected "saw tooth" pattern. In addition, the average temperature is increasing with time. The parabolic nature of the heat conduction equation is manifested as an instantaneous temperature response at any location within the rod. In reality, a finite propagation speed associated with the thermal "wave" would affect the temperature response associated with fast transients and will be represented with a nanoscale model.

Conduction modeling is focused on predicting the transport of thermal energy in the vicinity of transistor and through the bulk silicon substrate. However, ultimately that thermal energy must be removed from the microchip as a whole and transferred to a surrounding medium. This physical process is described by the heat transfer mechanism of convection. Convective heat transfer deals with the movement of thermal energy between a hot object and a relatively colder fluid by the bulk motion of the fluid. This involves conduction to the fluid in the immediate vicinity of the surface and the movement of the fluid away from the surface. The bulk motion of the fluid away from the surface can occur by density variation (buoyancy driven flow) or through externally forced means. For a simple microchip, this is illustrated with Fig. 7.

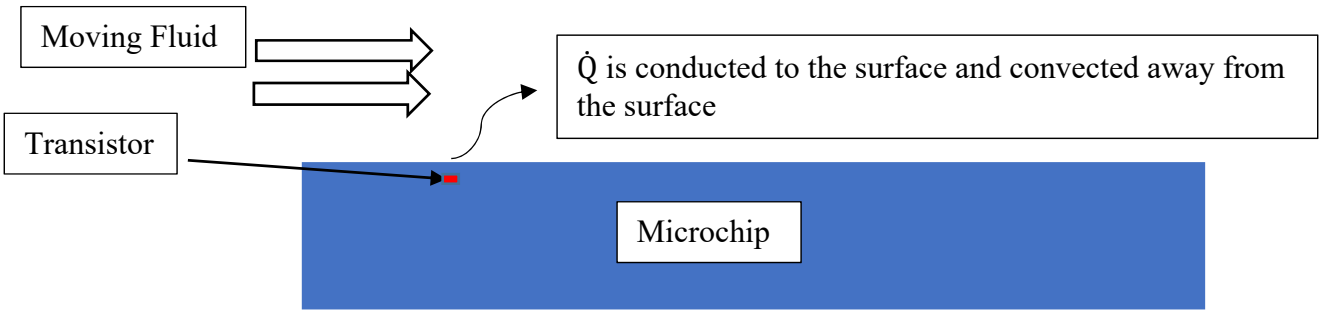

Fig. 7. Convection from microchip to a fluid showing a transistor as the most basic source of heat generation, not to scale.

Relative to microelectronics, much effort is employed to try to increase the rate at which heat can be removed by convection. Whole research groups, like those of the Thermal Analysis and Microfluidics Lab led by Dr. Kandlikar at RIT, spend much effort trying to maximize heat removal rates. To predict convective heat transfer, prediction of the conditions of the fluid adjacent to the microchip is required. That is typically done by relying on three governing equations. They are based on the three fundamental principles of the conservation of mass, momentum, and energy. These three equations are shown below [20, 21].

$$\nabla \cdot \rho \vec{V} + \frac{\partial \rho}{\partial t} = 0 \tag{4}$$

$$\frac{D(\rho \vec{V})}{Dt} = \rho \vec{g} - \nabla p + \mu \nabla^2 \vec{V} \tag{5}$$

$$\rho \frac{D}{Dt}(E) = \rho \dot{q} + \frac{\partial}{\partial x}\left(k \frac{\partial T}{\partial x}\right) + \frac{\partial}{\partial x}\left(k \frac{\partial T}{\partial x}\right) + \frac{\partial}{\partial x}\left(k \frac{\partial T}{\partial x}\right) - \frac{\partial (up)}{\partial x} - \frac{\partial (vp)}{\partial y} - \frac{\partial (wp)}{\partial z} + \frac{\partial (u\tau_{xx})}{\partial x} + \frac{\partial (u\tau_{yx})}{\partial y} + \frac{\partial (u\tau_{zx})}{\partial z} + \frac{\partial (v\tau_{xy})}{\partial x} + \frac{\partial (v\tau_{yy})}{\partial y} + \frac{\partial (v\tau_{zy})}{\partial z} + \frac{\partial (w\tau_{xz})}{\partial x} + \frac{\partial (w\tau_{yz})}{\partial y} + \frac{\partial (w\tau_{zz})}{\partial z} + \rho \vec{f} \cdot \vec{V} \tag{6}$$

$\vec{V}$ is the velocity vector (with components u, v, and w), $\vec{g}$ is the acceleration due to gravity, p is the pressure, μ is the dynamic viscosity, E is the total energy content of the fluid, τ is the shear stress components and $\vec{f}$ is the body force per unit mass. The three equations are formulated for a differential control volume and simultaneous solution would be able to predict heat transfer from the surface of a microchip.

Relative to heat transfer within microelectronics, the mechanism of radiation is not typically considered, however, the modeling of radiation transport between two surfaces where a participating media exists can draw direct analogy to the nanoscale modeling of heat conduction and thus will be discussed in brief. Radiation is electromagnetic (E/M) waves or particles

emitted from matter because atoms are in excited states. Thermal radiation is the transport of energy from/to an object by E/M waves because of the temperature of the object. As E/M waves carry a discrete amount of energy called the photon, radiative transport is due to photon transport. Most thermal radiation is in infrared spectrum (300 GHz – 430 THz). To predict the rate of heat transfer due to thermal radiation emitted from a gray surface, a relatively simple expression called Stefan-Boltzmann law is applicable. This is shown in equation 7,

$$\dot{Q} = \varepsilon\sigma T^4 \quad , \tag{7}$$

where $\dot{Q}$ is the heat transfer rate, ε is the emissivity, σ is the Stefan-Boltzmann constant that takes the value of 5.67 x 10^{-8} W/m^{2}K^4, and T is the absolute surface temperature. However, all objects are emitting, absorbing, reflecting and transmitting radiation simultaneously. The rate of heat transfer to a surface depends on the above factors in addition to orientation and surface characteristics of the objects. This complex interplay can be modeled with photon transport. A classic example of modeling radiation heat transfer with photon transport between two surfaces through an intervening media is schematically illustrated with Fig. 8.

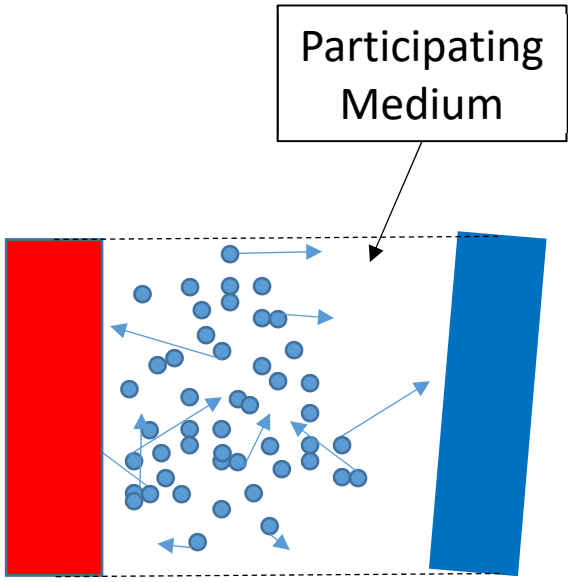

Fig. 8. Radiative photon transport between two surfaces through a participating medium where the red surface would be relatively hot and the blue surface is relatively cold. The blue circles are representing photons.

The photons are represented as blue circles being transported from the two surfaces (red and blue rectangles) through a participating medium. Photons are emitted from surfaces over a range of wavelengths. They move uninterrupted through the medium (drift) until interaction with the atoms of the medium. This interaction can involve absorption of a photon, emission of a photon, or scattering of the photon[22]. To accurately evaluate surface heat fluxes due to radiation, all of the above mechanisms must be represented. This type of approach of modeling the particle (quantum) nature of the wave propagation is similar to quasi-particle based approaches for phonon transport (nanoscale conduction) modeling and concepts such as drift and scattering require accurate prediction.

1.3 Macroscale Conduction Shortcomings

Fourier's Law of Heat Conduction is unreliable at the nanometer length scales and picosecond time scales associated with transistor geometries [23-25]. An experimental illustration of this, for carbon nanotubes, can be found in Fig. 9. With Fig. 9, Chang et al. [23] showed that the effective thermal resistance of the nanotube does not agree with theoretical results from Fourier's law.

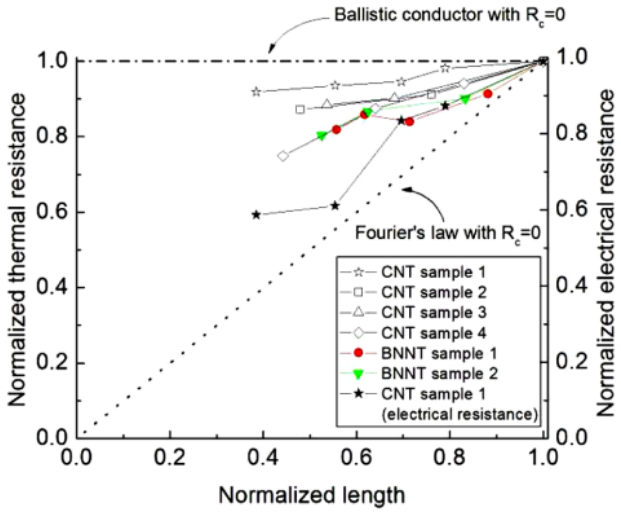

Fig. 9. Illustration of the unreliable results from Fourier's Law at nanoscale geometries. Reproduced from [23].

Yang et al. [24] and Hsiao et al. [25] showed similar results for nanowires. The inability of Fourier's Law to predict heat conduction at nanometer length scales occurs because of the breakdown of the assumption of local thermodynamic equilibrium. This assumption implies that the local temperature is an accurate representation of the distribution of phonons. The assumption becomes invalid as the transistor length and time scales approach the mean free path and scattering time of the dominant energy carriers [15, 26]. For silicon (depending on the temperature), representative values of the phonon mean free path and scattering time range from approximately 100 nm – 1 μm and 10 ps – 10,000 ps respectively [27]. According to Fig. 1, transistor feature sizes were below this range as of about 1990. This is illustrated with an annotated version of Fig. 1 in Fig. 10.

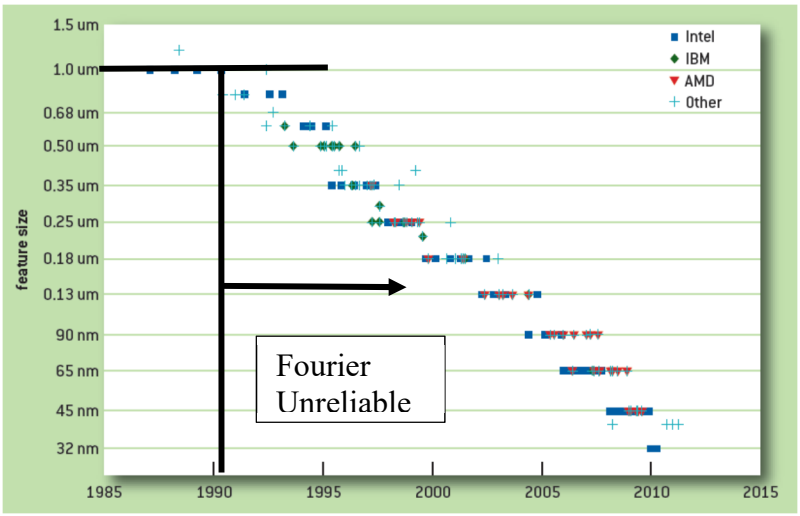

Fig. 10. Minimum transistor feature size from 1990 – 2010. Annotated to show point in time at which Fourier's Law became unreliable. Adapted from [3].

In addition to the effect of small length scales, transistor switching frequencies approached the characteristic scattering times of phonons in a similar timeframe seen above. The Intel486™ processor introduced in 1989 reports the minimum high and low time for 33 MHz operation on the order of 5 ns [28]. This is well within the range of characteristic phonon scattering times. As of 2017, according to the IRDS, transistor length scales (as indicated by the gate length) are approximately 20 nm and intrinsic delay times are 3.49 ps. By 2033, the IRDS predicts these length scales will reduce to 12 nm and intrinsic delay times will reduce to 1.57 ps. Both of these factors indicate that the length and time scales of transistors are outside the domain of Fourier's law. Thus, there is a growing urgent need for direct modeling of the transport of these energy carriers for accurate prediction of the distribution of thermal energy. In the semiconducting materials used in microelectronics, the dominant thermal energy carrier is the phonon.

1.4 Nanoscale Thermal Simulations

Simulation of phonon transport with any computational model will involve a tradeoff between accuracy, efficiency, and flexibility. It is the premise of this dissertation that the SPTM can be a flexible, efficient, and accurate tool for device level phonon transport modeling. To provide context of the proposed work in the area of phonon transport modeling, a brief review of the previously reported simulation techniques is presented.

1.5 Direct Atomic Simulation (DAS)

Direct atomic simulation involves modeling of the state of the atoms that make up the material. Typically, this is broken into simulating the state of motion of the nuclei (and core electrons) separate from the ground state valance electronic configuration. This is realistic as the much lighter electrons respond more quickly to changes in surrounding forces that the relatively heavy nuclei. This is known as the Born-Oppenheimer assumption [29]. This amounts to predicting the motion (vibrational state) of the nuclei (typically treated classically) moving in an interatomic potential created by the ground state electron configurations. The interatomic potential has been represented using phenomenological means previously. These include the Stilinger-Weber [30], Tersoff [31], Tewary [32], and the Environment Dependent Interatomic potentials [33]. More recently, interatomic potentials have been obtained from a first principles

based electronic configuration tool known as Density Functional Theory (DFT) [29, 34]. Molecular dynamics simulations utilizing DFT are referred to by many names but are typically called quantum molecular dynamics (QMD) [35]. Direct atomic simulation has been implemented to study different scenarios involving thermal transport. For example, Proshchenko et al. [36] studied the effects of random interstitial defects on phonon transport in bulk silicon using molecular dynamics. Meem et al. [37]studied the effects of vacancy defects on thermal conductivity of silicon nanowires. Sun and Murthy [38] investigated thermal transport at silicon/germanium interfaces. Fan et al. [39] looked at thermal conductivity of bulk silicon, graphene, and carbon nanotubes. Suzuki et al. [40] modeled charge and thermal transport in a silicon nanowire transistor using a coupling of molecular dynamics and Monte Carlo methods. Also, Rhyner et al [41-43] have modeled heat and charge transport in silicon nanowire transistors using a Non-Equilibrium Greens Function (NEGF) method. Direct atomic simulations have the advantage that the only input required is the interatomic potential. No knowledge of phonon interactions is required in advance. With an accurate interatomic potential, accurate results can be obtained. For example, Proshchenko et al. [36] were able to obtain results for the thermal conductivity of silicon of 122.22 +- 13.81 W/mK. This is within reasonable agreement to experimental results of 130 – 150 W/mK at 300 K. Fan et al. [39] were able to obtain results for bulk silicon of about 147 +- 2 W/mK. However, these simulations can have several disadvantages. They generally suffer from relatively high computational cost [36]. In modeling the silicon nanowire transistor with a diameter of 10 nm and length of 20 nm Suzuki et al. [40] reported that 1 ns of simulation time with their coupled electron Monte Carlo/molecular dynamics calculation took 4 days on an Intel core i7 3930k CPU. They were able to achieve a significant speed up (to about 18 hours) by utilizing an NVIDIA GeForce GTX690 GPU.

1.6 Monte Carlo (MC)

More flexible approaches that generally allow simulation of more complex geometries with larger domain sizes and longer simulations times rely on treating phonons as quasi-particles. Traditionally these are called Monte Carlo (MC) simulations. Within these simulations, phonon trajectories are tracked as they undergo various interactions [44]. Accurate representation of dispersion relations and scattering interactions are important to produce effective simulations. Dispersion curves show the available energy levels for phonons and the relationship between momentum and energy. Scattering is the process by which phonons interact to change their state. Past MC simulations have treated these two areas with varying levels of detail. In regards to dispersion, initial works gave all phonons the same group velocity and did not consider different polarizations [45]. Improvements were made to account for non-linear dispersion of just certain kinds of phonons (acoustic phonons) in an isotropic manner [46]. Curve fits to experimental dispersion data were implemented in an isotropic manner [47]. More recent work has used realistic dispersion relations calculated from the adiabatic bond charge model [48] or interatomic force constants from density functional theory [49].

Three phonon scattering is the primary process by which phonon transport is impeded in insulating or semiconducting materials. The representation of three phonon scattering in MC simulations been implemented in a variety of ways. Initial works used a constant lifetime [44] or lifetimes in the form of simple phenomenological formulas like those of Klemens [50]. Some only consider the available partners considering conservation of energy and momentum without consideration of a scattering strength parameter [46]. Later enhancements include the use of relaxation times computed from equations proposed by Holland [51]. Relaxation times based on

the use of Fermi's Golden Rule (this will be discussed further in Section 4.3) have been presented in many works like those of Ziman [52], Reissland [53], Srivastava [54], Hans and Klemens [55], Wang and Murthy [56], Esfarjani et al [57], Narumanchi et al [58], Ward and Broido [59], Gutierrez et al [60], Sabatti et al [61], Li et al [62], and others.

Despite the range of models associated with the MC approach, they typically lack in several areas. First, the dispersion relations are often isotropic [46] or rely on interatomic force constants that lack accuracy. Second, the scattering algorithms all rely on random number generation and do not typically directly result in conservation of energy and momentum. For example, Wu et al [49] implements a technique that is common in the MC simulation where scattered phonons are deleted from the simulation domain and new ones are introduced randomly from the equilibrium distribution. The actual number of phonons involved in scattering are not physically distributed among the partner states. This does not result in conservation of momentum or energy in an individual scattering event. Lastly, all use scaling factors to represent the actual number of phonons in a given volume and in scattering events. For example, Sabatti et al. [61] simulated phonon transport in a 2 μm silicon thermal resistor at 300 K using 130, 000 particles where each nanosecond of simulation required 1h and 30 minutes of wall clock time on 50 core processors (the type was not specified). With a cross section of 50 nm, there are on the order of 10^8 phonons in this domain. Thus, only representing a little over 0.1 % of the phonons in the domain. Kukita et al. [48, 63, 64] simulated phonon transport in FinFETs with a gate length of 22 nm and Fin thickness of 8 nm utilizing about 10, 000 particles. Table 1 shows that the actual number of phonons in the domain of similar size FinFETs are on the order of 10^6.

1.7 Statistical Phonon Transport Model

The Statistical Phonon Transport Model (SPTM) [9-11] was introduced to overcome some of the deficiencies of the physical models and algorithms of traditional MC codes. It is based on algorithms that allow for representation of all of the phonons in a given geometric domain. This eliminates the need for scaling factors. Full anisotropic dispersion is implemented. Within three phonon scattering, energy and momentum conservation is strictly enforced. The need for random number generation is eliminated because all of the phonons of a given type are distributed according to the probability of a given interaction, computed from basic physical principles, among all partner states. Thus, the SPTM allows for increased physicality and higher fidelity phonon transport modeling compared to MC. In addition, it is well suited for increased computational efficiency as individual phonon trajectories are not tracked and the code was developed to be implemented in a parallel nature. For example, some of the three phonon scattering results documented in this dissertation for an isothermal 100 nm cube of silicon at 500 K takes approximately 8.72 minutes for 1 ns (1 ps time step – 1000 time steps) of simulation time using a laptop with the Intel®Core™i7-6820HQ CPU operating at 2.7 GHz. In comparison to the DAS work of Fan el al. [39] (using the LAMMPS [65] software), the computational time was reported to be 6.0 x 10^5 atom-step/second computed on an Intel®Xenon™CPU E3-1230 V2 at 3.3 GHz. At the simulation specifications noted above (100 nm cube silicon domain, 50E6 atoms and 1000 time steps), DAS would take approximately 1387 minutes. As transistor feature sizes become smaller toward the horizontal and vertical nanowire dimensions noted in Table 1, it will be feasible to simulate thermal transport in silicon nanowire transistors using DAS in much shorter time frames, however, the SPTM will still be preferred to DAS due to several other disadvantages. The output of DAS calculations involve classical representations (not quantum)

of atomic positions as a function of time in real space. Extracting phonon specific properties may be difficult or require significant post processing [66]. Modeling mode specific interactions between phonons and other particles (like conduction electrons or photons) may also pose difficulties. Generating quick turnaround design changes or extending geometric domains to include multiple adjacent transistors would still be limited by computational effort. Thus, in comparison to MC and DAS of phonon transport the SPTM offers a high combination of fidelity, flexibility, and computation efficiency that will meet the needs of engineers.

2 Objectives

It is the premise of this dissertation that the SPTM can provide a high combination of flexibility, efficiency, and accuracy for device level phonon transport modeling. The SPTM will fill the gap between the lower fidelity MC models and high fidelity, inflexible direct quantum simulations. An extended SPTM will provide device designers with insight into non-equilibrium phonon conditions. Precise details of the phonon distribution are required for accurate predictions of thermal effects on charge transport with different design conditions including dopant concentrations, voltage biases, channel length, and gate geometry. Currently, reliability metrics are primarily influenced by temperatures but, non-equilibrium behavior could lead to different interpretations or prediction of these factors. In addition, the impact of mitigation strategies like enhanced heat transfer can only be effectively judged if accurate phonon conditions are modeled. Thus, this dissertation focuses on enhancing the physical models and algorithms of the SPTM compared to the Brown III version of the SPTM [9-11]. Subsequently, the enhanced SPTM will demonstrate its' ability to simulate non-equilibrium phonon transport in one-, two-, and three-dimensional transistor-like devices with realistic boundary conditions. The enhancements entail four major attributes which are detailed in Table 2 and described in the paragraphs to follow.

Table 2. Summary of Enhanced SPTM Model Improvements Compared to Brown III [9-11]

Attribute	SPTM Brown III	SPTM Medlar
Phonon Dispersion	Lattice dynamics with first nearest neighbor interactions	Lattice dynamics with first and second nearest neighbor interactions calculated from density functional theory
Three Phonon Scattering	Phenomenological model based on phonon populations	Quantum mechanics based model using Fermi's Golden Rule
Phonon Drift	1-d with limited boundary conditions	1-d, 2-d, and 3-d with enhanced boundary conditions
Joule Heating from Electron Phonon Scattering	None	Simplistic phonon source distribution accounting for strength of interaction and selection rules

First, the lattice dynamics model for the calculation of dispersion relationships will be enhanced to include second nearest neighbor interactions and interatomic force constants calculated from first principles. This will allow improvements to the SPTM to accurately reproduce

experimental observations of phonon dispersion curves in high symmetry directions for pure silicon. In addition, it will allow for accurate representation of phonon dispersion curves in all directions and polarizations for pure silicon.

Second, the three phonon scattering representation will be enhanced to include physics-based models (time dependent perturbation theory – Fermi's Golden Rule) for the computation of the scattering rate. It will be demonstrated that the revised SPTM inherently conserves energy and momentum across all applicable length and time scales. In addition, the SPTM will be shown to transiently return to thermodynamic equilibrium (if deviated) across applicable length, time, and temperature scales.

Third, the drift algorithms will be extended to include the capability to model phonon transport in one, two, and three dimensions. These enhancements along with changes to the boundary conditions of the SPTM will allow for flexible device modeling.

Fourth, the SPTM will be enhanced to model spatial and time dependent heat generation to represent Joule heating as a result of electron phonon interactions. This allows modeling of the thermal effects of the steady state operation and transient switching dynamics of semiconductor transistors. Design level thermal information on prototypic nanowire transistors will be presented and comparisons to other state of the art thermal simulations will be shown.

These four objectives may be embodied in this over-arching research question:

Is it possible to conduct high-fidelity, three-dimensional, phonon transport simulations of nanoscale electronic devices operating under transient switching conditions which reflect the non-equilibrium thermal phenomena associated with electron-phonon scattering induced heat generation?

3 Background and Theoretical Foundation for the SPTM

3.1 Nanoscale Heat Conduction

On the atomic level, conduction can be thought of as the result of two mechanisms. These consist of the movement of free electrons and the transport of energy associated with lattice vibrational waves. Within electrically conductive materials (mostly metals) both of these mechanisms exist. Within electrically insulating or semi-conducting materials, lattice vibrational waves are the predominant mechanism and thus are the subject of this work.

3.1.1 The Phonon

The atoms that comprise the lattice of a given material are in constant vibrational motion at any temperature above absolute zero. Atoms do not move in isolation as their movement directly affects neighboring atoms through displacement-dependent interatomic forces. Thus, the vibration of one atom can affect the movement of its neighbors in the form of a lattice vibrational wave. To illustrate this concept, consider a 1-d atomic lattice shown in Fig. 11,

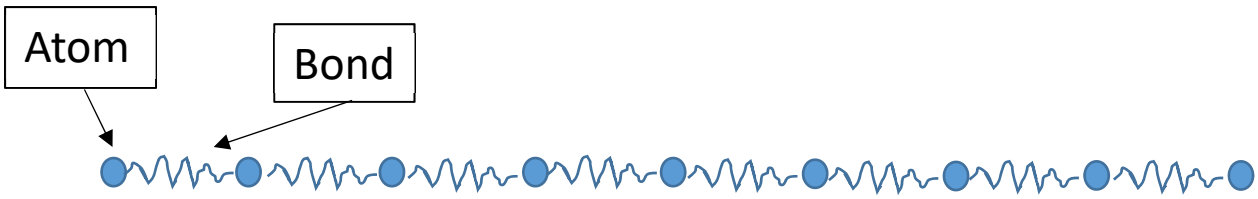

Fig. 11. Representation of a linear atomic lattice where the blue circles are atoms with core electrons and the "springs" show the effect of interatomic forces (aka bonds).

where the circles represent atoms and the zig-zag lines represent interatomic bonds. If the left most atom is displaced from its equilibrium position to the right, this would exert a force on its immediate neighbor that would have a tendency to force it to the right and this would continue down the line of atoms. Thus, a lattice vibrational wave is transmitted through the line of atoms. The quantum nature of the atoms dictate that when they are confined to exist in a certain region in space (bound state) they can only be found in discrete energy levels [67]. This implies that only a discrete amount of energy (and momentum) is transmitted with the lattice vibrational wave. This discrete amount of energy is referred to as a phonon [68, 69] and is analogous to the discrete amount of energy transmitted with the electromagnetic wave called the photon. The amount of energy associated with the elementary excitations is proportional to the frequency of the phonon and is equal to $\hbar\omega$, where $\hbar$ is modified Planks constant with a value of 1.0545718E-34 J-s.

As all objects have a wave/particle duality, phonons can be thought of as pseudo particles. This is an adequate description as long as the length scales under consideration are larger than the characteristic wavelength of the phonon (sometimes called the coherence length) [15]. As elementary excitations of the lattice, multiple phonons can exist with the same quantum conditions. This implies that they follow Bose Einstein statistics and the excitation number (related to the number of phonons with given characteristics) are given by the following [69].

$$n = \frac{1}{e^{\hbar\omega/k_B T} - 1}\ , \tag{8}$$

where n is the phonon occupation number (units of number per unit volume in physical space per unit volume in wavevector space) , k_B is the Boltzmann constant given as 1.38064852E-23 J/K, and T is the absolute temperature. The phonon occupation number is directly related to the number of phonons in a given volume of real space.

3.1.2 Phonon Dispersion and Relation to Crystal Structure

Determination of the energy levels (or normal modes) available to phonons amounts to the determination of the dispersion relationship. The dispersion relationship describes the relationship between energy and momentum for phonons. Dispersion relations are directly affected by the geometry of the atomic lattice for a given material as well as the interatomic force relationships. The materials under consideration (silicon and germanium) have the diamond centered crystal structure. This structure is illustrated in Fig. 12.

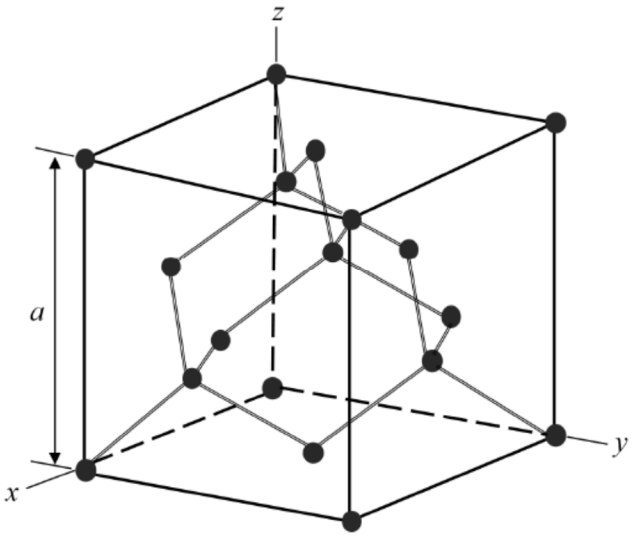

Fig. 12. Diamond centered crystal structure. Reproduced from [9].

It is instructive to look at the lattice in wavevector space (k-space) or reciprocal space. Reciprocal space is formed by taking the 3D spatial Fourier transform of the real space lattice. A special portion of k-space is referred to as the First Brillouin Zone (FBZ). The FBZ represents the basic unit cell in wavevector space and the physically meaningful values of the wavevector for phonons. Wavevectors beyond this space can always be related back to the FBZ due to the concept of aliasing [69]. That is, there is no physically identifiable difference between a wavevector inside the FBZ and one with the addition of a reciprocal lattice vector if atomic displacements are sampled on the lattice points. The edge of the FBZ (zone boundary) represents phonons with the minimum meaningful wavelength relative to the lattice. A schematic of the FBZ for silicon is shown in Fig. 13.

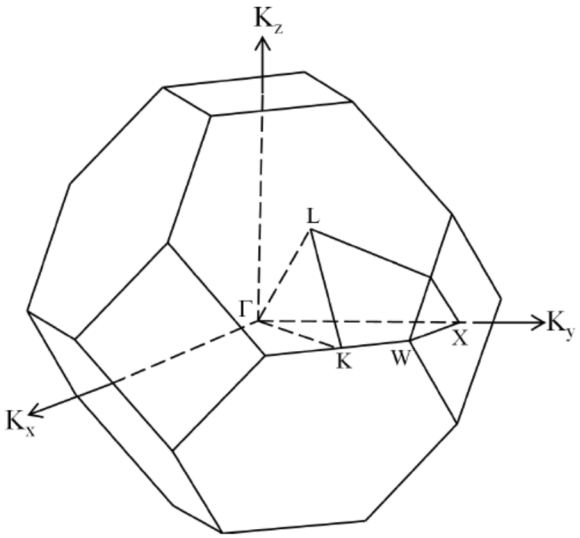

Fig. 13. FBZ for silicon. Reproduced from [9].

Each axis labels the different components of the allowable wavevectors. Traditionally, certain locations in the wavevector space are labeled with the letters Γ, L, X, K, and W shown in Fig. 13. The labels are used to denote directions of high symmetry of the crystal lattice. For example, the direction Γ-L is referred to as the (100) direction and denotes propagation of phonons in a direction parallel to one edge of the cubic unit cell shown in Fig. 12. The direction Γ-L would be denoted as the (111) direction and represents phonon propagation along the body diagonal of the cubic unit cell. The direction G-K is denoted as the (110) direction and represents phonon propagation along the face diagonal.

Six energy levels are available at any wavevector in the FBZ [68]. The energy levels are labeled with different frequencies and are referred to as modes or polarizations. The different modes are physically related to the different manners in which the adjacent atoms in the lattice can move relative to one another. The acoustic modes involve adjacent atoms moving in the same direction while optical modes are moving opposite to one another. Within acoustic and optical, transverse and longitudinal motions can be identified. Transverse indicates that atomic motions are perpendicular to the direction of motion of the wave whereas longitudinal indicates atomic motions are parallel to the direction of the wave (compression wave). Two transverse directions exist for any given longitudinal direction and they are orthogonal to the longitudinal direction. An example of experimentally determined dispersion relationships for silicon is illustrated with Fig. 14.

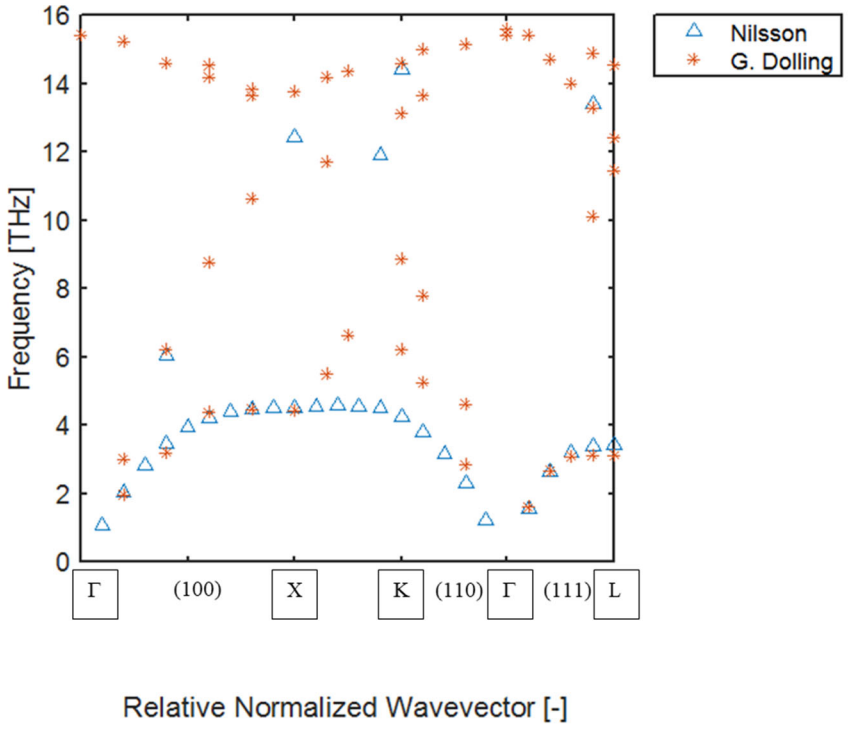

Fig. 14. Experimental values for silicon dispersion in the (100) direction at 300 K. Triangles are experimental data from Nilsson and Nelin [70], Open circles are from Dolling [71].

Results are shown for frequency vs. wavevector in different directions in the FBZ. The labeling of the graph corresponds to the different wavevector points identified in the FBZ labeled in Fig.

13. Phonons traversing in different directions through the lattice can have different frequencies. This is a result of the different interatomic forces that result from different trajectories. As a result, they will exhibit different group velocities as they traverse through the material lattice. The group velocity is defined in equation 9.

$$v_g = \frac{d\omega}{dk} \tag{9}$$

Graphically, this is interpreted as the slope at any point on the dispersion curves.

3.1.3 Three Phonon Scattering

Scattering interactions affect phonon transport just as photon interactions with intervening media affect radiative transport. Phonons can interact with boundaries, interfaces, impurities, transport electrons, photons, and other phonons. In a pure insulating bulk material the primary interaction that affects phonon transport is three phonon scattering. As the name suggests, this involves the interaction of three phonons, which can take two forms. A Type I interaction is one in which two phonons combine to create a third, or the reverse process called a Type II interaction in which a single phonon decomposes into two others. If phonons can be considered as wave packets, this process is graphically illustrated in Fig. 15,

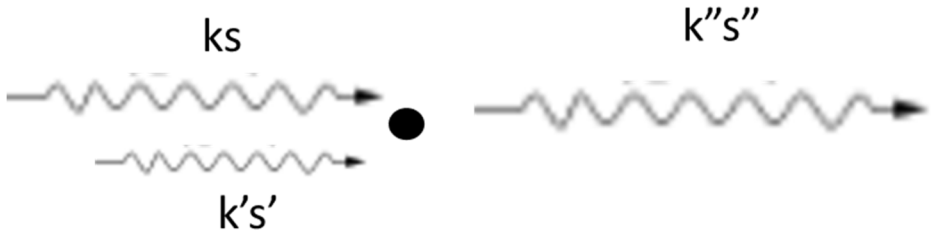

Fig. 15. Illustration of 1-d three phonon scattering where phonons ks and k's' produce k"s" in the Type I event or the reverse occurs in the Type II event.

where k, k' and k" indicate the wavevectors of the three phonons and s, s' and s" are the polarizations or modes. In both types of interactions, energy and momentum (up to the subtraction of a reciprocal lattice vector) is conserved. This implies the following regarding wavevectors and frequencies.

$$ks + k's' = k''s'' + G \tag{10}$$

$$\omega(k) + \omega'(k') = \omega''(k'') \tag{11}$$

The only meaningful wavevectors are those in the FBZ. If an interaction involves the addition of wavevectors that lead to a result inside the FBZ it is referred to as a normal scattering event. If an interaction involves the addition of wavevectors that results in one outside the FBZ it is aliased back to the FBZ. This type of backscattering interaction is called an Umklapp process. Both types of interactions are schematically shown with Fig. 16 [69].

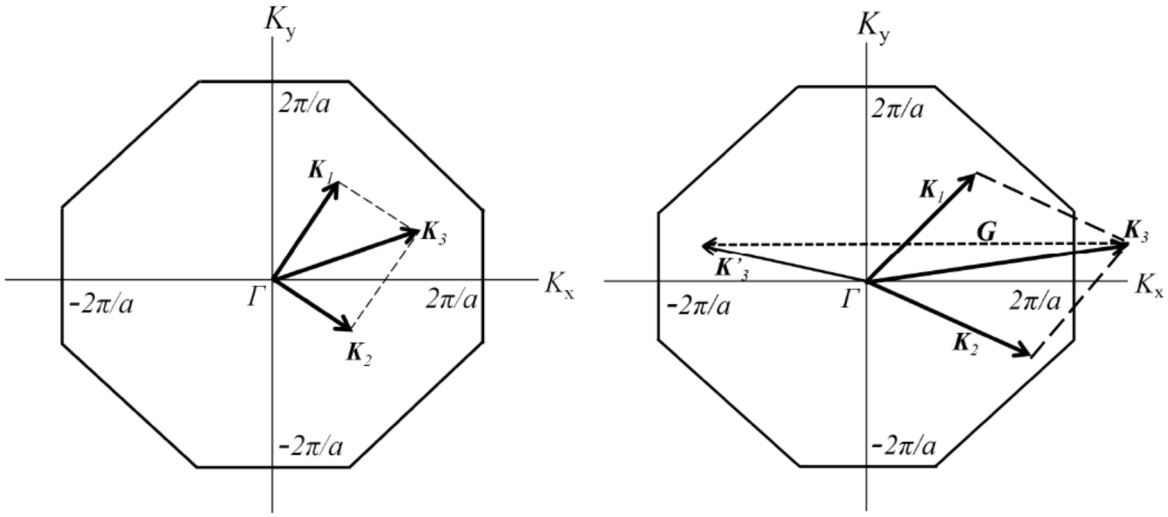

Fig. 16. Normal vs. Umklapp three phonon scattering in a 2-d representation of the wavevector space. Phonons K_1 and K_2 interact to result in K_3 in the normal process on the left. Phonons K_1 and K_2 interact to result in K_3 that is reflected back into the FBZ with the reciprocal lattice vector G in the Umklapp process on the right. Reproduced from [9].

Three phonon scattering is the result of a physical feature of the interatomic potential referred to as the anharmonic interatomic potential. This implies that the variation in interatomic potential energy as a function of interatomic distance is not symmetric. As an example, consider the illustration of a two atom interatomic potential for an H_2 molecule compared to a harmonic (symmetric) potential shown in Fig. 17 [72].

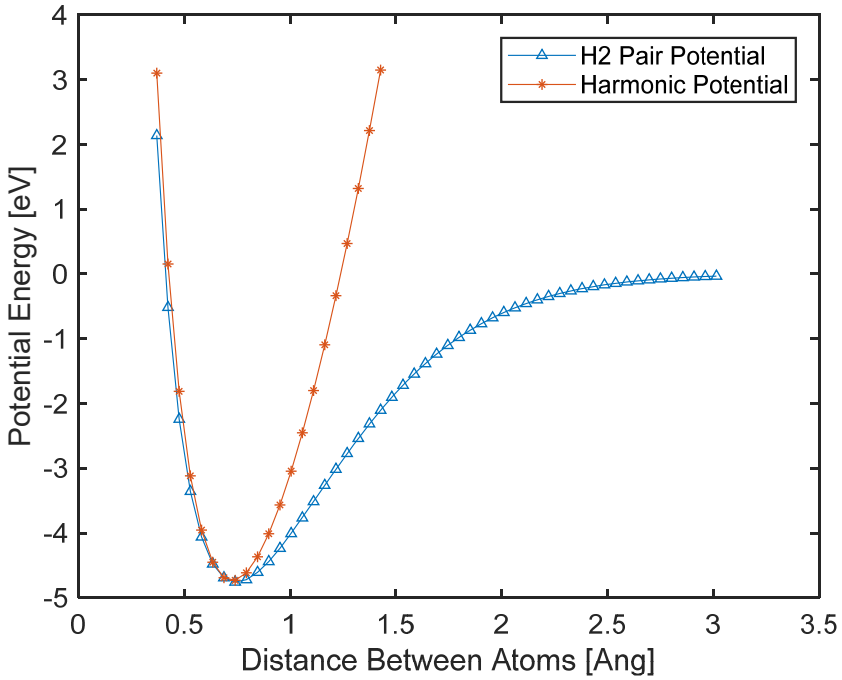

Fig. 17. Anharmonic interatomic potential illustration. Variation in electrical potential energy as a function of interatomic spacing for a diatomic molecule of hydrogen and a harmonic approximation. Adapted from [72].

The asymmetric nature of the interatomic potential energy curve for the H_2 pair potential implies that the interatomic forces (the negative of the slope at any location on the chart and a result of changing electron configurations) are different depending on the relative locations of the atoms. If the interatomic forces were modeled as springs, this would imply non-constant spring constants for expansion or compression. These are referred to as interatomic force constants and it is the change in the interatomic force constant as atoms are displaced from equilibrium that leads to three phonon scattering. The presence of one phonon results in an atomic displacement pattern that changes the effective force constant experienced by another phonon and results in the probability of a scattering event [68].

3.1.4 Other Scattering Mechanisms

Phonons can interact with boundaries, interfaces, impurities (such as dopants), transport electrons, photons, and other phonons. Within transistors, thermal energy generation is a result of electron-phonon interactions [73]. The origins of this interaction on the atomic level can be considered a result of two sources.

The first source of the electron-phonon interaction is called the deformation potential interaction. It is a result of phonons deforming the atomic electron cloud because of the displacement of atoms from equilibrium. This deformed potential influences the movement of conduction electrons and can cause transitions in state of the electrons and phonons [52]. This is visualized with Fig. 18.

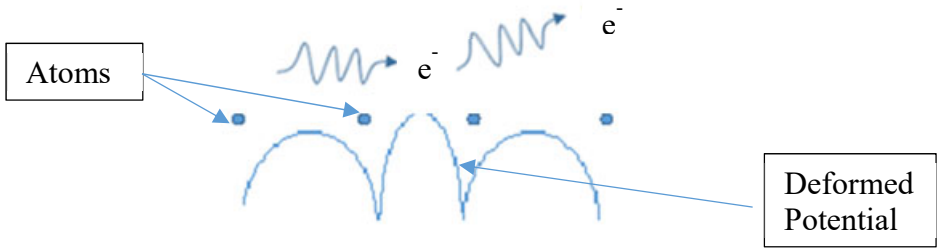

Fig. 18. Example of the interaction of an electron with a deformed linear chain of atoms. Atoms are represented with blue circles, the deformed electric potential is represented as the blue lines, and the electrons are shown with wavepackets and e^-. Adapted from [52].

The blue circles are the atoms (nuclei and core electrons), the blue lines represent the interatomic potentials, and the wave packets labeled with e^- represent conduction electrons. The two atoms in the center are moved closer to one another by the presence of a phonon and this results in a change in the interatomic potential illustrated with the blue curves. This change causes scattering of the electron wave packet from its initial trajectory. Mathematically, this is treated in a manner similar to three phonon scattering and will be discussed in more detail in section 4.5. This interaction is present in both polar crystals (such as silicon) and non-polar crystals.

The second type of electron-phonon interaction mechanism is called the Frohlich interaction. It is only present in polar or ionic crystals where unequal sharing of valence electrons between adjacent atoms creates alternating positive and negative charged. When an optical phonon is present, it will cause adjacent ions of opposite charge to oscillate and lead to a long range oscillating electric field that can influence electrons to change state [74]. This interaction is similar in effect to how an electromagnetic wave can induce optical phonons in ionic compounds or polar semiconductors. It is visualized with the Fig. 19.

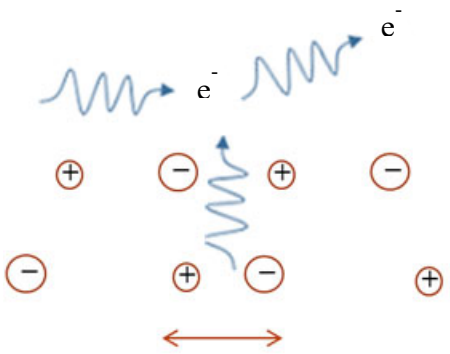

Fig. 19. Oscillating ions in a polar or ionic crystal leading to Frohlich interaction. Ions are labeled with a + or – enclosed in a circle. Electrons are labeled with a wavepacket and an e⁻. Adapted from [74].

The plus and minus circles indicate ions of opposite charge and the wavy line indicates an electromagnetic field leading to scattering of the electron wave packet and thus a change in energy state.

Electron-phonon interactions arise due to the added charge carriers introduced by dopant atoms. Dopant atoms are impurities within the silicon lattice. As such, phonon transport is affected by the presence of these impurities. The dopant atoms differ in mass from the base silicon and create a change in the interatomic force constants in the vicinity of the impurity. This can produce a perturbation that can lead to a change in state [75]. The impurity scattering rates are directly dependent on the square of the frequency of the phonon involved, the number of phonons with that frequency, and the impurity scattering parameter [61]. The impurity scattering parameter is directly dependent on the difference in mass between the dopant atoms and the silicon atoms, the concentration of dopant atoms, as well as the difference in local force (stiffness) constants between the host atoms and the impurity atoms. As the dopant concentration increases, additional effects on dispersion relations will result. Also, as the type of dopant will vary from the source to the drain of a transistor, impurity scattering rates will be a function of location within the transistor and could lead to an interfacial scattering effect as a result of phonon propagation through different doped regions.

Boundary scattering occurs between phonons and actual boundaries or interfaces. Scattering at boundaries or interfaces becomes the dominant mechanisms of impeding thermal transport [76] as dimensions become significantly smaller than the mean free path of the phonons within the lattice. This occurs because the probability of three phonon interaction becomes smaller with the reduced length and time scales. Thus, there is a high probability of the phonons traversing the geometric domain without experiencing a scattering event. This is referred to as a classical size effect and can result in ballistic transport between boundaries. Boundary scattering can be treated as adiabatic (no heat transfer) using varying degrees of specularity from pure specular reflection to a completely diffusive approach [9].

4 Modeling Approach

4.1 Dispersion - Theory

Accurate determination of the dispersion relationships is vital as they affect the interaction among phonon modes that takes place in three phonon scattering as well as the average speed

that phonon wave packets travel through the physical domain. This work makes use of the lattice dynamics technique [77] with the harmonic assumption [53] to calculate dispersion relations. This technique amounts to the application of Newton's 2nd Law to the atomic lattice where interatomic forces are expressed as a function of interatomic force constants and atomic displacements. The difficulty in the use of this method to obtain accurate results lies in the use of accurate interatomic force constants and the inclusion of enough neighboring interactions to reproduce the relevant physics. This model makes use of interatomic force constants calculated from Density Functional Theory (DFT) [34] and includes up to second nearest neighbor interactions.

Development of the model follows closely that of Herman [77]. For illustration, the relative arrangement of the first and second nearest neighbor atoms of silicon are shown below. The two atoms that make up the basis of silicon are illustrated within the boxed region. If these atoms are applied to the Face-Centered-Cubic (FCC) lattice, then the diamond lattice (Fig. 12) is created.

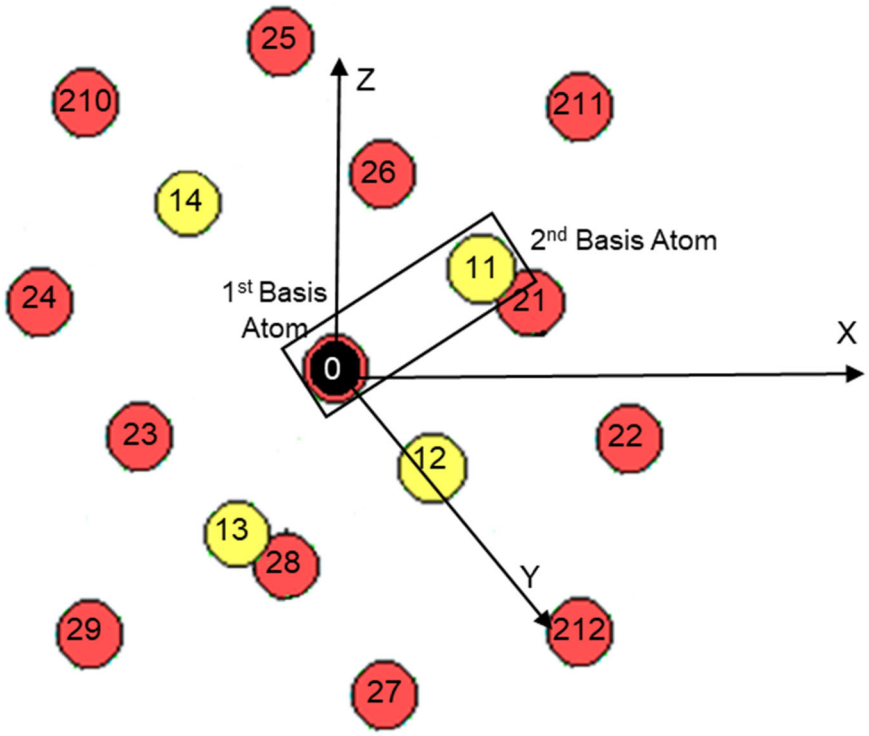

Fig. 20. Illustration of the atoms associated with the silicon lattice in 3-d. The four first nearest neighbor atoms are shown in yellow and labeled 11 - 14. The twelve second nearest neighbors are illustrated in red and labeled 21 – 212. Adapted from [78].

The atoms in Fig. 20 are labeled with the following scheme. The central atom is black and labeled as 0, the four nearest neighbor atoms are yellow and labeled 11-14, and the twelve second nearest neighbor atoms are red and labeled as 21 – 212. The derivation begins with application of Newton's 2nd Law to the central atom in each coordinate direction as follows:

$$\Sigma F_x = ma_x \tag{12}$$

$$\Sigma F_y = ma_y \tag{13}$$

$$\Sigma F_z = ma_z \tag{14}$$

An expanded version of the forces acting in the x-direction on atom 0 is shown in equation 14.

$$\begin{aligned}\sum F_x(0) = F_x(00x) + F_x(00y) + F_x(00z) + F_x(011x) + F_x(012x) + F_x(013x) + \\ F_x(014x) + F_x(011y) - F_x(012y) + F_x(013y) - F_x(014y) + F_x(011z) - F_x(012z) + \\ F_x(013z) - F_x(014z) + F_x(021x) + F_x(022x) + F_x(023x) + F_x(024x) + F_x(025x) + \\ F_x(026x) + F_x(027x) + F_x(028x) + F_x(029x) + F_x(0210x) + F_x(0211x) + \\ F_x(0212x) + F_x(021y) + F_x(022y) + F_x(023y) + F_x(024y) + F_x(025y) + \\ F_x(026y) + F_x(027y) + F_x(028y) + F_x(029y) + F_x(0210y) + F_x(0211y) + \\ F_x(0212y) + F_x(021z) + F_x(022z) + F_x(023z) + F_x(024z) + F_x(025z) + F_x(026z) + \\ F_x(027z) + F_x(028z) + F_x(029z) + F_x(0210z) + F_x(0211z) + F_x(0212z)\end{aligned} \tag{15}$$

Each term represents the force resulting on atom 0 in the x direction when the given atom is displaced in a certain direction. For example, $F_x(011x)$ indicates the force in the x-direction on atom 0 when the atom labeled 11 is displaced in the x-direction. $F_x(027z)$ Indicates the force in the x-direction on atom 0 when atom 27 is displaced in the z-direction. Next, the forces acting on the atoms are expressed in terms of interatomic force constants multiplied by atomic displacements. This amounts to the harmonic assumption and is expressed with equation 16,

$$F_x(011x) = \frac{\partial^2 V}{\partial x^2} u_{11x} \ , \tag{16}$$

where $\frac{\partial^2 V}{\partial x^2}$ is the second derivative of the interatomic potential between atom 0 and atom 11 and $u_{11x}$is the displacement of atom 11 in the x-direction. The second derivatives are the interatomic force constants and are traditionally expressed using the notion shown in Table 3.

Table 3. Interatomic force constants [34]

α_0	On-site interaction
α_1	First nearest neighbors
β_1	
μ_2	Second nearest neighbors
ν_2	
δ_2	
λ_2	

Where a subscript of 0 indicates the original atom, a subscript of 1 indicates first nearest neighbors, and a subscript of 2 is for second nearest neighbors. The different force constants represent different interactions between the atoms involved. For example, α_1 represents the interaction between atom 0 in a given coordinate direction when the first nearest neighbors are displaced in the same directions. Thus, in equation 15, $\frac{\partial^2 V}{\partial x^2}$ is equal to α_1. Similarly, β_1 represents the interaction between atoms 0 in a given direction when the first nearest neighbors are displaced in orthogonal directions from atom 0. So, β_1 would appear in the equation for $F_x(011y)$ representing the second derivative term. Likewise, the second nearest neighbor force constants are used in a similar manner for the forces between atom 0 and the second nearest neighbor atoms labeled 21-212. However, the second nearest neighbor atoms form a different geometric configuration around atom 0 than compared to the first nearest

neighbor atoms. Atoms 21 – 24 all lie in the x-y plane, atoms 25 – 28 lie in the y-z plane, and atoms 29 – 212 lie in the x-z plane. Because of this planar nature, four force constants are required to describe the interactions depending on whether the atoms are moved within the plane of the second nearest neighbors or out of the plane. μ_2 represents the force constant between atom 0 and atoms in the x-y and x-z planes when the atoms are displaced in the same in-plane coordinate direction. ν_2 represents the force constant between atom 0 and atoms in x-y and x-z planes when the atoms are moved in the orthogonal in-plane direction. δ_2 represents the force constant between atom 0 and the atoms in the x-y and y-z planes when they are moved in the orthogonal out-of-plane direction. And, λ_2 represents the force constant between atom 0 and the atoms in the y-z plane when they are moved in the same coordinate, out-of-plane, direction. The force constants above are obtained from the use of a first principles quantum electronic configuration calculation called DFT. The details of the DFT calculation are not discussed here. An introduction to DFT is discussed in Sholl [29] and the method specific to the interatomic force constants is detailed in Aouissi et al [79].

After insertion of the force constant notation, the sum of the forces acting in the x-direction on atom 0 is show with equation 17.

$$\begin{aligned}\sum F_x(0) = -\alpha_0 u_x(0) - \alpha_1 u_x(11) - \alpha_1 u_x(12) - \alpha_1 u_x(13) - \alpha_1 u_x(14) - \beta_1 u_y(11) + \\ \beta_1 u_y(12) + \beta_1 u_y(13) - \beta_1 u_y(14) - \beta_1 u_z(11) + \beta_1 u_z(12) - \beta_1 u_z(13) + \beta_1 u_z(14) - \\ \mu_2 u_x(21) - \mu_2 u_x(22) - \mu_2 u_x(23) - \mu_2 u_x(24) - \lambda_2 u_x(25) - \lambda_2 u_x(26) - \lambda_2 u_x(27) - \\ \lambda_2 u_x(28) - \mu_2 u_x(29) - \mu_2 u_x(210) - \mu_2 u_x(211) - \mu_2 u_x(212) + \nu_2 u_y(21) - \\ \nu_2 u_y(22) + \nu_2 u_y(23) - \nu_2 u_y(24) + \nu_2 u_y(29) - \nu_2 u_y(210) + \nu_2 u_y(211) - \\ \nu_2 u_y(212) - \delta_2 u_z(21) - \delta_2 u_z(22) + \delta_2 u_z(23) + \delta_2 u_z(24) - \delta_2 u_z(29) + \\ \delta_2 u_z(210) - \delta_2 u_z(211) + \delta_2 u_z(212) = M_0 \ddot{u_x}(0)\end{aligned} \tag{17}$$

The atomic displacements are assumed to take the form of a wave solution. This can be thought of as a travelling wave moving through the lattice. An example of the displacement of atom 0 in the x-direction is shown with equation 18,

$$u_x(0) = A_x(0) e^{i\left(\omega t - \vec{k}\cdot\vec{r}(0)\right)} \quad , \tag{18}$$

where $A_x(0)$ is the amplitude of the displacement of atom 0 in the x-direction, ω is the angular frequency of the wave, $\vec{k}$ is the wavevector and $\vec{r}(0)$ is the postion vector to atom 0. Upon insertion into the equations of motion, the following characteristic equation emerges.

$$\begin{aligned}\sum F_x(0) = \alpha_0 A_x(0) + \alpha_1 A_x(1)\left[e^{-iK\cdot r(11)} + e^{-iK\cdot r(12)} + e^{-iK\cdot r(13)} + e^{-iK\cdot r(14)}\right] + \\ \beta_1 A_y(1)\left[e^{-iK\cdot r(11)} - e^{-iK\cdot r(12)} - e^{-iK\cdot r(13)} + e^{-iK\cdot r(14)}\right] + \beta_1 A_z(1)\left[e^{-iK\cdot r(11)} - \right. \\ \left. e^{-iK\cdot r(12)} + e^{-iK\cdot r(13)} - e^{-iK\cdot r(14)}\right] + \mu_2 A_x(0)\left[e^{-iK\cdot r(21)} + e^{-iK\cdot r(22)} + e^{-iK\cdot r(23)} + \right. \\ \left. e^{-iK\cdot r(24)} + e^{-iK\cdot r(29)} + e^{-iK\cdot r(210)} + e^{-iK\cdot r(211)} + e^{-iK\cdot r(212)}\right] + \lambda_2 A_x(0)\left[e^{-i\left(K\cdot r(25)\right)} + \right. \\ \left. e^{-i\left(K\cdot r(26)\right)} + e^{-i\left(K\cdot r(27)\right)} + e^{-i\left(K\cdot r(28)\right)}\right] + \nu_2 A_y(0)\left[-e^{-iK\cdot r(21)} + e^{-iK\cdot r(22)} - \right. \\ \left. e^{-iK\cdot r(23)} + e^{-iK\cdot r(24)} - e^{-iK\cdot r(29)} - e^{-iK\cdot r(210)} + e^{-iK\cdot r(211)} + e^{-iK\cdot r(212)}\right] + \\ \delta_2 A_z(0)\left[e^{-iK\cdot r(21)} + e^{-iK\cdot r(22)} - e^{-iK\cdot r(23)} - e^{-iK\cdot r(24)} + e^{-iK\cdot r(29)} - e^{-iK\cdot r(210)} + \right. \\ \left. e^{-iK\cdot r(211)} - e^{-iK\cdot r(212)}\right] = M_0 \omega^2 A_x(0)\end{aligned} \tag{19}$$

The terms have been grouped in terms of the amplitude of displacements of atom 0 and atom 1 in the x, y, and z directions. Atom 0 is the first basis atom in the silicon lattice and atom 1 is the second basis atom. Note that the second nearest neighbor atoms will share the same amplitude of displacements as the atom labeled 0 as they are identical by symmetry arguments. If the equations of motion are applied in this manner to the y and z directions to both the first and second basis atoms, six equations will result with six unknown displacement amplitudes. This sets up a system of equations that are shown in matrix form in equation 20,

$$\begin{bmatrix} A & B & C & D & E & F \\ G & H & I & E & D & L \\ M & N & O & F & L & D \\ D^* & E^* & F^* & A & B & C \\ E^* & D^* & L^* & G & H & I \\ F^* & L^* & D^* & M & N & O \end{bmatrix} \begin{bmatrix} A_x(0) \\ A_y(0) \\ A_z(0) \\ A_x(1) \\ A_y(1) \\ A_z(1) \end{bmatrix} = \begin{bmatrix} A_x(0)M\omega^2 \\ A_y(0)M\omega^2 \\ A_z(0)M\omega^2 \\ A_x(1)M\omega^2 \\ A_y(1)M\omega^2 \\ A_z(1)M\omega^2 \end{bmatrix}, \tag{20}$$

where the left hand six by six matrix is known as the dyanmical matrix. Its coefficients contain all of the interatomic force constants above and are also a function of a given wavevector. A star(*) indicates the complex conjugate. The functionality of the elements of the dynamical matrix are shown below with equations 21 - 33.

$$A = \alpha_0 + \mu_2 \left[4cos\left(\frac{a}{2}k_x\right)cos\left(\frac{a}{2}k_y\right) + 4cos\left(\frac{a}{2}k_x\right)cos\left(\frac{a}{2}k_z\right)\right] + \lambda_2 \left[4cos\left(\frac{a}{2}k_y\right)cos\left(\frac{a}{2}k_z\right)\right] \tag{21}$$

$$B = \nu_2 \left[-e^{-i\left(\frac{a}{2}(k_x-k_y)\right)} + e^{-i\left(\frac{a}{2}(k_x+k_y)\right)} - e^{-i\left(\frac{a}{2}(-k_x+k_y)\right)} + e^{-i\left(\frac{a}{2}(-k_x-k_y)\right)}\right] + \delta_2 \left[-e^{-i\left(\frac{a}{2}(-k_y+k_z)\right)} - e^{-i\left(\frac{a}{2}(k_y+k_z)\right)} + e^{-i\left(\frac{a}{2}(k_y-k_z)\right)} + e^{-i\left(\frac{a}{2}(-k_y-k_z)\right)} - e^{-i\left(\frac{a}{2}(-k_x-k_z)\right)} + e^{-i\left(\frac{a}{2}(-k_x+k_z)\right)} + e^{-i\left(\frac{a}{2}(k_x+k_z)\right)} - e^{-i\left(\frac{a}{2}(k_x-k_z)\right)}\right] \tag{22}$$

$$C = \nu_2 \left[e^{-i\left(\frac{a}{2}(-k_x-k_z)\right)} - e^{-i\left(\frac{a}{2}(-k_x+k_z)\right)} + e^{-i\left(\frac{a}{2}(k_x+k_z)\right)} - e^{-i\left(\frac{a}{2}(k_x-k_z)\right)}\right] + \delta_2 \left[e^{-i\left(\frac{a}{2}(k_x-k_y)\right)} + e^{-i\left(\frac{a}{2}(k_x+k_y)\right)} + e^{-i\left(\frac{a}{2}(-k_x+k_y)\right)} + e^{-i\left(\frac{a}{2}(-k_x-k_y)\right)} + e^{-i\left(\frac{a}{2}(-k_y+k_z)\right)} - e^{-i\left(\frac{a}{2}(k_y+k_z)\right)} + e^{-i\left(\frac{a}{2}(k_y-k_z)\right)} - e^{-i\left(\frac{a}{2}(-k_y-k_z)\right)}\right] \tag{23}$$

$$D = 4\alpha_1 cos\left(\frac{a}{4}k_x\right)cos\left(\frac{a}{4}k_y\right)cos\left(\frac{a}{4}k_z\right) + i\left[4\alpha_1 sin\left(\frac{a}{4}k_x\right)sin\left(\frac{a}{4}k_y\right)sin\left(\frac{a}{4}k_z\right)\right] \tag{24}$$

$$E = \beta_1 \left[e^{-i\left(\frac{a}{4}(k_x+k_y+k_z)\right)} - e^{-i\left(\frac{a}{4}(k_x-k_y-k_z)\right)} - e^{-i\left(\frac{a}{4}(-k_x+k_y-k_z)\right)} + e^{-i\left(\frac{a}{4}(-k_x-k_y+k_z)\right)} \right] \tag{25}$$

$$F = \beta_1 \left[e^{-i\left(\frac{a}{4}(k_x+k_y+k_z)\right)} - e^{-i\left(\frac{a}{4}(k_x-k_y-k_z)\right)} + e^{-i\left(\frac{a}{4}(-k_x+k_y-k_z)\right)} - e^{-i\left(\frac{a}{4}(-k_x-k_y+k_z)\right)} \right] \tag{26}$$

$$G = \nu_2 \left[-e^{-i\left(\frac{a}{2}(k_x-k_y)\right)} + e^{-i\left(\frac{a}{2}(k_x+k_y)\right)} - e^{-i\left(\frac{a}{2}(-k_x+k_y)\right)} + e^{-i\left(\frac{a}{2}(-k_x-k_y)\right)} \right] +$$
$$\delta_2 \left[e^{-i\left(\frac{a}{2}(-k_y+k_z)\right)} + e^{-i\left(\frac{a}{2}(k_y+k_z)\right)} - e^{-i\left(\frac{a}{2}(k_y-k_z)\right)} - e^{-i\left(\frac{a}{2}(-k_y-k_z)\right)} + e^{-i\left(\frac{a}{2}(-k_x-k_z)\right)} - \right.$$
$$\left. e^{-i\left(\frac{a}{2}(-k_x+k_z)\right)} - e^{-i\left(\frac{a}{2}(k_x+k_z)\right)} + e^{-i\left(\frac{a}{2}(k_x-k_z)\right)} \right] \tag{27}$$

$$H = \alpha_0 + \mu_2 \left[4cos\left(\frac{a}{2}k_x\right) cos\left(\frac{a}{2}k_y\right) + 4cos\left(\frac{a}{2}k_y\right) cos\left(\frac{a}{2}k_z\right) \right] +$$
$$\lambda_2 \left[4cos\left(\frac{a}{2}k_x\right) cos\left(\frac{a}{2}k_z\right) \right] \tag{28}$$

$$I = \nu_2 \left[-e^{-i\left(\frac{a}{2}(-k_y+k_z)\right)} + e^{-i\left(\frac{a}{2}(k_y+k_z)\right)} - e^{-i\left(\frac{a}{2}(k_y-k_z)\right)} + e^{-i\left(\frac{a}{2}(-k_y-k_z)\right)} \right] +$$
$$\delta_2 \left[e^{-i\left(\frac{a}{2}(k_x-k_y)\right)} + e^{-i\left(\frac{a}{2}(k_x+k_y)\right)} - e^{-i\left(\frac{a}{2}(-k_x+k_y)\right)} - e^{-i\left(\frac{a}{2}(-k_x-k_y)\right)} + e^{-i\left(\frac{a}{2}(-k_x-k_z)\right)} + \right.$$
$$\left. e^{-i\left(\frac{a}{2}(-k_x+k_z)\right)} - e^{-i\left(\frac{a}{2}(k_x+k_z)\right)} - e^{-i\left(\frac{a}{2}(k_x-k_z)\right)} \right] \tag{29}$$

$$L = \beta_1 \left[e^{-i\left(\frac{a}{4}(k_x+k_y+k_z)\right)} + e^{-i\left(\frac{a}{4}(k_x-k_y-k_z)\right)} - e^{-i\left(\frac{a}{4}(-k_x+k_y-k_z)\right)} - e^{-i\left(\frac{a}{4}(-k_x-k_y+k_z)\right)} \right] \tag{30}$$

$$M = \nu_2 \left[e^{-i\left(\frac{a}{2}(-k_x-k_z)\right)} - e^{-i\left(\frac{a}{2}(-k_x+k_z)\right)} + e^{-i\left(\frac{a}{2}(k_x+k_z)\right)} - e^{-i\left(\frac{a}{2}(k_x-k_z)\right)} \right] + \delta_2 \left[e^{-i\left(\frac{a}{2}(k_x-k_y)\right)} - \right.$$
$$\left. e^{-i\left(\frac{a}{2}(k_x+k_y)\right)} - e^{-i\left(\frac{a}{2}(-k_x+k_y)\right)} + e^{-i\left(\frac{a}{2}(-k_x-k_y)\right)} - e^{-i\left(\frac{a}{2}(-k_y+k_z)\right)} + e^{-i\left(\frac{a}{2}(k_y+k_z)\right)} + \right.$$
$$\left. e^{-i\left(\frac{a}{2}(k_y-k_z)\right)} - e^{-i\left(\frac{a}{2}(-k_y-k_z)\right)} \right] \tag{31}$$

$$N = \nu_2\left[-e^{-i\left(\frac{a}{2}(-k_y+k_z)\right)} + e^{-i\left(\frac{a}{2}(k_y+k_z)\right)} - e^{-i\left(\frac{a}{2}(k_y-k_z)\right)} + e^{-i\left(\frac{a}{2}(-k_y-k_z)\right)}\right] + \delta_2\left[-e^{-i\left(\frac{a}{2}(k_x-k_y)\right)} - e^{-i\left(\frac{a}{2}(k_x+k_y)\right)} + e^{-i\left(\frac{a}{2}(-k_x+k_y)\right)} + e^{-i\left(\frac{a}{2}(-k_x-k_y)\right)} - e^{-i\left(\frac{a}{2}(-k_x-k_z)\right)} - e^{-i\left(\frac{a}{2}(-k_x+k_z)\right)} + e^{-i\left(\frac{a}{2}(k_x+k_z)\right)} + e^{-i\left(\frac{a}{2}(k_x-k_z)\right)}\right]$$

(32)

$$O = \alpha_0 + \mu_2\left[4cos\left(\frac{a}{2}k_y\right)cos\left(\frac{a}{2}k_z\right) + 4cos\left(\frac{a}{2}k_x\right)cos\left(\frac{a}{2}k_z\right)\right] + \lambda_2\left[4cos\left(\frac{a}{2}k_x\right)cos\left(\frac{a}{2}k_y\right)\right]$$

(33)

For a given wavevector, there exist six solutions of the dynamical matrix for the frequencies that satisfy the equations of motion. These are the eigenvalues of the dynamical matrix and represent the six phonon modes (or polarizations). They consist of the two transverse acoustic (TA1, TA2), the longitudinal acoustic (LA), the two transverse optical (TO1, TO2), and the longitudinal optical (LO) mode.

4.2 Dispersion – Implementation

The lattice dynamics model described in the preceding section can be used to calculate the frequencies of the six modes corresponding to any given wavevector. The SPTM, is implemented on a uniform discretization of wavevector (k) space. This dissertation uses a mesh size of 14. This value was chosen based upon three phonon scattering considerations and is discussed in section 4.4. A mesh size of 14 implies that the principle directions within the wavevector space are divided into 14 equal sized elements. This is shown in three dimensions for one eighth (one octant) of the FBZ with the Fig. 21.

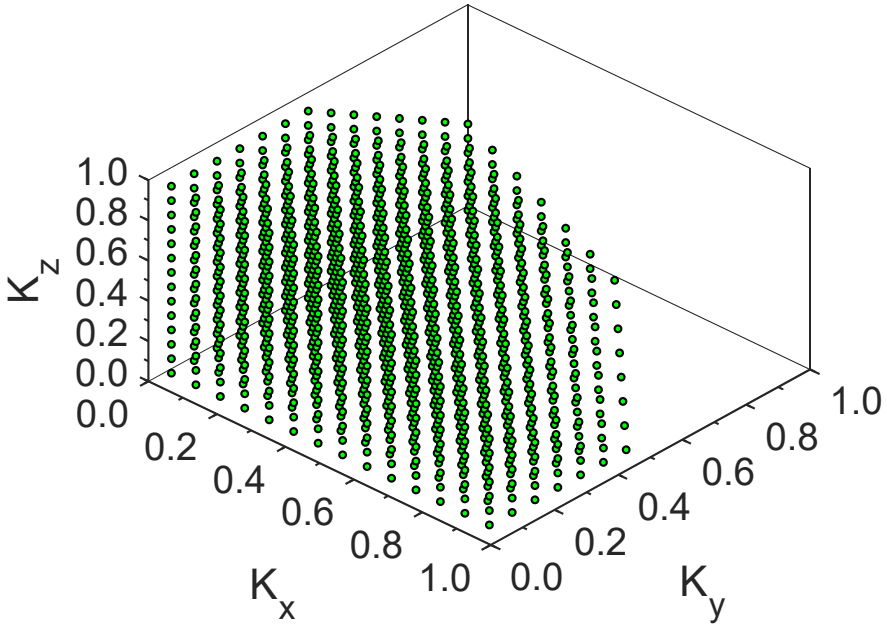

Fig. 21. Discretization of one octant of wavevector space for a mesh size of 14. Normalized wavevectors in the x, y, and z directions are shown. The respective pseudostates are illustrated with green circles.

The wavevector space elements are labeled by the location of their centroids. With the mesh size chosen, there are 10,976 elements in the FBZ. The lattice dynamics model is applied to calculate the six representative frequencies at the centroids of the elements. The wavevector and frequency values associated with the centroid points are used as labels and unique combinations of wavevector centroid and calculated frequency are referred to as pseudostates. There are 65,856 pseudostates in the FBZ for the chosen mesh size. For a mesh size of 12 there are 41,472 pseudostates and for a mesh size of 16 there are 98,304 pseudostates. Dispersion calculations are performed at each of the six faces of the wavevector space volume elements in addition to the centroid. Thus, for an implementation of the dispersion calculation on a mesh size of 14, there are seven solutions of equation 20 generated in complex double precision for each of the 65,856 pseudostates. This results in 460,992 instances of equation 20 that are solved through the use of the GNU Scientific Library (GSL) open source software package [80]. This package contains a complex eigenvalue solver. The GSL complex eigenvalue solver uses the complex form of the symmetric bi-diagonalization and QR reduction method. This method is assumed to take on the order of N^3 calculations [81]. Thus for the mesh size of 14, on the order of 10^8 computations would be involved for the dispersion calculations.

Values of the interatomic force constants that were implemented in the solution of the dynamical matrix for the calculation of dispersion relationships in pure silicon are shown with Table 4. The values for germanium are shown as well and could be implemented to compute dispersion relations for pure germanium.

Table 4. Interatomic Force Constants in units of N/m [79]

	Silicon	Germanium
α_0	215.41173	185.33255
α_1	-52.54514	-45.88164
β_1	-36.64926	-32.63248
μ_2	-2.92696	-2.31977
ν_2	-2.83355	-2.10181
δ_2	1.72815	1.38563
λ_2	6.69464	6.00961

The value of μ_2 for silicon was adjusted to -4.001216 N/m to ensure enforcement of the acoustic sum rule when truncating the interactions to second nearest neighbors. This rule implies the following when using interatomic force constants up to second nearest neighbors [82].

$$\alpha_0 = -4\alpha_1 - 8\mu_2 - 4\lambda_2 \tag{34}$$

The solutions from the dispersion calculations need only be computed one time for a given mesh discretization and are stored in a look-up table for future use in both scattering and drift algorithms. The group velocities are calculated using a finite difference method to solve equation 9 in each of the coordinate directions with knowledge of the frequencies and wavevectors at each of the six faces of a pseudostate. Group velocities are used when considering the drift (unimpeded movement) of phonons between different geometric cells. The wavevector and frequency will be used in both the selection of three phonon scattering partners and the calculation of the three phonon scattering rates. Results of the dispersion implementation are shown in section 5.1.

4.3 Three Phonon Scattering - Theory

Macroscopically we know, by Newton's 1st Law, that if an object is traveling in a straight line then it takes some interaction with the surroundings to change its trajectory. This is similar to quantum objects (like phonons or photons) in the sense that it takes a change in interaction from the surroundings to change state (trajectory). However, because of the quantum nature of the objects (wave particle duality), interaction with the surroundings is not a guarantee of a change in state. All that can be predicted is the likelihood of the state changing. This likelihood is dependent on the strength of the interaction. To predict the likelihood of an event occurring, we must be able to predict how the quantum state that represents the object or system changes with time. This involves solving the Schrodinger equation for a mathematical object called the state vector. The Schrodinger equation is shown in equation 35 [83],

$$i\hbar \frac{\partial \Psi(x,t)}{\partial t} = H\Psi(x,t) \ , \tag{35}$$

where, i is the imaginary number, $\hbar$ is modified Plank's constant, Ψ is the state vector (expressed in the position space representation it is also known as the wave function), and H is the Hamiltonian operator. The Hamiltonian operator represents the total energy of the system (kinetic and potential) and in that regard all of interactions with the surrounding. It is a differential operator that takes the following form with equation 36,

$$H(\cdot) = -\frac{\hbar^2}{2m}\nabla^2(\cdot) + V(x)(\cdot) \ , \tag{36}$$

where, m is the mass of the object or system, $\nabla^2$is the Laplacian differential operator and V is the potential energy associated with the location of the mass in a surrounding force field. The state vector Ψ is typically solved for by a separation of variables where it is expressed as a product of a time dependent piece and a position dependent piece. Thus it takes the following form in equation 37,

$$\Psi(x,t) = \psi(x)\phi(t) \ , \tag{37}$$

where, ψ is the position dependent function and ϕ is the time dependent function. Substituting this form of the state vector into the Schrodinger equation and dividing by the quantity $\psi\phi$ it can be shown that equation 38 results.

$$i\hbar \frac{1}{\phi}\frac{d\phi}{dt} = -\frac{\hbar^2}{2m}\frac{1}{\psi}\frac{d^2\psi}{dx^2} + V(x) \tag{38}$$

As Griffiths [84] noted, the left hand side of equation 38 is a function of time alone and the right hand side is a function of space alone. The only way that this can be true is if both sides are a constant. This constant will be denoted with E as it will ultimately represent the possible values of measurement of the energy and this results in equations 39 and 40.

$$i\hbar \frac{1}{\phi}\frac{d\phi}{dt} = E \tag{39}$$

$$E = -\frac{\hbar^2}{2m}\frac{1}{\psi}\frac{d^2\psi}{dx^2} + V \tag{40}$$

The first equation is solved to produce the following result with equation 41.

$$\phi(t) = e^{-iEt/\hbar} \tag{41}$$

The other equation is referred to as the time independent Schrodinger equation, often written as in equation 42.

$$H(\psi) = E\psi \tag{42}$$

Its solutions, ψ, are of interest as they are stationary states, states of definite energy, orthogonal, and they serve as basis states to express any general solution to the Schrodinger equation. That is, any solution to the time dependent Schrodinger equation can be expressed as in equation 43,

$$\Psi(x,t) = \sum_n C_n \psi_n(x) e^{-iE_n t/\hbar} \ , \tag{43}$$

where $\Psi(\mathrm{x},\mathrm{t})$ is the time and space dependent state vector, $\psi_n(x)$ are the possible solutions to the time independent Schrodinger equation, $e^{-iE_n t/\hbar}$ is the time dependent piece mentioned above, and E_n are the energy levels associated with the basis states.

The expansion coefficients,C_n, are related to the probability of measuring a value of energy corresponding to E_n if the system is represented by the state $\Psi(\mathrm{x},\mathrm{t})$. The values of the expansion coefficients are computed from the initial condition of the object or system. Subject to a Hamiltonian that does not vary with time (i.e. the potential energy piece does not vary with time), the values of the expansion coefficients will also not change with time and the expectation or average values of physically observable quantities will also not change with time.
In dynamical situations, the Hamiltonian can vary with time. To allow for the prediction of scattering events or transitions in state, we must allow for a time dependent Hamiltonian [84]. This implies that it takes a change in the Hamiltonian (interactions with surroundings) to cause a transition to other states or a scattering event. To handle the time variation, the Hamiltonian is usually expressed as the sum of a time independent piece and a time dependent piece as in equation 44.

$$H = H_0 + H'(t) \tag{44}$$

Subject to the time variation of the Hamiltonian, the expansion coefficients can now vary in time. As the expansion coefficients completely specify the dynamics of the state vector and thus the system it represents solving for them amounts to solving the Schrodinger equation. A Schrodinger-like equation for the expansion coefficients can be developed by substituting equations 43 and 44 into equation 35. This leaves equation 45.

$$i\hbar \frac{\partial}{\partial t}\left[\sum_n C_n(t)\psi_n(x)e^{-iE_n t/\hbar}\right] = (H_0 + H'(t))\sum_n C_n(t)\psi_n(x)e^{-iE_n t/\hbar} \tag{45}$$

After manipulation, this leaves equation 46.

$$i\hbar \sum_n \left[\frac{d}{dt}C_n(t)\psi_n(x)e^{-\frac{iE_n t}{\hbar}} + C_n(t)\psi_n(x)\left(\frac{-iE_n}{\hbar}\right)e^{-\frac{iE_n t}{\hbar}}\right] = \sum_n \left(H_0 C_n(t)\psi_n(x)e^{-\frac{iE_n t}{\hbar}} + H'(t)C_n(t)\psi_n(x)e^{-\frac{iE_n t}{\hbar}}\right) \tag{46}$$

Making note of equation 42, the last term on the left hand side will cancel the first term on the right. This leaves equation 47.

$$i\hbar \sum_n \left[\frac{d}{dt}C_n\psi_n(x)e^{-\frac{iE_n t}{\hbar}}\right] = \sum_n \left(H'(t)C_n\psi_n(x)e^{-\frac{iE_n t}{\hbar}}\right) \tag{47}$$

Now, a standard trick is used where the inner product of both sides of equation 47 is taken with respect to $\psi_m(x)$. The orthogonality of $\psi_m(x)$ is also noted with equation 48.

$$\langle\psi_m|\psi_n\rangle = \delta_{mn} \tag{48}$$

Utilizing these facts, equation 47 becomes equation 49,

$$i\hbar \frac{d}{dt}C_m = \sum_n \left(\langle\psi_m(x)|H'(t)|\psi_n(x)\rangle C_n e^{-\frac{i(E_n - E_m)t}{\hbar}}\right) \ , \tag{49}$$

where $\langle\psi_m(x)|\mathrm{H}'(\mathrm{t})|\psi_n(x)\rangle$ is referred to as the matrix element or transition amplitude as it connects the states n and m. It is related to the probability of transition between the states n and m caused by the perturbation $H'(t)$. Equation 49 in terms of the expansion coefficients is exact and equivalent to the Schrodinger equation. If $H'(t)$ is relatively small compared to H_0 an approximation method called first order perturbation expansion is used to determine the expansion coefficients. This amounts to using successively more complex assumptions to approximate the solution. The zeroth order approximation is used to estimate the first order value of the coefficients. That is,

$$i\hbar\frac{d}{dt}C_m^{p+1} = \sum_n\left(\langle\psi_m(x)|H'(t)|\psi_n(x)\rangle C_n^p e^{-\frac{i(E_n-E_m)t}{\hbar}}\right), \tag{50}$$

where p is the order of the approximation. At the zeroth order, C_n^p is assumed to be a constant value equal to 1. This amounts to assuming that we start in state described by C_n and all of the other expansion coefficients at the zeroth order are zero. Separating and integrating, results in the following expression for the first order expansion coefficients with equation 51:

$$C_m^{p+1} \cong \frac{-i}{\hbar}\int_0^t\langle\psi_m(x)|H'(t)|\psi_n(x)\rangle e^{-\frac{i(E_n-E_m)t}{\hbar}}dt \tag{51}$$

Assuming that that perturbing Hamiltonian "turns on" at time zero and remains constant over the time interval, it can be shown that equation 51 becomes equation 52.

$$C_m^{p+1} \cong \frac{-i}{\hbar}\langle\psi_m(x)|H'(t)|\psi_n(x)\rangle\frac{e^{\frac{-i(E_n-E_m)t}{\hbar}}-1}{(E_n-E_m)/\hbar} \tag{52}$$

The probability that the state undergoes a transition from n to m due to the perturbing Hamiltonian is then the squared modulus of equation 51. We will now drop the superscript (p+1) assuming that we are stopping the expansion at first order:

$$P_m(t) = |C_m(t)|^2 \cong \frac{1}{\hbar^2}|\langle\psi_m(x)|H'(t)|\psi_n(x)\rangle|^2\left[\frac{e^{\frac{-i(E_n-E_m)t}{\hbar}}-1}{(E_n-E_m)/\hbar}\right]\left[\frac{e^{\frac{i(E_n-E_m)t}{\hbar}}-1}{(E_n-E_m)/\hbar}\right] \tag{53}$$

$$P_m(t) = |C_m(t)|^2 \cong \frac{1}{\hbar^2}|\langle\psi_m(x)|H'(t)|\psi_n(x)\rangle|^2\frac{1-e^{\frac{-i(E_n-E_m)t}{\hbar}}-e^{\frac{i(E_n-E_m)t}{\hbar}}+1}{[(E_n-E_m)/\hbar]^2} \tag{54}$$

$$P_m(t) = |C_m(t)|^2 \cong \frac{1}{\hbar^2}|\langle\psi_m(x)|H'(t)|\psi_n(x)\rangle|^2\frac{2-2cos(\frac{(E_n-E_m)t}{\hbar})}{[(E_n-E_m)/\hbar]^2} \tag{55}$$

Equation 55 represents the probability of state transition. To predict the rate at which transitions occur, we take the time derivative of equation 55 and obtain equation 56.

$$\dot{P}_{n-m} = \frac{d}{dt}|C_m(t)|^2 \cong \frac{2}{\hbar^2}|\langle\psi_m(x)|H'(t)|\psi_n(x)\rangle|^2\frac{sin(\frac{(E_n-E_m)t}{\hbar})}{(E_n-E_m)/\hbar} \tag{56}$$

Phonon transitions occur between states where energy is conserved. That is, $\mathrm{E_m} - \mathrm{E_n}$ approaches zero. The limiting behavior of the $\frac{sin(\frac{(\mathrm{E_n}-\mathrm{E_m})t}{\hbar})}{(\mathrm{E_n}-\mathrm{E_m})/\hbar}$ term, as the energy difference approaches zero and the time goes to infinity, approaches the value of $\pi\hbar\delta(\mathrm{E_n} - \mathrm{E_m})$. This enforces energy conservation and leads to equation 57.

$$\dot{P}_{n-m} \cong \frac{2\pi}{\hbar}|\langle\psi_m(x)|H'(t)|\psi_n(x)\rangle|^2\delta(E_n - E_m) \tag{57}$$

Equation 57 is known as Fermi's Golden Rule and it can be applied to predict scattering probabilities for both three phonon scattering and electron-phonon scattering. Its application to

the three phonon interaction involves some modification. The initial state is represented as the state where three phonons are present and the final state is one in which the population of the phonons either decreases or increases based on the type of event. These states are shown with equations 58 – 60 [85].

$$|\psi_n(x)\rangle = |\, n_{ks}, n_{k\prime s\prime}, n_{k"s"}\rangle \tag{58}$$

$$|\psi_m(x)\rangle_{Type\ I} = |\, n_{ks} - 1, n_{k's'} - 1, n_{k"s"} + 1\rangle \tag{59}$$

$$|\psi_m(x)\rangle_{Type\ II} = |\, n_{ks} + 1, n_{k's'} + 1, n_{k"s"} - 1\rangle \tag{60}$$

The states are identified with the occupation number, n_{ks} as identified in equation 8. It is analogous to the number that labels the excitation level in the simple harmonic oscillator. In addition to specifying the initial and final states, the perturbing Hamiltonian must be specified for use in Fermi's Golden Rule. For the three phonon interaction this is the deviation in the interatomic potential from harmonic. Typically, the interatomic potential is expressed as a Taylor series expansion about the equilibrium position of the atoms. This can be expressed as equation 61 [57],

$$V = V_o + \sum_i \Pi_i u_i + \frac{1}{2!}\sum_{ij} \Phi_{ij} u_i u_j + \frac{1}{3!}\sum_{ijk} \Psi_{ijk} u_i u_j u_k + \cdots \tag{61}$$

where u_i is the displacement of the atom at location i about its equilibrium position and, Π_i, Φ_{ij}, Ψ_{ijk} are known as the interatomic force constants (Φ_{ij} is analogous to α_0 from the dispersion calculations). They are related to the first, second, and third derivative of the interatomic potential respectively. We are interested in only the third order term for the perturbing Hamiltonian (or deviation from the harmonic approximation). The classical expression for this is shown with equation 62 [54]:

$$H'(t) = \frac{1}{3!}\sum_{ijk} \Psi_{ijk} u_i u_j u_k \tag{62}$$

Specification of the perturbing Hamiltonian in a form appropriate for use in Fermi's Golden Rule involves promotion of the displacement variables to quantum mechanical operators. This is defined in equation 63 [53],

$$u_{lx} = \frac{1}{\sqrt{N}}\sum_{ks} \left(\frac{\hbar}{2M\omega(k)}\right)^{1/2} \left(a_{ks}^{\dagger} - a_{ks}\right) e^{-i\boldsymbol{k}\cdot\boldsymbol{l}} \tag{63}$$

where M is the atomic mass, N is the number of normal modes over which the summation is performed, $\omega(k)$ is the frequency associated with phonon mode k, $a_{ks}^{\dagger}$ is the phonon creation operator that creates of phonon of wavevector k and polarization s, a_{ks} is the phonon annihilation operator that destroys a phonon with wavevector k and polarization s, and l is a lattice vector. Substituting the definition of the displacement operator from equation 63, it can be shown [53] that the perturbing Hamiltonian of equation 62 becomes equation 64.

$$H'(t) = \sum_{\substack{l\, l'\\ l"}} \sum_{kk'k''} \frac{1}{3!}\left(\frac{\hbar^3}{8M^3N^3\omega(k)\omega\prime(k\prime)\omega"(k")}\right)^{1/2} \Psi_{ijk}\left(a_{ks}^{\dagger} - a_{ks}\right)\left(a_{k\prime s}^{\dagger} - a_{k\prime s}\right)\left(a_{k"s}^{\dagger} - a_{k"s}\right) e^{i\boldsymbol{k}\cdot\boldsymbol{l}} e^{i\boldsymbol{k'}\cdot\boldsymbol{l\prime}} e^{i\boldsymbol{k''}\cdot\boldsymbol{l"}} \tag{64}$$

Equation 64 involves summations over the three wavevectors of phonons involved in the scattering event and summation over the locations of the three adjacent atoms of the lattice (labeled by lattice vectors to their locations l, l', and l"). This can be further simplified by considering that the above expression should be invariant under translation. That is, if we add a

lattice vector (move to a different spot in the crystal) the results should be unchanged. Thus, if we add a lattice vector l to each one of the lattice vectors l, l' and l" the following term is introduced:

$$\frac{1}{N}\sum_l e^{i(\boldsymbol{k}+\boldsymbol{k}'+\boldsymbol{k}")\cdot l} \tag{65}$$

This expression is zero unless $\mathbf{k}+\mathbf{k}'+\mathbf{k}"$ is equal to zero or a reciprocal lattice vector (G). This amounts to a delta function that has the effect of conserving momentum. In addition, we can take the origin of our lattice to be at position l. Equation 64 is them simplified to equation 66.

$$H'(t) = \sum_{\substack{l\,l'\\ l"}} \sum_{kk'k''} \frac{1}{3!}\left(\frac{\hbar^3}{8M^3N\omega(k)\omega'(k')\omega"(k")}\right)^{1/2} \Psi_{ijk}\left(a_{ks}^\dagger - a_{ks}\right)\left(a_{k's}^\dagger - a_{k's}\right)\left(a_{k"s}^\dagger - a_{k"s}\right) e^{i\boldsymbol{k}'\cdot\boldsymbol{l}'} e^{i\boldsymbol{k}''\cdot\boldsymbol{l}"} \delta_{k+k'+k''+G} \tag{66}$$

Substituting into Fermi's Golden Rule (equation 57) for a Type I interaction, equation 67 results.

$$\dot{P}_{n-m} \cong \frac{2\pi}{\hbar}\left|\langle\psi_m(x)|\sum_{\substack{l\,l'\\ l"}} \sum_{kk'k''} \frac{1}{3!}\left(\frac{\hbar^3}{8M^3N\omega(k)\omega'(k')\omega"(k")}\right)^{1/2} \Psi_{ijk}\left(a_{ks}^\dagger - a_{ks}\right)\left(a_{k's}^\dagger - a_{k's}\right)\left(a_{k"s}^\dagger - a_{k"s}\right) e^{i\boldsymbol{k}\cdot\boldsymbol{l}} e^{i\boldsymbol{k}'\cdot\boldsymbol{l}'} e^{i\boldsymbol{k}''\cdot\boldsymbol{l}"} \delta_{k+k'+k''+G}\,|\psi_n(x)\rangle\right|^2 \delta(E_n - E_m) \tag{67}$$

A slight simplification produces equation 68.

$$\dot{P}_{n-m} \cong \frac{2\pi}{\hbar}\left\{\sum_{\substack{l\,l'\\ l"}} \sum_{kk'k''} \frac{1}{3!}\left(\frac{\hbar^3}{8M^3N\omega(k)\omega'(k')\omega"(k")}\right)^{1/2} \Psi_{ijk} e^{i\boldsymbol{k}\cdot\boldsymbol{l}} e^{i\boldsymbol{k}'\cdot\boldsymbol{l}'} e^{i\boldsymbol{k}''\cdot\boldsymbol{l}"} \delta_{k+k'+k''+G}\,\delta(E_n - E_m)\right\}^2 \left|\langle\psi_m(x)|\left(a_{ks}^\dagger - a_{ks}\right)\left(a_{k's}^\dagger - a_{k's}\right)\left(a_{k"s}^\dagger - a_{k"s}\right)|\psi_n(x)\rangle\right|^2 \tag{68}$$

Evaluation of the squared modulus, requires knowledge of how the annihilation and creation operators act on the three phonon state. This is shown with equations 69 – 70.

$$a_{ks}^\dagger|\, n_{ks}, n_{k's'}, n_{k"s"}\rangle = (\, n_{ks}+1)^{1/2}|\, n_{ks}+1, n_{k's'}, n_{k"s"}\rangle \tag{69}$$

$$a_{ks}|\, n_{ks}, n_{k's'}, n_{k"s"}\rangle = (n_{ks})^{1/2}|\, n_{ks}-1, n_{k's'}, n_{k"s"}\rangle \tag{70}$$

Enforcing orthogonality of the state vectors implies that the only terms that will survive the inner product are the ones where the groups of three operators act on the initial state to produce the final state. For a Type I event, there are only six terms in the summation over the wavevectors (k, k' and k") that result in a non-zero inner product. They also all produce the same value and an example of this for a Type I event is shown in equation 71 [66].

$$\begin{aligned}
&\langle\, n_{ks}-1, n_{k's'}-1, n_{k"s"}+1|a_{ks}a_{k's'}a_{k"s"}^\dagger|\, n_{ks}, n_{k's'}, n_{k"s"}\rangle \\
&= \langle\, n_{ks}-1, n_{k's'}-1, n_{k"s"}+1|\,(n_{ks})^{\frac{1}{2}}\,(n_{k's'})^{\frac{1}{2}}\,(\, n_{k"s"}+1)^{\frac{1}{2}}\,|\, n_{ks}-1, n_{k's'}-1, n_{k"s"}+1\rangle \\
&= (n_{ks})^{\frac{1}{2}}\,(n_{k's'})^{\frac{1}{2}}(\, n_{k"s"}+1)^{\frac{1}{2}}\langle\, n_{ks}-1, n_{k's'}-1, n_{k"s"}+1||\, n_{ks}-1, n_{k's'}-1, n_{k"s"}+1\rangle \\
&= (n_{ks})^{\frac{1}{2}}\,(n_{k's'})^{\frac{1}{2}}(\, n_{k"s"}+1)^{\frac{1}{2}}
\end{aligned} \tag{71}$$

Thus, the transition rate for a Type I scattering event becomes equation 72.

$$\dot{P}_{n-m} \cong \frac{\pi}{\hbar}\frac{1}{3!^2}\frac{\hbar^2}{4M^3N\omega(k)\omega\prime(k\prime)\omega"(k")}\sum_l\left(\Psi_{ijk}e^{i\mathbf{k}\cdot l}e^{i\mathbf{k}'\cdot \mathbf{l}'}e^{i\mathbf{k}''\cdot \mathbf{l}"}\right)^2 n_{ks}n_{k's'}(n_{k"s"}+1)\,\delta(\omega(\mathrm{k})-\omega'(k')-\omega(k)) \quad (72)$$

Prior to implementation of the above equation, the anharmonic strength term (the Fourier transform of the third order derivative of the interatomic potential) must be specified. This work will approximate the term $\Psi_{\mathrm{ijk}}e^{\mathbf{i}\mathbf{k}\cdot\mathbf{l}}e^{\mathbf{i}\mathbf{k}'\cdot\mathbf{l}'}e^{\mathbf{i}\mathbf{k}''\cdot\mathbf{l}"}$ using the Gruneisen parameter [57]. This is shown in equation 73,

$$\sum_l \Psi_{ijk}e^{i\mathbf{k}\cdot l}e^{i\mathbf{k}'\cdot \mathbf{l}\prime}e^{i\mathbf{k}''\cdot \mathbf{l}"} \cong \frac{-6\gamma_{ks}M\omega"(k")^2}{a} \quad (73)$$

where γ_{ks} is the Gruneisen parameter, M is the atomic mass, $\omega"(k")$ is the frequency of the third phonon partner and a is the lattice constant. The Gruneisen parameter is directly related to the change in normal mode frequency due to a change in the lattice constant of the crystal thus, it is physically reasonable to use this parameter to estimate the anharmonic scattering strength as it is directly related to the anharmonic nature of the interatomic potential. (That being said, the Gruneisen parameter will be used as an adjustable parameter to ensure that three phonon scattering rates are consistent with physical expectations and higher fidelity published work.) The transition rate for a Type I interaction becomes equation 74.

$$\dot{P}_{n-m} \cong \frac{\pi\hbar}{4M^3N\omega(k)\omega\prime(k\prime)\omega"(k")}\left(\frac{\gamma_{ks}^2M^2\omega"(k")^4}{a^2}\right)n_{ks}n_{k\prime s\prime}(n_{k"s"}+1)\delta(\omega(\mathrm{k})-\omega'(k')-\omega(k)) \quad (74)$$

The SPT Model of Brown III and Hensel [9] computed an interaction table for use in three phonon scattering implementation. This interaction table consists of pseudostates that can participate in three phonon scattering events based on the selection rules for energy and momentum conservation. As mentioned in section 4.2, each pseudostate represents a volume in wavevector space. For a given scattering interaction the scattering rate equation, as in the form of equation 74, can be thought of as the scattering rate per unit volume in real space and in wave vector space. To account for application of pseudostates, the scattering rate must be modified and this amounts to the following manipulation.

$$\dot{P}_{n-m} \cong \frac{\pi\hbar}{4M^3N\omega(k)\omega\prime(k\prime)\omega"(k")}\left(\frac{\gamma_{ks}^2M^2\omega"(k")^4}{a^2}\right)n_{ks}n_{k\prime s\prime}(n_{k"s"}+1)\sum_{k-volume}\delta(\omega(\mathrm{k})-\omega'(k')-\omega"(k")) \quad (75)$$

The summation can be transformed to an integral in wavevector space as in equation 76.

$$\dot{P}_{n-m} \cong \frac{\pi\hbar}{4M^3N\omega(k)\omega\prime(k\prime)\omega"(k")}\left(\frac{\gamma_{ks}^2M^2\omega"(k")^4}{a^2}\right)n_{ks}n_{k\prime s\prime}(n_{k"s"}+1)\int\frac{V}{(2\pi)^3}\delta(\omega(\mathrm{k})-\omega'(k')-\omega"(k"))d\boldsymbol{k} \quad (76)$$

The integral of the delta function over the region in wavevector space can be changed to an integral over a surface in wavevector space where the frequency is within an infinitesimal band and thus energy conservation is satisfied. The following substitution (equation 77) can be made [68],

$$\int_k\frac{V}{(2\pi)^3}\delta(\omega(\mathrm{k})-\omega'(k')-\omega"(k"))d\boldsymbol{k}=\int_\omega\frac{V}{(2\pi)^3}\delta(\omega(\mathrm{k})-\omega'(k')-\omega"(k"))\frac{dSdkd\omega}{d\omega} \quad , \quad (77)$$

where, V is the volume of the crystal, $\frac{\mathrm{d}\omega}{dk}$ is the group velocity (v_g) and S is a surface in momentum space of constant wavevector. The integral of the delta function with respect to frequency becomes unity and equation 76 becomes equation 78.

$$\dot{P}_{n-m} \cong \frac{\pi\hbar}{4M^3N\omega(k)\omega\prime(k\prime)\omega"(k")}\left(\frac{\gamma_{ks}^2M^2\omega"(k")^4}{a^2}\right)n_{ks}n_{k\prime s\prime}(n_{k"s"}+1)\frac{V}{(2\pi)^3}\int_{k-cell}\frac{dS}{v_g} \quad (78)$$

The remaining difficulty comes in evaluating the integral over the surface S. It is assumed the surface takes a spherical shape. Thus, the integral results in a portion of the surface area of a sphere that is contained within one of the volume elements in k-space. This surface area is approximated as the cross sectional area of a pseudostate volume element ($\Delta k_x \Delta k_y$).

4.4 Three-Phonon Scattering Implementation

Application of the scattering rate from Fermi's Golden Rule to calculate three phonon scattering within the framework of the statistical phonon transport model begins with computation of the available scattering partners within the geometric domain and the phase space that ensure both energy and momentum conservation. As was mentioned above, this is done through the creation of an interaction table that is pre-computed and stored for scattering calculations [9-11]. Computation of the interaction table starts with a search scheme applied to the discretized FBZ. In this initial step, the wavevector of the centroid of each element is compared to every other one in the FBZ to determine all of the combinations that conserve momentum. Because phonons are assumed to be evenly distributed over the k-space element, the size of the volume element must be taken into account when applying momentum conservation constraints. That is, it is possible for phonons that are relatively low in wavevector within each volume element to produce phonons outside of the resultant volume element if just centroids are considered. This is accounted for in the fact that each combination of two element partners can add to create one of eight possible outcomes. This is illustrated with a graphic showing interacting elements within the wavevector space in a two dimensional case with Fig. 22,

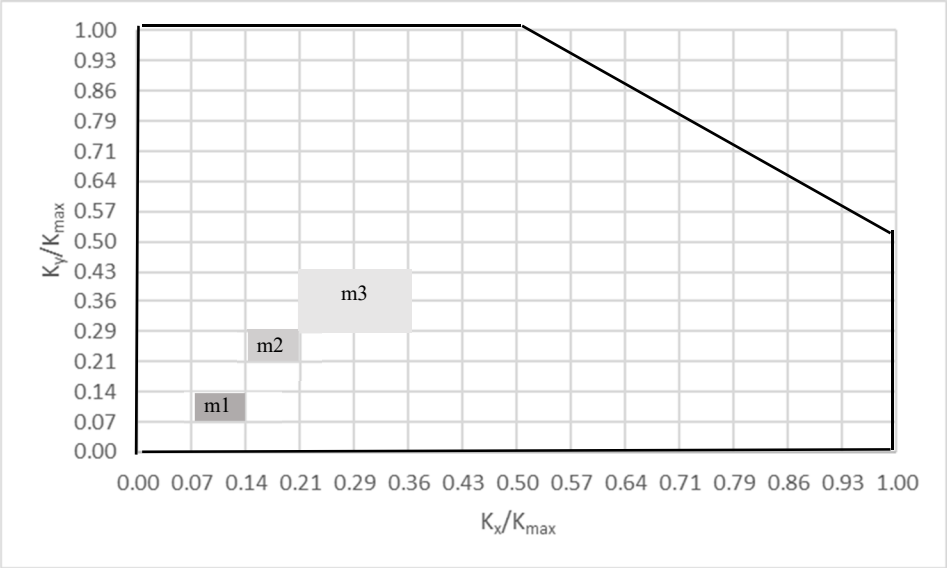

Fig. 22. Representation of a portion of the wavevector space to illustrate determination of interacting elements. Relative wavevectors in the x and y direction are shown. m1, m2, and m3 represent the three interacting elements. Adapted from [9].

where m1 and m2 indicate the two scattering partner elements that combine to produce possible elements within the m3 volume. Within the interaction search of the wavevector space, momentum conservation is ensured up to the addition of a reciprocal lattice vector (G) and both normal and Umklapp processes are considered. This amounts to enforcement of equation 10.

If an interaction is deemed to satisfy momentum conservation, it is then checked for energy conservation. This is done by comparing the frequencies of each of the six modes at the centroid of a given element to the frequencies of the modes corresponding to the centroids of the partner elements. Comparison of the frequencies to satisfy energy conservation involves the use of a pre-specified relative tolerance (ω_{eps}). This is illustrated with equation 79.

$$\frac{\omega^{"}(k^{"})-\omega'(k')-\omega(k)}{\omega^{"}(k^{"})} < \omega_{eps} \tag{79}$$

The interactions that are deemed to meet the criteria of equation 79 are included in the three phonon scattering interaction table. The number of interactions that result is directly dependent on the value of the tolerance. Too small of a tolerance will result in artificially limiting the number of interactions. And conversely, too large of a tolerance will allow too many interactions that will be both computationally intensive and induce non-physical results. Based on a sensitivity performed, this work selected a tolerance that was large enough to ensure that all pseudostates within the FBZ are ensured to have at least one scattering interaction. Thus, there are zero non-participating states. This ensures that the change in the population (number of phonons) of a given pseudostate will have a basis in the three phonon scattering physics discussed in the preceding section. The value used for the tolerance that meets this criteria is 2.75E-5, which is approximately five orders of magnitude less than the value of $\omega^{"}(k^{"})$. If a three phonon partner passes the energy and momentum checks, it is added to the interaction table and the process continues. The current work uses a table that involves 1,334,112 three phonon scattering interactions. It is noted that the value of the tolerance, ω_{eps}, should be dependent on the mesh size chosen to discretize the FBZ. At larger mesh values, the size of the volume element in wavevector (and therefore frequency) space will be smaller. This has the effect of enforcing a tighter tolerance on energy conservation and implies that the value of ω_{eps} could also be reduced to produce the same effect noted above in regards to ensuring that all pseudostates have at least one scattering interaction.

After computation of the available three phonon scattering partners, scattering is computed at each computational time step within the geometric domain of interest. Both the time step and the domain size (cell size) are variables that are set depending on multiple factors. These include computation stability, computation fidelity, and ensuring that no single phonon can traverse a single cell in a single time step. Thus, all phonons within the geometric cell are assumed to have the ability to participate in three phonon scattering. The equations for the scattering rates (Type I Rate and Type II Rate) computed from Fermi's Golden Rule (equation 78) are applied to each interaction listed in the interaction table. The value of the Gruneisen parameter used in the present work is 6.2. The scattering rates are directly dependent on the Gruneisen value and it was set to ensure an accurate representation of the three phonon scattering process.

Once scattering rates are computed for each three phonon scattering event, this allows for the computation of a probability of both a Type I and Type II interaction in the chosen time step. This probability is applied to the population of phonons associated with the least populated state involved in the interaction to compute the number of phonons created or phonons destroyed due to the single scattering event in a single time step. An illustration of the results of this calculation applied to three, three phonon interactions is shown in Table 5,

Table 5. Example of implementation of scattering equations in interaction table for three scattering events.

Partner 1			Partner 2			Partner 3			Type I Rate	Type II Rate	Phonons Created	Phonons Destroyed
k	ω	n	k'	ω'	n'	k"	ω"	n"				
(1/m)	(rad/s)	(-)	(1/m)	(rad/s)	(-)	(1/m)	(rad/s)	(-)	(1/s)	(1/s)	(#)	(#)
7.16E+08	2.50E+12	25.7	6.33E+09	2.12E+13	2.6	7.43E+09	2.37E+13	2.3	9.25E+09	9.25E+09	4.82E+01	4.82E+01
1.37E+09	4.86E+12	12.9	6.55E+09	8.67E+13	0.4	6.95E+09	9.15E+13	0.3	5.23E+09	5.24E+09	3.93E+00	3.94E+00
2.95E+09	2.38E+13	2.3	1.09E+10	6.46E+13	0.6	1.21E+10	8.84E+13	0.3	7.15E+08	7.15E+08	5.69E-01	5.69E-01

where the wavevector (k), frequency (ω), and occupation number of phonons (n) are shown for each of the three scattering partners involved in a given interaction. All possible events in the interaction table involving a given pseudostate are considered when determining the overall change in the population of that state. Thus, populations are updated with exact number of phonons created or destroyed and this redistribution of phonons from scattering is done within the phase space. This is in contrast to the Monte Carlo methods discussed in section 1.6 where phonons that are destroyed are eliminated from the domain and only a small fraction of the phonon population is represented. Results of the three phonon scattering implementation are illustrated in section 5.2.

4.5 Heat Generation Theory

Electron-phonon scattering is the source of thermal energy generation within transistors. Electrons, like phonons, can experience many interactions as they move through a material. Electron-phonon scattering is the only one that changes the net energy of the electron population as it results in energy transfer to the lattice [86]. The input of energy to the phonon population is primary due to the deformation potential interaction. With the deformation potential interaction, phonons are assumed to produce a uniform local deformation of the lattice. This local deformation of the electron cloud produces a change in energy that influences transport electrons. This is treated as a perturbation responsible for scattering and scattering rates can be computed from Fermi's Golden Rule in a manner similar to the calculation for three phonon scattering. Fermi's Golden Rule, initially shown with equation 57 is repeated below.

$$\dot{P}_{n-m} \cong \frac{2\pi}{\hbar} |\langle \psi_m | H' | \psi_n \rangle|^2 \delta(E_n - E_m), \tag{80}$$

$\dot{P}_{n-m}$ is the transition rate or probability per unit time of a transition from state labeled as $|\psi_n\rangle$ to $\langle \psi_m|$. The δ function is to ensure energy conservation in the process and H′is the perturbing Hamiltonian. As for three phonon scattering, the initial and final states need to be specified as well as the perturbing Hamiltonian to evaluate the transition rate. In the inelastic interaction, an electron emits a phonon as it transitions to a lower energy state or an electron absorbs a phonon to reach a higher energy state. This interaction is schematically illustrated with Fig. 23 below [87].

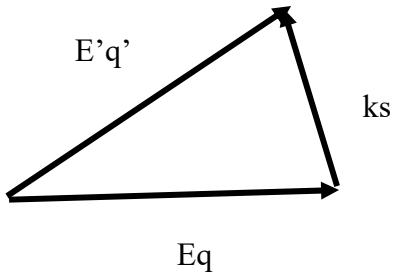

Fig. 23. Electron phonon interaction illustration. The vectors label E'q' and Eq represent different electron states and the vector labeled ks represents a phonon. Reproduced from [87].

In the case where a phonon is emitted, the initial state consists of an electron of energy E' and momentum q' (where q' is q + k), an electron of energy E and momentum q, and a phonon of momentum k and polarization s. The final state consists of the occupation number of electrons with energy E' and momentum q' ($f_{E(q+k)}$) decreasing by a value of one, the occupation number of electrons with energy E and momentum q ($f_{E(q)}$) increasing by one, and the occupation number of phonons with momentum k and polarization s (n_{ks}) increased by a value of one. Thus, the initial and final states are denoted with the following nomenclature.

$$|\psi_n\rangle = \left|f_{E(q+k)}, f_{E(q)}, n_{ks}\right\rangle \tag{81}$$

$$\langle\psi_m| = \left\langle n_{ks}+1, f_{E(q+k)}-1, f_{E(q)}+1\right| \tag{82}$$

The perturbing Hamiltonian (H′) is taken to be the coupled electron-phonon Hamiltonian expressed to first order atomic displacements. In the notation of Giustino [88] it is shown with equation 83,

$$H' = N_P^{-1/2} \sum_{\substack{k,q \\ mns}} g_{mns}(q,k)\hat{c}^{\dagger}_{mq+k}\hat{c}_{nq}(\hat{a}_{ks} + \hat{a}^{\dagger}_{-ks}) \ , \tag{83}$$

where $N_P^{-1/2}$ is the number of unit cells in the crystal, $g_{mns}(q,k)$ is the matrix element of the electron-phonon interaction (it is an indication of the strength of the interaction between electrons in bands n and m (with wavevectors q and q + k respectively) and a phonon with wavevector k and polarization s), and $\hat{c}$ and $\hat{a}$ are the respective electron and phonon creation/annihilation operators. The matrix element can be expressed as follows [52, 88, 89].

$$g_{mns}(q,k) = \left(\frac{\hbar}{2M\omega_{ks}}\right)^{1/2} \langle mq+k|\partial_{ks}V|nq\rangle \tag{84}$$

M is the atomic mass, ω_{ks} is the frequency of the phonon with wavevector k and polarization s, and $\partial_{ks}V$ is the variation in the electron potential produced by the deformed lattice due to the presence of the phonon. In the deformation potential approach [89], the term $\langle mq+k|\partial_{ks}V|nq\rangle$ is replace by two different expression depending on the polarization of the phonon that is present. The two expressions are shown below with equations 85 and 86 for acoustic and optical phonon respectively.

$$\langle mq+k|\partial_{ks}V|nq\rangle = D_A k \tag{85}$$

$$\langle mq+k|\partial_{ks}V|nq\rangle = D_0 \tag{86}$$

D_A is the deformation potential associated with acoustic phonons and D_0 is the deformation potential associated with optical phonons. The expressions are different for the phonon polarizations because of the different manner in which these two types of phonons distort the crystal lattice. Making these substitutions into Fermi's Golden Rule for the case where an acoustic phonon is emitted results in equation 87.

$$\dot{P}_{n-m} \cong \frac{2\pi}{\hbar}\left|\langle n_{ks}+1, f_{E(q+k)}-1, f_{E(q)}+1|N_P^{-1/2}\sum_{\substack{k,q\\mns}}\left(\frac{\hbar}{2M\omega_{ks}}\right)^{1/2} D_A k\ \hat{c}^{\dagger}_{mq+k}\hat{c}_{nq}(\hat{a}_{ks}+\hat{a}^{\dagger}_{-ks})\,|f_{E(q+k)}, f_{E(q)}, n_{ks}\rangle\right|^2 \delta(E_n-E_m), \tag{87}$$

Simplification results in equation 88.

$$\dot{P}_{n-m} \cong \frac{2\pi}{\hbar}\left(\frac{\hbar}{2N_P M\omega_{ks}}\right) D_A{}^2 k^2\ \left|\langle n_{ks}+1, f_{E(q+k)}-1, f_{E(q)}+1|\sum_{\substack{k,q\\mns}}\hat{c}^{\dagger}_{mq+k}\hat{c}_{nq}(\hat{a}_{ks}+\hat{a}^{\dagger}_{-ks})\,|f_{E(q+k)}, f_{E(q)}, n_{ks}\rangle\right|^2 \delta(E_n-E_m), \tag{88}$$

The only terms that survive the inner product with the annihilation and creation operators are the ones that lead to the initial state being identical to the final state. This results in equation 89.

$$\dot{P}_{n-m} \cong \frac{2\pi}{\hbar}\left(\frac{\hbar}{2N_P M\omega_{ks}}\right) D_A{}^2 k_s{}^2\ f_{E(q)}(1-f_{E(q-k)})(n_{ks}+1)\delta(E_n-E_m) \tag{89}$$

The case where an acoustic phonon is absorbed is shown with equation 90.

$$\dot{P}_{n-m} \cong \frac{2\pi}{\hbar}\left(\frac{\hbar}{2N_P M\omega_{ks}}\right) D_A{}^2 k_s{}^2\ f_{E(q)}(1-f_{E(q+k)})n_{ks}\delta(E_n-E_m) \tag{90}$$

Similar equations can be written for the cases involving emission or absorption of optical phonons and are shown with equations 91 and 92.

$$\dot{P}_{n-m} \cong \frac{2\pi}{\hbar}\left(\frac{\hbar}{2N_P M\omega_{ks}}\right) D_0^2\ f_{E(q)}(1-f_{E(q-k)})(n_{ks}+1)\delta(E_n-E_m) \tag{91}$$

$$\dot{P}_{n-m} \cong \frac{2\pi}{\hbar}\left(\frac{\hbar}{2N_P M\omega_{ks}}\right) D_0^2\ f_{E(q)}(1-f_{E(q+k)})n_{ks}\delta(E_n-E_m) \tag{92}$$

Thus, equations 89-92 represent the electron-phonon scattering rates as determined from Fermi's Golden Rule using the deformation potential approximation.

4.6 Heat Generation Implementation

Fully accounting for electron-phonon scattering using the scattering rate equations of 89-92, in a manner consistent with the prior development of the SPTM, would involve significant model development. This would be initiated with development of an electron transport model that is on par with the phonon transport model. This would involve implementation of an electron dispersion model or band model. In a manner similar to Pop et al. [90] a relatively simple analytic conduction band model could be implemented. Determination of the available electron-phonon scattering partners that conserve energy and momentum would involve an interaction search across the wavevector space. And, prediction of the net number of phonons of a given mode generated (or destroyed) in each time step would be determined by applying the scattering rates of equations 89-92 to each of the scattering partner interactions. This is currently beyond the scope of this dissertation and is deferred to a future work. Thus, a simplified approach to account for heat generation due to this interaction is implemented. The model is broken into two relative effects. First, the heat generation rate in the geometric space is considered and second, the distribution of the heat generation to the respective phonon modes. Combined, these models

would account for the important physical features of the electron-phonon interaction and would be able to reproduce a physically appropriate phonon generation rate.

As the electron-phonon scattering rate is not computed directly in the current implementation of the model, the volumetric heat generation rate is treated as a geometric cell input parameter. At each time step, the energy input to each cell is computed as the product of the heat generation rate, the cell volume, and the time step as is shown in equation 93.

$$E_{in} = \dot{Q}'''\Delta x\dot{\Delta} y\Delta z\Delta t \tag{93}$$

The volumetric heat generation rate is expressed as $\dot{Q}'''$, the cell dimension in the Cartesian coordinate directions are shown as $\Delta x\Delta y\Delta z$ and the time step is expressed as Δt . The cellular energy input results in in a net production of phonons but not all phonon modes produce phonons at the same rate. The rate that phonons of given characteristics are produced as a result of heat generation from the electron phonon interaction depends on the phonon wavevector, frequency, and polarization as well as the electron-phonon energy and momentum selection rules. As a result, the number of phonons generated in a given computational domain and timestep is computed directly from these factors. This is done in a multi-step process. First, a parameter that is directly proportional to the electron-phonon scattering rate from Fermi's Golden Rule, is computed for all of the phonon pseudostates referenced in section 4.2. This is referred to as the electron-phonon scattering strength and is computed within the deformation potential approach using the following equations for acoustic and optical phonons respectively.

$$EPH_{St} = {D_A}^2 k_s^2 \tag{94}$$

$$EPH_{St} = {D_0}^2 \tag{95}$$

The values used for the deformation potential constant D_A were 3.01 eV for transverse acoustic modes and 6.39 eV for longitudinal acoustic modes. The value used for D_0 was 6.0E8 eV/cm [73].

Secondly, the relative strengths are then multiplied by a measure of the electron-phonon interaction density in the phase space. The electron phonon interaction density was estimated using a 1-d approach. The phonon characteristics are estimated using fits to the dispersion relations in the (100) direction. The electron dispersion was estimated using the parabolic conduction band model of Rowlette and Goodson [73]. The respective electron and phonon energy as a function of wavevector computed by the SPTM are illustrated with Fig. 24 overlaid with the conduction band model.

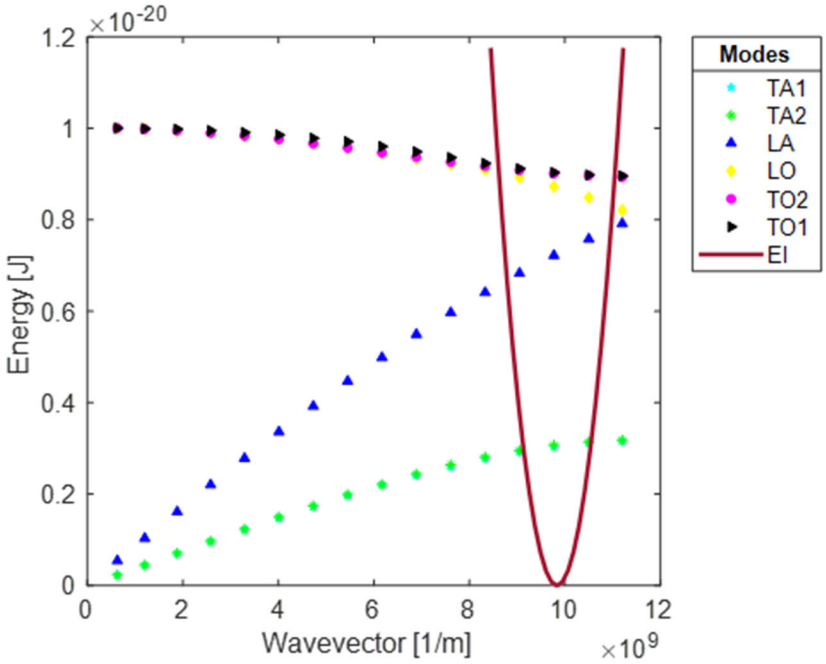

Fig. 24. Phonon and electron dispersion relations (Energy vs. wavevector) utilized in the calculation of phonon source to mimic Joule heating. Electron energies (El) calculated from [73].

For a given discretization of the wavevector space, the possible partners available for the electron phonon interaction are computed based on satisfying momentum conservation. In one dimension this is illustrated below.

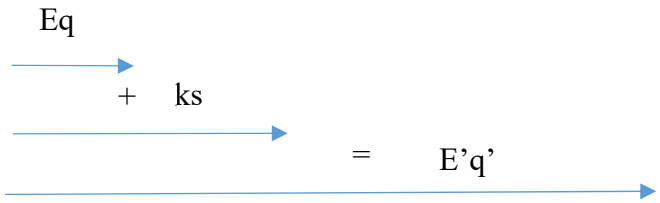

Fig. 25. Illustration of the combination of wavevectors satisfying momentum conservation associated with an electron (Eq) and a phonon (ks) to produce a different electron state (E'q') in 1-d.

The wavevector associated with one volume element is added to the wavevectors associated with all of the other volume elements. If this results in a value greater than the end of the FBZ, then a reciprocal lattice vector is subtracted from the results. The possible interactions that satisfy momentum conservation are then checked to see if energy conservation is possible. This results in a check to see if an initial phonon energy added to an electron energy will be equal to a phonon energy within a certain tolerance. If the interaction passes the energy conservation check then it is written to a file. The results of the file are compiled to determine the number of respective interactions in the (100) direction as a function of the resulting phonon energy. Graphically, the interaction density is illustrated with Fig. 26.

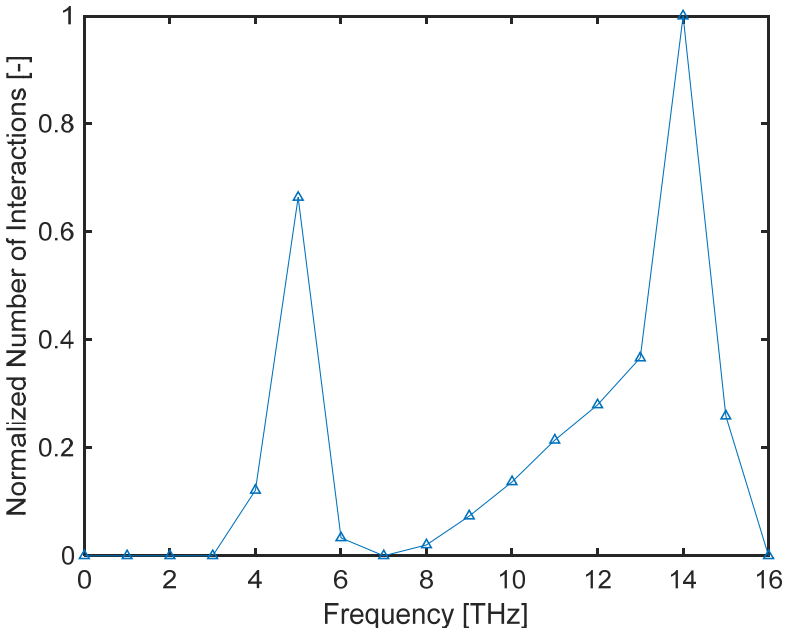

Fig. 26. Normalized interaction density for electron phonon scattering calculations as a function of phonon frequency computed from a 1-d interaction search.

Fig. 26 illustrates the interaction density ($\mathrm{EPH_{Int}}$) (relative number of electron-phonon scattering partners) as a function of phonon frequency. The first peak corresponds to locations where the electron energy is similar to the phonon energy. In areas where there is significant difference between the phonon and electron energies there are gaps as the selection rule precludes an interaction from occurring. If an interaction can occur, the number of phonons created for a given mode is computed as a multiplication of this relative interaction density against the strength parameter described previously.

The product of the electron phonon scattering strength and the electron phonon interaction density gives a value proportional to the number of phonons created from heat generation.

$$N_{gen} \sim EPH_{St} \cdot EPH_{Int} \tag{96}$$

To determine the actual number of phonons generated in a given cell and time step a normalization procedure is employed. This normalization procedure ensures that energy conservation is enforced while the modal dependent phonon generation profile is preserved. The normalization constant is computed as follows.

$$EPH_{Norm} = \frac{E_{in}}{\sum_{i=1}^{N_{pseudo}} \hbar\omega_i EPH_{St} \cdot EPH_{Int}} \tag{97}$$

The summation is performed over all of the phonon pseudostates. The number of phonons generated in a given cell in a given timestep for each pseudostate is then computed as the following.

$$N_{gen} = EPH_{St} \cdot EPH_{Int} \cdot EPH_{Norm} \tag{98}$$

It should be noted that the implementation of this model is meant to mimic Joule heating as a result of electron-phonon interactions. However, since the heating rate is treated as an input parameter, some effects are not accounted for. These include the increase in the heating rate that

could occur because of the increase in the non-equilibrium populations of phonons as well as the increase in the intrinsic carrier concentration as a result of increased lattice effective temperature. It is possible that these two effect could lead to a feedback loop between the local conditions and the overall heating rate leading to an excursion event. This feedback phenomenon is deferred to future work. Results of the heat generation implementation are illustrated in section 5.3.

4.7 Drift Theory

Drift is the unimpeded movement of phonon wavepackets though the crystal lattice between scattering events. Phonon wavepackets translate through the lattice at a velocity corresponding to the group velocity that depends directly on the dispersion relations and therefore the nature of the crystal structure [52]. This is illustrated with equation 9. Variation of the group velocity occurs within a given phonon mode as the wavevector and frequency change. In addition, there is variation from mode to mode with the highest group velocities occurring for the acoustic polarizations near the FBZ center. Drift of phonons from one geometric location to another in the domain of interest will impact the effective temperatures at any location within the domain and the number of phonons in any geometric cell that are available to participate in scattering events.

4.8 Drift Implementation

Calculation of drift from one cell in the geometric domain to its neighbors with the SPTM begins with computation of the group velocity of the phonon pseudostates. This is done using a finite difference formulation to approximate the derivative of equation 9. The frequencies of a given pseudostate are calculated at the boundaries of the volume element surrounding the centroid in the wavevector space [9]. These values are then used with the dimensions of the volume element to estimate the group velocity in a given direction. The pseudostate velocities are shown with Fig. 27 below.

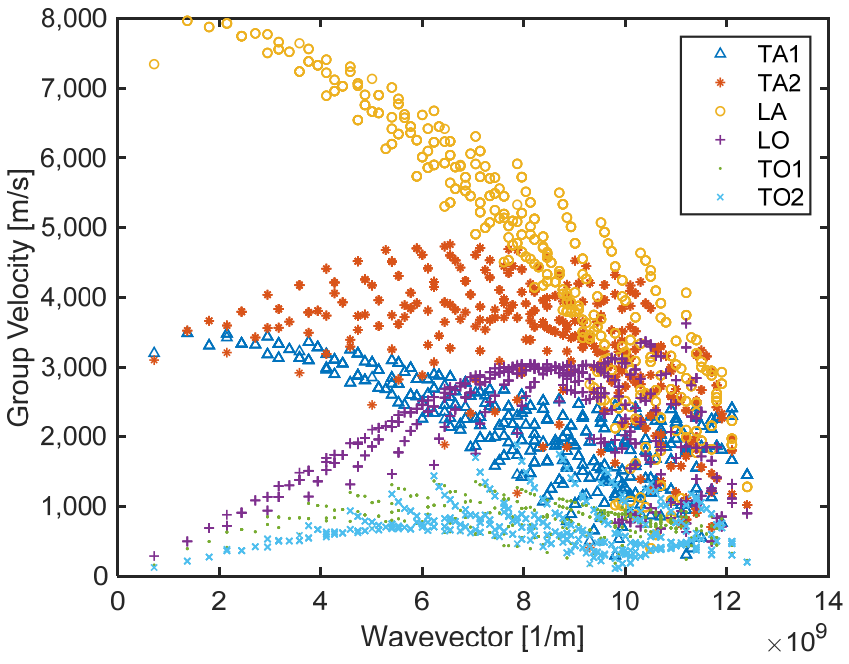

Fig. 27. Phonon pseudostate group velocities for the six phonon modes or polarizations across the wavevector space shown as a function of wavevector magnitude.

With the pseudostate group velocities determined, cellular drift is computed in the following manner. The methodology utilized is similar for both 1-d and 3-d cases. It begins with the assumption that the phonons of a given pseudostate are uniformly distributed across the geometric cell of interest. Subject to their group velocity, these phonons will travel a certain distance in the computational timestep. This will lead to the probability that a given number of phonons will have traversed to adjacent cells depending on their location within the current cell. This probability is computed based off of the ratio of shifting geometric properties, like area or volume, which would be directly related to the number of phonons. This is illustrated in two dimensions with Fig. 28.

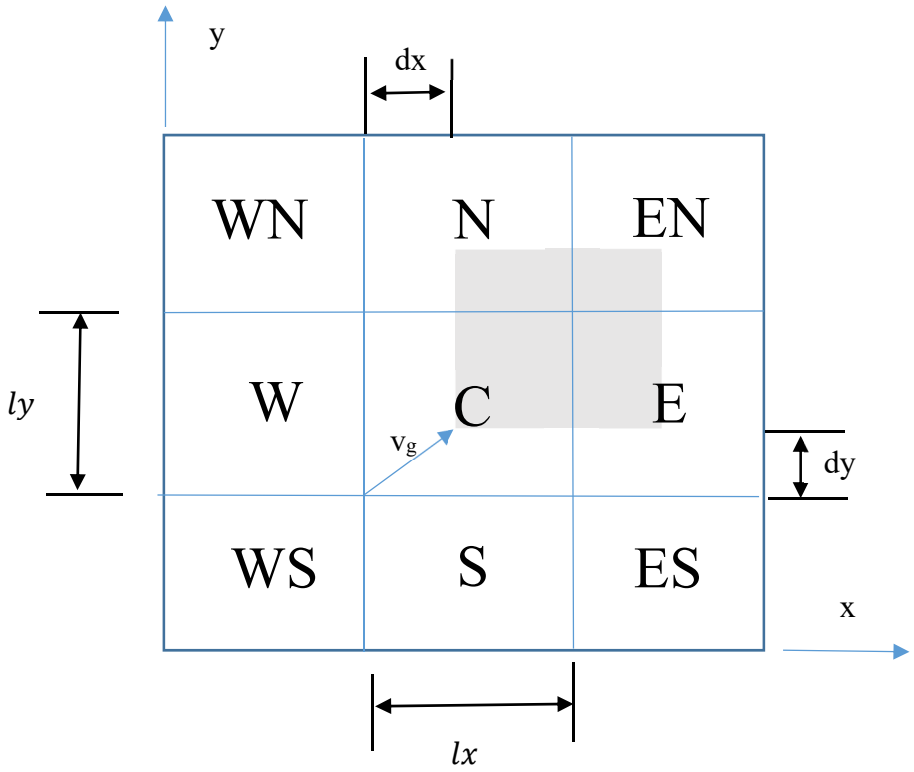

Fig. 28. Illustration of pseudostate drift in two dimensions. Nine geometric cells are shown in an x-y plane and labeled according to their geographic location relative to the center cell. The gray shading shows the displaced distribution of phonon associated with a pseudostate undergoing drift with a group velocity with positive components. Adapted from [9].

Nine geometric cells are shown. For illustration, drift is considered from the Center (C) cell to the surrounding cells with a particular pseudostate group velocity in the positive x, and y. The probability that the phonons associated with that pseudostate will remain in the current cell is computed by the ratio of the shaded area remaining in the cell to the total area of the cell. This is shown as follows,

$$P_C = \frac{(l_x - dx)(l_y - dy)}{l_x l_y} \quad , \tag{99}$$

where l_x and l_y are the x and y dimensions of the geometric cell, dx and dy are the distances the phonons from the given pseudostate are displaced in geometric space for the given timestep. These displaced distances are computed as the product of the x and y components of the group velocity and the timestep as follows.

$$dx = v_{gx} \cdot \Delta t \quad (100)$$

$$dy = v_{gy} \cdot \Delta t \quad (101)$$

v_{gx} and v_{gy} are the components of the group velocity (v_g) in the x and y directions respectively and Δt is the timestep. Drift of phonons to the Eastern (E) cell in the positive x direction is given with the following equation.

$$P_E = \frac{dx(l_y - dy)}{l_x l_y} \quad (102)$$

Drift to the Northern (N) cell in the positive y direction is given with the following equation.

$$P_N = \frac{dy(l_x - dx)}{l_x l_y} \quad (103)$$

Drift to the East-North (EN) cell in the positive x and y directions is given with the following equation.

$$P_{EN} = \frac{dxdy}{l_x l_y} \quad (104)$$

Drift to the other cells is computed in exactly the same way for all of the pseudostate group velocities. Depending on the velocity, drift could be to the West-North (WN), West (W), South (S), East-South (ES), or West-South (WS) as well.

The drift computation in the 3-d case is performed in a manner analogous to the two dimensional case. However, in three dimensions, drift can occur to twenty-six neighboring cells.

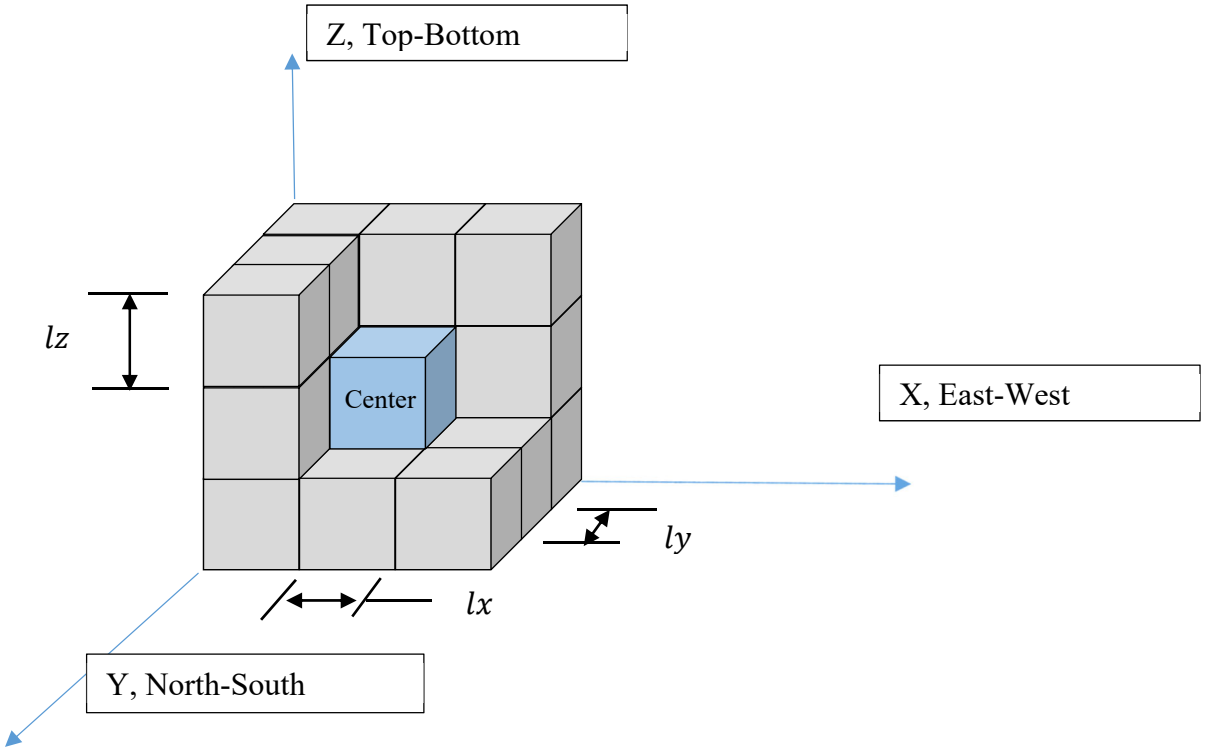

Fig. 29. Direction nomenclature and the twenty-seven relevant geometric cells for 3-d Drift.

The cells are referenced in the x, y, and z directions according to the East-West, North-South, and Top-Bottom designations. The twenty-seven cells in the 3 by 3 array are shown in Fig 29.

The Center cell is colored with blue. Some of the cells are removed to show the center cell. As in the two dimensional case, all of the phonons of a given pseudostate are initially assumed to be evenly distributed within the volume of the center cell. The probability calculations for drift in the different possible directions will be illustrated with the equations below. First, the displacement of the volume that represents the distribution of phonons in the center cell is calculated in the x, y, and z directions.

$$dx = |v_{gx}|\Delta t \quad (105)$$

$$dy = |v_{gy}|\Delta t \quad (106)$$

$$\mathrm{dz} = |v_{gz}|\Delta t \quad (107)$$

The amount of the volume that remains in the center cell is computed as the following.

$$rdx = lx - dx \quad (108)$$

$$rdy = ly - dy \quad (109)$$

$$rdz = lz - dy \quad (110)$$

The volume of the cell is computed as the following.

$$CellVolume = lxlylz \quad (111)$$

The probability of movement of phonons to adjacent cells is computed as the ratio of displaced or remaining volume to the original cell volume as follows.

$$P_c = \frac{rdx*rdy*rdz}{CellVolume} \quad (112)$$

$$P_x = \frac{dx*rdy*rdz}{CellVolume} \quad (113)$$

$$P_y = \frac{dy*rdx*rdz}{CellVolume} \quad (114)$$

$$P_z = \frac{dz*rdx*rdy}{CellVolume} \quad (115)$$

$$P_{xy} = \frac{dx*dy*rdz}{CellVolume} \quad (116)$$

$$P_{xz} = \frac{dx*rdy*dz}{CellVolume} \quad (117)$$

$$P_{yz} = \frac{rdx*dy*dz}{CellVolume} \quad (118)$$

$$P_{xyz} = \frac{dx*dy*dz}{CellVolume} \quad (119)$$

P_c is the probability of phonons in a given pseudostate remaining in the center cell, P_x is the probability of phonons moving in the x direction, P_y is the probability of phonons moving in the y direction, P_z is the probability of phonons moving in the z direction, P_{xy} is the probability of phonons moving in the x and y direction, P_{xz} is the probability of phonons moving in the x and z direction, P_{yz} is the probability of phonons moving in the y and z direction, and P_{xyz} is the probability of phonons moving in the x and y and z direction. The probabilities are normalized to minimize round off error.

The number of phonons that are transferred to adjacent cells are calculated based off of the individual pseudostate characteristics of population and group velocity direction. Consider drift of a pseudostate with a group velocity in both the positive x, y, and z direction. With this scenario, some phonons will remain in the Center (C) cell after the given timestep and others will drift to the East (E), North (N), Top (T), East-North (EN), East-Top (ET), North-Top (NT), and East-North-Top (ENT). The numbers are computed as follows.

$$N_c = N_{ps}P_c \quad (120)$$

$$N_E = N_{ps}P_x \quad (121)$$

$$N_N = N_{ps}P_y \quad (122)$$

$$N_T = N_{ps}P_z \quad (123)$$

$$N_{EN} = N_{ps}P_{xy} \quad (124)$$
$$N_{ET} = N_{ps}P_{xz} \quad (125)$$
$$N_{NT} = N_{ps}P_{yz} \quad (126)$$
$$N_{ENT} = N_{ps}P_{xyz} \quad (127)$$

Boundary conditions for drift calculations include a specified cell temperature, periodic boundary, pure specular boundaries, and partially reflective boundaries. Purely diffusive boundary conditions are not implemented at this time. Any cell in the domain can be specified as a constant temperature cell. This implies that after drift calculations are performed, the phonon distribution within the specified cell are set back to the local thermodynamic equilibrium values based off of the Bose Einstein distribution for the specified temperature. The Bose Einstein distribution is illustrated with equation 8.

Periodic boundary conditions can be implemented in the 1-d simulations. This implies that phonons transported out of the geometric cell in the y and z directions return back to the geometric cell but in the opposite side of the cell. This can be illustrated in the following Figure.

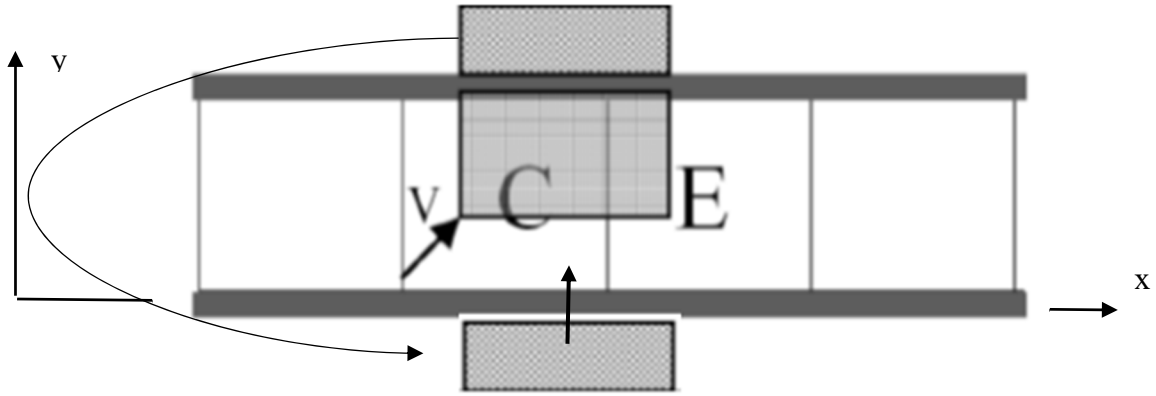

Fig. 30. Illustration of periodic boundary conditions for drift calculations. As in Fig. 28, the shaded area represents the displaced distribution of phonons from a pseudostate with group velocity V. Adapted from [9].

Fig. 30 illustrates drift of a pseudostate with a group velocity in the positive x and y directions. With this group velocity, phonons will drift from the Center cell to the East, North, and Northeast cells. With the periodic boundary condition, the phonons that drift to the North and Northeast cells are returned to the computational domain to the Center and East cells respectively.

In addition to the periodic boundary condition, 1-d calculations can employ specular boundaries. Specular implies a pure reflection back into the geometric domain and would be indicative of perfect insulation surrounding the domain. Fig. 31 is used to illustrate this condition.

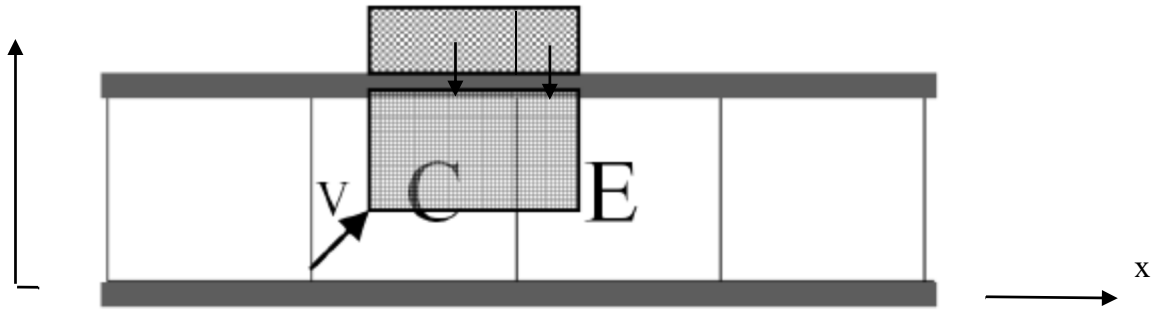

Fig. 31. Illustration of specular boundary conditions for drift calculation. As in Fig. 28, the shaded area represents the displaced distribution of phonons from a pseudostate with group velocity V. Adapted from [9].

As was the case with Fig. 30, consider drift of a pseudostate with a group velocity in the positive x and y directions. With this group velocity, phonons of this pseudostate would be expected to drift from the Center cell to the East, North, and East-North cells. However, when top and bottom boundaries are considered to be purely specular, the phonons that would have drifted to the North and East-North cells are reflected back in to the computational domain. Those that would have transported to the North cell are reflected back to Center cell. Those that would have been transported to the East-North cell are reflected back into the domain but to the East cell. In either case, the sign of the component of the wavevector and thus velocity in the direction perpendicular to the respective boundary is flipped. With certain pseudostate velocities like the one illustrated above, it is possible that some of the phonons that would have transported to the North cell and are reflected back into the Center cell should actually be transported to the East cell due to multiple reflections. This is currently not implemented in the SPTM but its effect is considered to be very small given the limitations imposed on the computational timestep for a given geometric cell size.

With the purely specular boundary conditions, all of the phonons incident on a given boundary are reflected back into the computational domain. The SPTM has the option to reflect less than 100% of the phonons back into the domain. This would be indicative of some level of conduction heat transfer to the surrounding material. As phonons are "lost" from the computational domain, this would demonstrate energy transport out of the geometric region of interest.

2-d and 3-d specular boundaries are implemented in a manner consistent with the 1-d illustration. Results of the implementation of drift are illustrated in section 5.4.

4.9 Device Modeling

The model improvements documented in this dissertation are aimed at enhancing the capability of the SPTM to model nanoscale electronic devices involving heat generation as a result of electron-phonon scattering. Two methods were used to demonstrate this capability. The first is a method of comparisons to prior published works. The direct comparison of the SPTM to these works will demonstrate the combined accuracy, flexibility, and efficiency of the method. Second, the SPTM is applied to simulations of current and proposed transistor geometries to demonstrate that valuable thermal design information can be obtained for these devices. This

involves providing information that may not be attainable from experimental means and enhancing understanding of physical behavior of devices and systems.

4.9.1 Comparison to Prior Published Works

The SPTM was applied to model devices similar to those presented in current state of the art nanoscale thermal simulations with heat generation as a result of electron-phonon scattering. This direct comparison is assessed against certain metrics to demonstrating the accuracy, flexibility, and efficiency of the SPTM against works that span the range of modeling approaches. The metrics and the score for each metric is illustrated in Table 6.

Table 6. Metrics and score used for comparison of SPTM to other models

Score	Thermal Model	Electrical Model	Interaction	Geometric Flexibility	Temporal Flexibility	Feasibility as Design Tool
1	Classical Fourier Diffusion	Classical Maxwell Wave	Classical heat source	Only geometry specified	Only Steady State	Not feasible for real devices
2	Numerical BTE	Numerical BTE	Analytical phonon source	Any 1D	Only Transient	Simple devices on Supercomputer
3	Monte Carlo	Monte Carlo	Random phonon source	Any 2D	Both Steady State and Transient	Realistic devices on Supercomputer
4	Full Phonon Fidelity	Full Electron Fidelity	Phonon source to mimic electron-phonon scattering	Any 3D	Transient Switching	Realistic devices on workstation
5	Direct Atomic Simulation	Direct Quantum Transport	Scattering rates for Fermi's	All	Any transient	Realistic devices on PC

The defined rubric was chosen to represent the important characteristics that would be needed by an accurate, flexible, and efficient transistor design tool. The first two categories relate to the fidelity of the two major physical phenomena that require representation for transistor modeling. The third one relates to the interaction between thermal and electrical transport. The fourth is for geometric flexibility, the fifth for temporal flexibility, and the last for feasibility which really relates to computational efficiency. Within each category a higher score indicates either a higher fidelity modeling approach or higher flexibility. The device models of prior works chosen for comparison are summarized in the paragraphs to follow.

4.9.1.1 Case 1: DAS - Rhyner and Luisier Simulations

Rhyner et al [41-43] performed simulations of nanowire transistors using a Non-Equilibrium Greens Function (NEGF) [91] quantum formulation for both phonon and electron transport. This is a fundamental atomistic quantum treatment for the transport and interactions of both electrons and phonons. The quantum vibrational state of the atoms and quantum state of the transport electrons are computed at each lattice site and can change due to scattering interactions. The simulations were performed on a domain illustrated with Fig. 32.

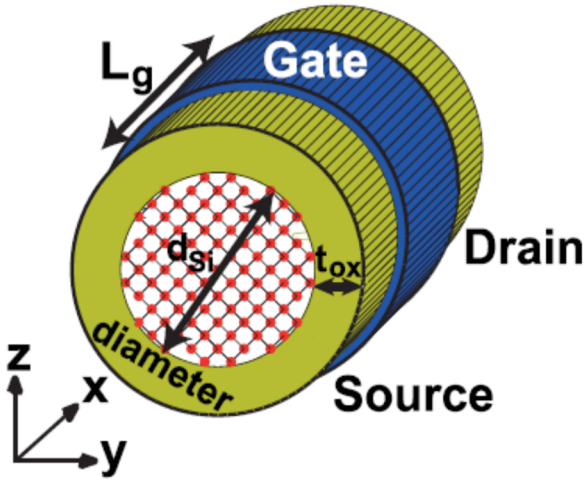

Fig. 32. Schematic illustration of the nanowire transistor simulated by Rhyner et al [41].

The silicon domain was composed of approximately 15,000 atoms. The diameter was 3 nm with a total length of 45 nm. Source, drain, and gate regions had a length of 15 nm each. The simulations demonstrated effective temperature distributions as a function of both length and total power dissipation rate. In addition, the effect of self-heating on current reduction was reported.

The SPTM was applied using a 1-d model to similar conditions as the Rhyner model described above. As the SPTM is currently only able to use rectilinear coordinates, y and z dimensions were chosen as 2.66 nm to produce the same effective cross section area as a 3 nm diameter. The total effective length was 45 nm with source, channel, and drain regions each consisting of 15 nm. The geometry is illustrated in the following Fig. 33.

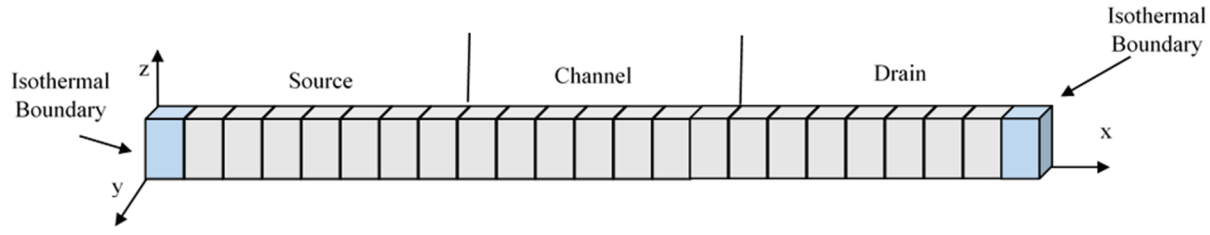

Fig. 33. Schematic illustration of the nanowire transistor simulated with the SPTM to compare to Rhyner et al [41].

The total number of cells in the x direction was 32 with a dimension of 1.5 nm. The first and last cell are set to an isothermal boundary condition of 300 K. The heating profile used was exponential in nature, peaked at the end of the channel and extends into the drain region. The profile is similar to the one documented in section 4.9.1.4 to follow with Fig. 41. The heating

profile was scaled to produce the same heat dissipation rates documented by Rhyner. Results of the comparison are illustrated in Section 5.5.1.1.

4.9.1.2 Case 2: 1D Monte Carlo - Rowlette and Goodson Simulations

Goodson, Pop, Sinha, and Rowlette have done much work in the area of coupled thermal/electrical transport in nanoscale Field Effect Transistors (FET's). The work chosen for comparison to the SPTM predictions is that of Rowlette and Goodson [73]. With this work, a 1D simulation of a silicon n+/n/n+ device (also known as a PNP junction) was used to represent the core of transistor structures. The device consists of 150 nm source (S or n+) and drain (D or n+) regions separated by a channel (Channel or n) of 20 nm. The channel is below the gate region (G) and heat generation is peaked near the channel/drain interface. Schematically these are illustrated with Fig. 34.

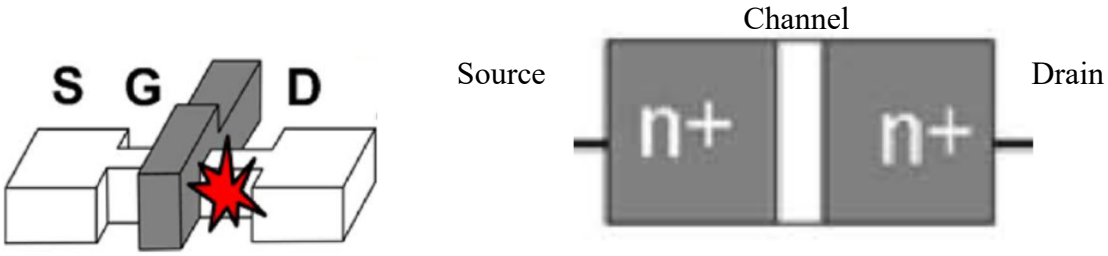

Fig. 34. Schematic illustration of the 1-d domain simulated by Rowlette and Goodson [73].

Electron transport was simulated with a Monte-Carlo technique. Phonon transport was simulated through the solution of a split-flux form of the phonon Boltzmann Transport Equation. The simulations are coupled through electron-phonon scattering which results in addition or removal of phonons with given characteristics within the domain. Key results of these simulations include current density, electric field, power dissipation, and effective temperature as a function of position. In addition, predictions on the magnitude of the deviation of the phonon population (and particularly optical phonons) from equilibrium at certain locations are provided.
The SPTM was applied to a similar 1D domain as was used for the Rhyner comparison. The total length was 340 nm consisting of 34 cells. The geometric domain is illustrated in Fig. 35.

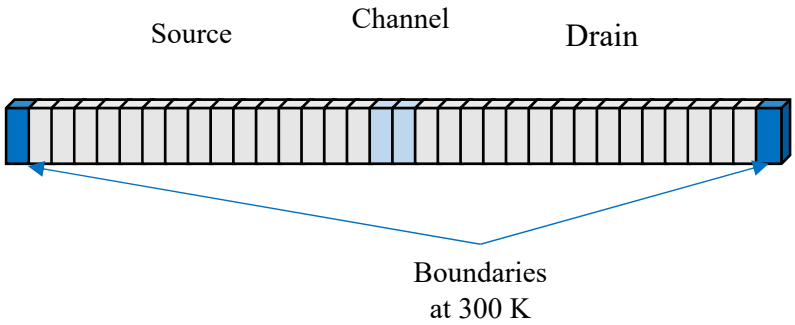

Fig. 35. Schematic illustration of the nanowire transistor simulated with the SPTM to compare to Rowlette and Goodson [73].

The maximum heating profile detailed in [73] was used as an input to the SPTM and temperature boundary conditions of 300 K were applied in a manner consistent with the paper. Comparisons of key thermal conditions are made in Section 5.5.1.2.

4.9.1.3 Case 3: 3D Monte Carlo - Shomali Simulations

Shomali et al [92] performed simulations of thermal transport using the Monte Carlo method for solving the Boltzmann transport equation in two and three dimensions to represent silicon Metal Oxide Semiconductor (MOS) devices. The details of the computational method follow closely that of Mittal [93]. Heat generation was included to represent Joule heating using a phonon source. The 3-d structure simulated is illustrated with Fig. 36.

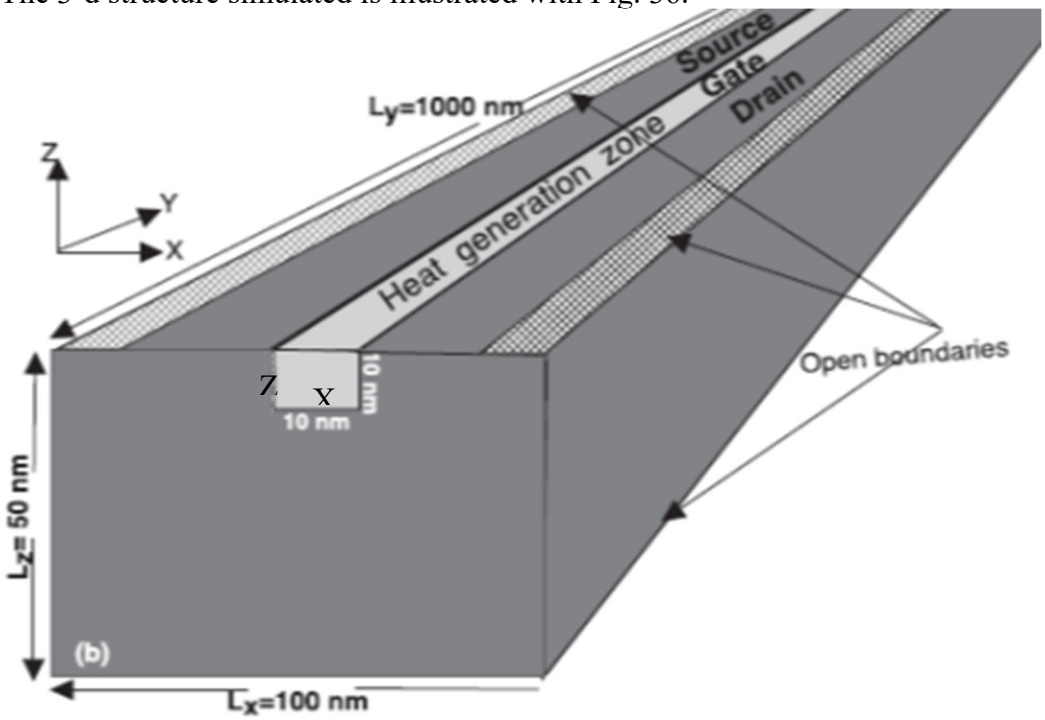

Fig. 36. Schematic illustration of the transistor domain simulated by Shomali et al [92].

Two cases were considered. The first (Case I) had an open bottom boundary, and the second (Case II) had both open bottom boundary and open boundaries at the source and drain contacts. Within the heat generation zone, a non-uniform heat generation rate was applied using the following equation,

$$\mathrm{Q} = Q_{max}(X + Z - 1) \quad , \tag{128}$$

where, X and Z are transformed coordinates within the local heat generation zone and Q_{max} is 1.0E13 W/cm^3.

The SPTM was applied to a similar domain in a 2-d manner. Both cases described above were modeled with 450 rectangular cells in the SPTM. This includes 30 cells in the x-direction of 3.33 nm and 15 cells in the z-direction of 3.33 nm. The geometric domain for the SPTM simulation is shown in Fig. 37 below.

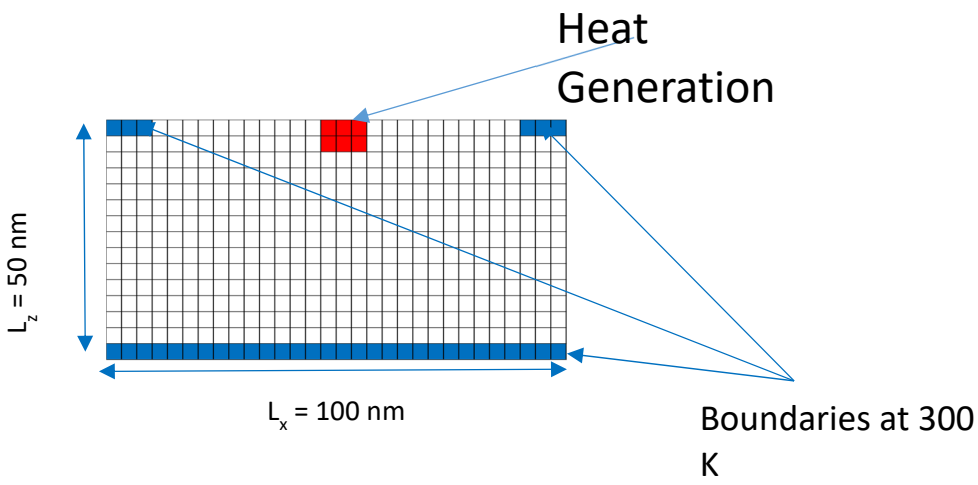

Fig. 37. Schematic illustration of the SPTM domain simulated to compare to Shomali et al [92].

Heat generation in the heat generation zone was modeling in a manner similar to equation 128 within the framework previously described for the heat generation algorithm in the SPTM. The results of the comparisons for the two cases are illustrated in Section 5.5.1.3.

4.9.1.4 Case 4: Fourier - Chhabria Simulations

Chhabria et al [94] performed thermal simulations on both FinFET and nanowire geometries with the goal of predicting temperatures and relating them to reliability concerns. Relative to the purposes of comparison to the SPTM, detailed simulations were performed using finite difference based methods to solve the Heat Conduction Equation to estimate the maximum effective lattice temperature rise on a gate level analysis. The detailed gate level analysis was performed on an array of either fins or nanowires. An example of the FinFET array geometry is schematically illustrated with Fig. 38.

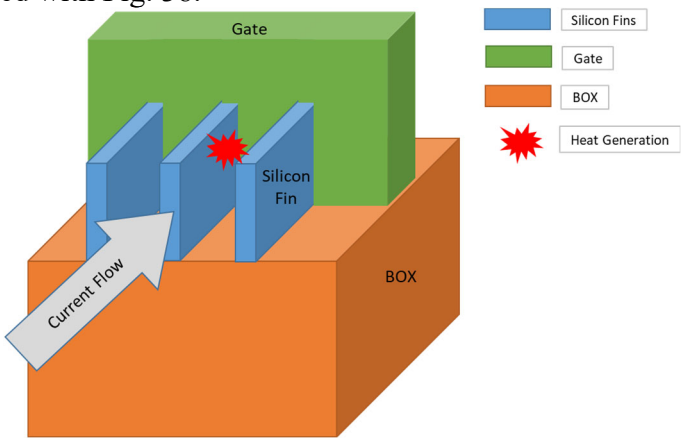

Fig. 38. Schematic illustration of a FinFET array [94].

Current flows from the source to the drain when the gate is energized. Energy is transferred from the current to the lattice resulting in heat generation. The heat generation profile used by Chhabria in the channel region is illustrated in Fig. 39.

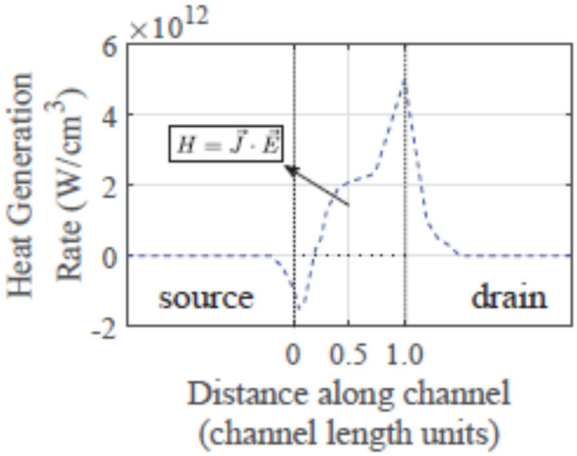

Fig. 39. Heat generation profile applied in the channel region used by Chhabria [94]. Profile is based off of that calculated by Pop [95].

The 7 nm Silicon-on-Insulator (SOI) FinFET node specifies fins to be 7 nm in width, 32 nm in height and approximately 50 nm in length with a 20 nm channel length. The fin pitch is 27 nm which illustrates the distance from fin to fin.

The SPTM was applied in a 2D manner to a geometric region surrounding one fin in the center of the array. The entire array was not simulated due to the assumption of thermal and geometric symmetry. The SPTM currently only has the capability to model phonon transport in silicon so the entire domain is silicon. The simulated geometry is illustrated in Fig. 40.

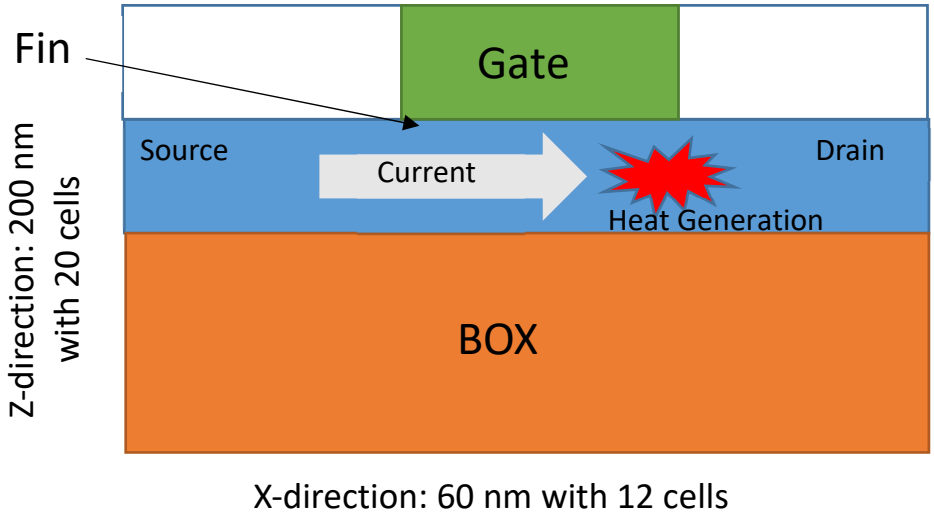

Fig. 40. Schematic illustration of the FinFET array simulated with the SPTM.

The geometric domain consists of 12 cells of 5 nm in the x-direction and 20 cells of 10 nm in the z-direction for a total of 240 computational cells. The bottom boundary (x-y plane at z = 0) is set to an isothermal condition at 300 K. The regions at the beginning and end of the fin (source and drain) are also set to isothermal at 300 K. Heat generation is implemented within the fin region. Rowlette et al. [73] have shown that a more realistic heat generation profile includes the peak

heat generation occurring at the end of the channel and extends significantly into the drain region. This is illustrated with Fig. 41.

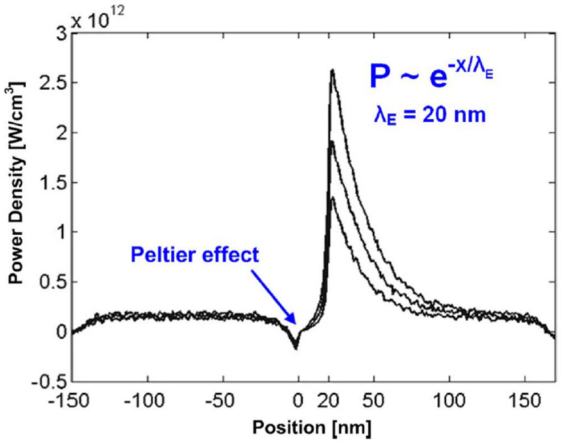

Fig. 41. More realistic heat generation profile from the source to the drain in a FinFET transistor. Reproduced from [16].

So, the heat generation profile implemented within the SPTM was different than the Chhabria simulation to reflect this fact. In addition, Chhabria scaled the heat generation profile to produce a net power dissipation of approximately 0.1 μW within the FinFET array. In reference to other works, this seemed to be a very low power dissipation thus, the SPTM implemented a higher peak dissipation rate on the order of 5.0E12 W/cm^3. This is more representative of the heat dissipated due to the current densities associated with these devices and the results are illustrated in Section 5.5.1.4.

4.9.2 Design Tool Demonstration

4.9.2.1 Silicon Nanowire Transistor

In addition to the comparison method described in the sections above, the SPTM was applied to current and emergent transistor geometries to demonstrate that design information can be obtained that includes valuable insight to local thermodynamic conditions. The IRDS predicts transitions to silicon nanowire array geometries in the near future. These geometries are illustrated in Fig. 4c and 4d. In addition, the nanowire is known as the ideal transistor due to the enhanced control provided by the gate all around geometry. Thus, this geometry was investigated for the initial design tool demonstration. The geometry of a simple nanowire transistor includes the source, channel, and drain regions. The current incarnation of the SPTM is only capable of modeling in rectilinear coordinates so, these regions are represented with labeled rectangles in Fig. 42.

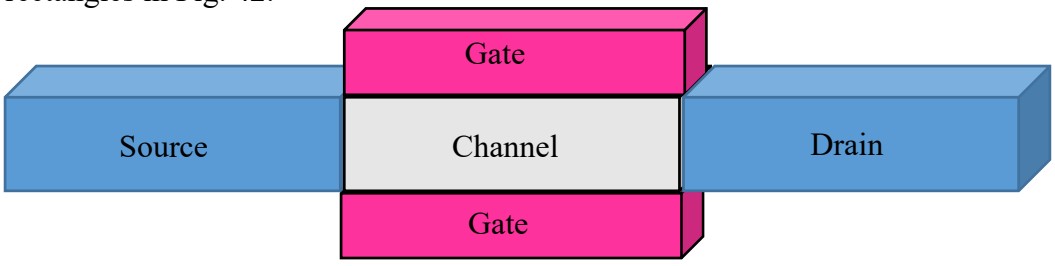

Fig. 42. 1-d geometric model of silicon nanowire transistor.

The geometric region is modeled in one dimension due to the symmetric nature of the device. The domain for the 1-d simulation is illustrated with the Fig. 43.

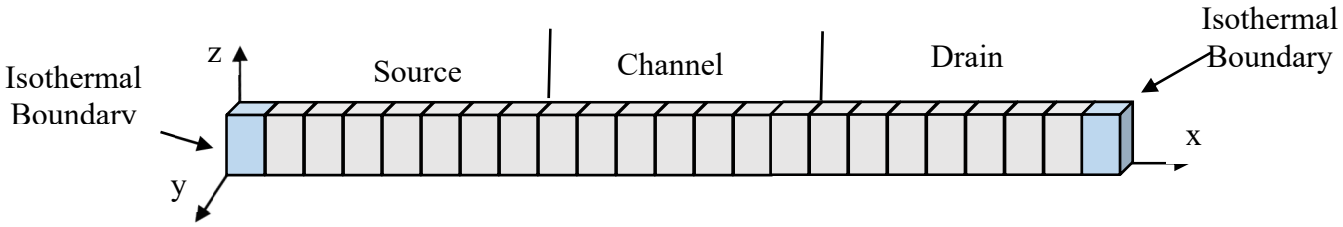

Fig. 43. 1-d geometric model of prototypic silicon nanowire transistor.

The geometric space is discretized into 23 cells in the x direction with an active length of 42 nm. The cells are each of 2 nm in the x direction and 6 nm in the y and z directions. The minimum cell dimension was chosen to ensure the validity of the quasi particle approach and provide fidelity in the geometric space. According to Hahn [15], the extent of the phonon wavepacket (or wavelength of the phonon wavepacket) is on the order of the lattice parameter for temperature above the Debye temperature. For silicon, this is on the order of 0.5 nm. The source, channel, and drain regions are each of approximately 14 nm in length.

The boundary conditions are purely specular at the Top, Bottom and North, South boundaries in the z and y direction respectively. Isothermal boundaries are imposed at the beginning of the source region and end of the drain region at the East and West boundaries in the x direction. Heat is generated in the transistor while current flows from the source to the drain due to electron-phonon interactions. The rate of heat generation depends on the bias voltage from the source to the drain, the gate to drain bias, the channel length, and the dopant. As the source to drain bias is increased and the channel length is decreased, the local electric field is increased and the electrons attain more kinetic energy. This results in increased heat generation as the scattering rates increase. The maximum heat generation rate is estimated from prior published results primarily from Monte Carlo analyses like those of Pop [96]. In addition, the functionality with respect to channel length was estimated from Rowlette and Goodson [73] as proportional to the channel length raised to the negative exponent of 1.7. The maximum heat generation rate expected as a function of the voltage bias and channel length ranging from 20 nm down to 5 nm with the source and drain regions doped at a rate of 1E20 $1/cm^3$ is shown with Fig. 44.

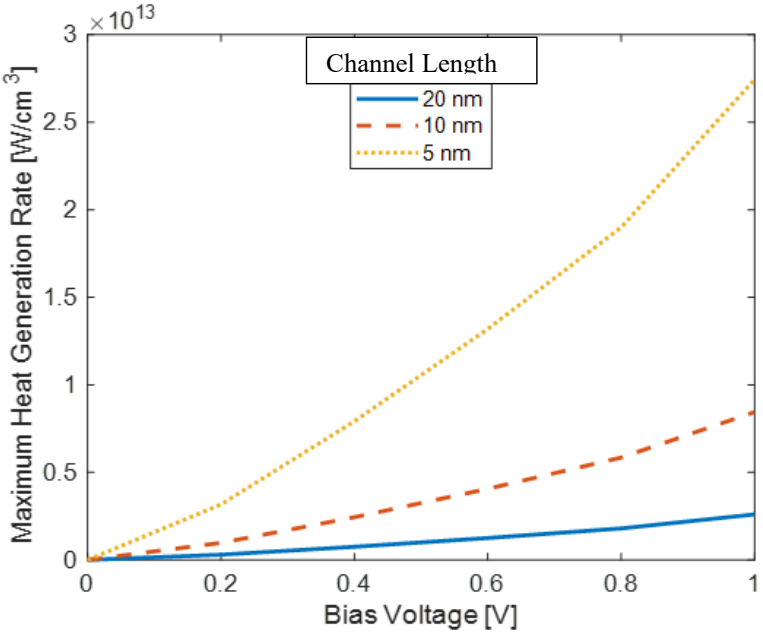

Fig. 44. Peak heat generation rate in a 1-d transistor as a function of bias voltage across the channel. Three channel lengths are illustrated from 20 nm down to 5 nm. Produced based on [73]and [96]. Dopant level in the source and drain is 1E20 1/cm^3.

In addition, the profile of heat generation from the source to the drain is not constant as was illustrated with Fig 41. The peak occurs near the end of the channel region and continues with significant heating in the drain region. The effect becomes more pronounced as the channel length becomes shorter. This is a result of the fact that electrons transport significant distances prior to scattering with the lattice [96]. The heat generation profiles of Fig. 41 are based on Monte Carlo analysis of electron and phonon transport. A similar simulation by Pop and Sinha [86] illustrates similar results relative to the profile and is shown with Fig. 45.

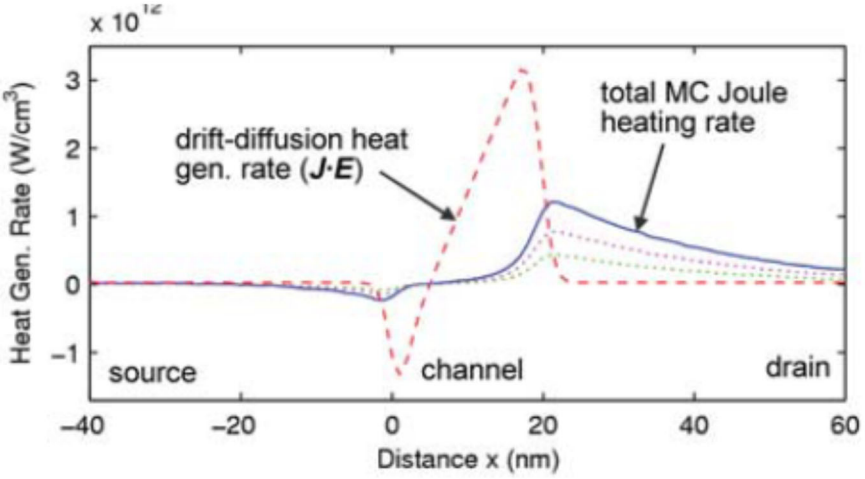

Fig. 45. Phonon-Electron scattering heat generation rates from source to drain in a transistor computed from Monte Carlo and compared to classical calculation referred to as drift diffusion. The small dotted lines indicate the heat generation due to optical phonons (upper) and acoustic phonons (lower). Reproduced from [86].

The heat generation rate as a result of Joule heating is treated as an input to the SPTM and is based on the results shown with Fig. 41 and 45. An example heat generation profile used with the 1-d nanowire simulations is shown with Fig. 46.

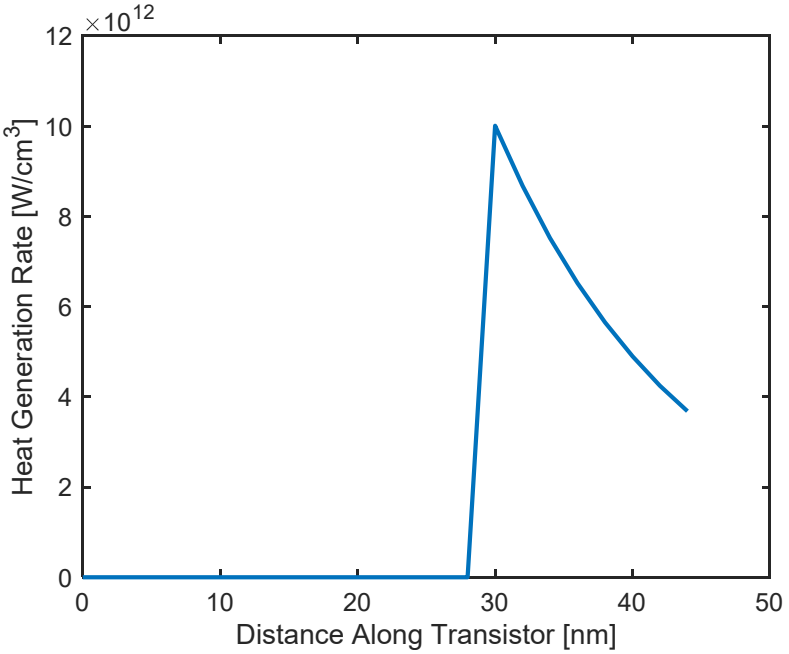

Fig. 46. Representative heat generation profile used in the nanowire transistor simulations.

Fig. 46 shows the volumetric heat generation rate for a peak generation rate of 1.0E13 W/cm^3 as a function of the x-distance from the source through the channel to the drain of the transistor. As was illustrated with the previous figures, the peak generation rate occurs at the end of the channel (distance of 28 nm) and extends significantly throughout the drain region.

The peak heat generation rate will also be affected by the level of doping within the source and drain regions. As Liao et al [89] points out, electron phonon scattering rates increase in a direct fashion with the dopant level. As electron phonon scattering rates increase, heat generation will increase accordingly. Dopant level increases from 1E20 1/cm^3 to 1E21 1/cm^3 or greater will push heat generation rates into the 1E13 W/cm^3 and 1E14 W/cm^3 region. Thus, studies to the effect of peak heat generation rates on thermal transport will be performed.

Simulations for the silicon nanowire transistor geometry show in Fig. 42 – 43 are performed with a constant heating rate (in time) and a time varying heating rate to demonstrate the on and off condition of the transistor. The characteristics of the time varying heating rate are determined by the period and duty cycle. Sensitivities will be performed to both factors to determine the effect on magnitude of the generated hot spot and thermal conditions.

The 1-d simulations involving parametric studies on the peak generation rate and transient characteristics are performed with purely specular boundary conditions in the y and z directions. This adiabatic boundary condition is recognized as a conservative condition. The effect of phonon transport to the surrounding material in the vicinity of the maximum heat generation rate location will be investigated using reflectivity values less than 100%. Physically this could be thought of as a result of the use of enhanced heat transfer materials in the vicinity of the

channel/drain transition region or the use of highly thermally conductive materials that still allow electrical insulation. Results of the silicon nanowire transistor simulations are illustrated in section 5.5.2.1.

4.9.2.2 FinFET Array Transistor

The FinFET transistor is currently the mainstream structure for logic devices. The IRDS predicts that it will remain in production for several years. A schematic of a FinFET array transistor is illustrated with Fig. 4b. The SPTM was applied to a representative geometry associated with these devices. The initial geometry simulated is illustrated with Fig. 47 below.

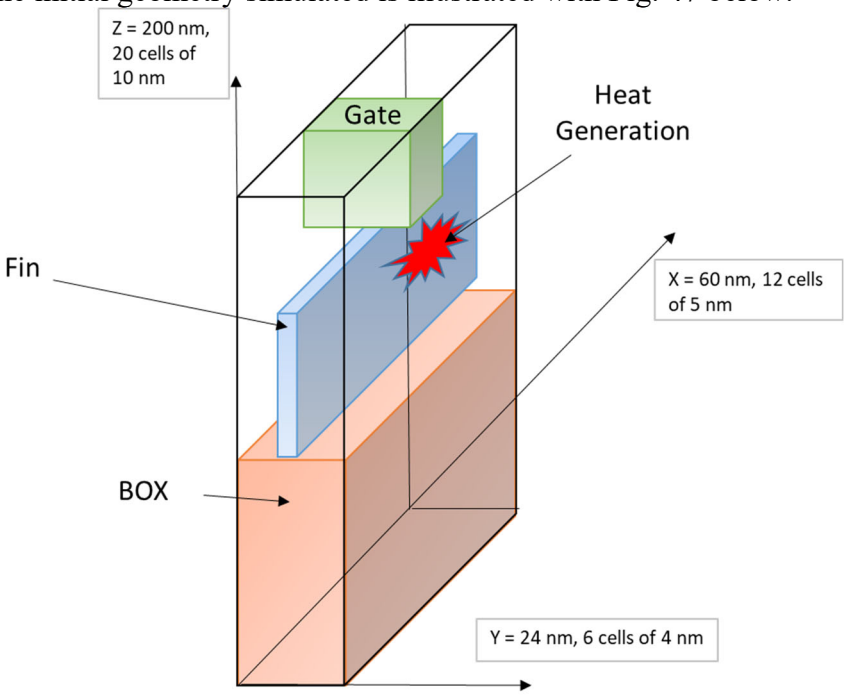

Fig. 47. Simulated geometry of a FinFET array transistor.

Thermal and geometric symmetry was assumed, such that a rectangular region around the center fin was chosen as the geometric computational domain. The symmetry assumption implicitly assumed all fins in the array were operating synchronously and an adiabatic thermal plane (no heat transfer) resulted in the middle of the region between the fins. This resulted in a conservative estimate of the thermal loading on the center fin. The 3D simulation domain consisted of 1440 rectangular cells in the domain. The entire domain is modeling as silicon. The fin itself consists of a region in the middle of the domain that is 60 nm in the X direction, 8 nm in the Y direction, and 30 nm in the Z direction. Heat generation occurs with the drain region of the fin which ranges from X dimensions of 40 nm – 60 nm. Heating is applied uniformly in the two cells representing the fin in the Y direction consisting of a width of 8 nm and the 3 cells in the Z direction with a height of 30 nm. In the X direction, the peak occurs at the channel/drain interface and extends into the drain region. The profile for heat generation in the X direction is the same as illustrated in Fig. 46.

Transient switching is simulated with the use of several periods at a 50% duty cycle. These include 10 ps, 50 ps, and 100 ps. In addition, the effect of the size of the unheated regions surrounding the fin in the Y direction is simulated by using different cell numbers and

dimensions in that direction. Three simulations were performed with the size of the unheated regions ranging from 8 nm, 4 nm, and 0 nm. The simulation results are shown in section 5.5.2.2.

5 Results and Discussion

5.1 Dispersion Results

The original lattice dynamics formulation implemented by Brown III in the SPTM utilized only first nearest neighbor interactions and force constants reported by Ghatak and Kothari [97]. The results of this calculation, which were previously reported by Wang and Murthy [56] (and reproduced by Brown III [9]), are illustrated in Fig. 48 in high symmetry directions. The Greek letters correspond to specific points in the FBZ of silicon and were discussed in reference to Fig. 13.

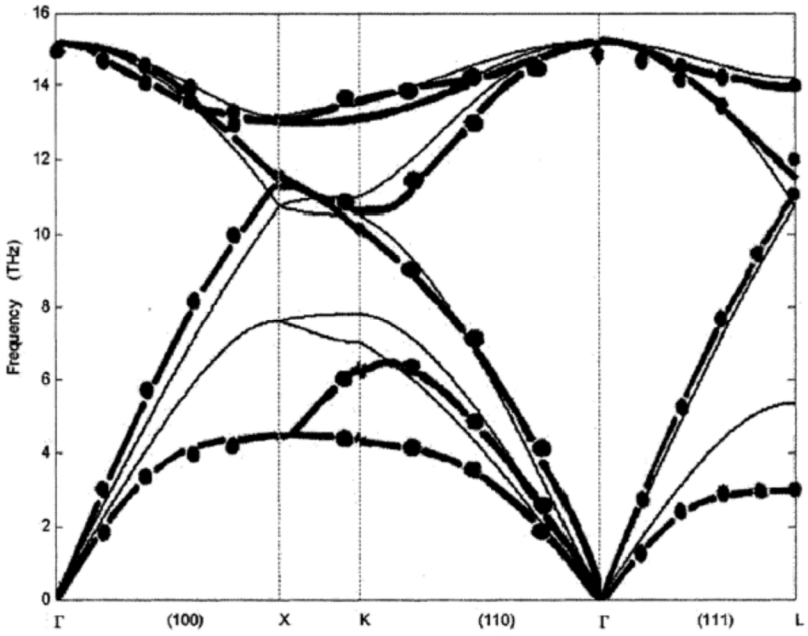

Fig. 48. Predicted dispersion results compared to experimental from previous lattice dynamics model (using first nearest neighbor approximation) implemented by Brown III [9]. Thin black lines are results from the previous SPTM, solid circles are experimental data, and thick black lines are from a bond charge model [56].

The thin black lines are the SPTM predictions and the solid circles are experimental data. At the worst case location (close to the X point) the prediction is off by about 75%. The results for the enhanced dispersion model implemented in this work compared to similar experimental data are shown in Fig. 49.

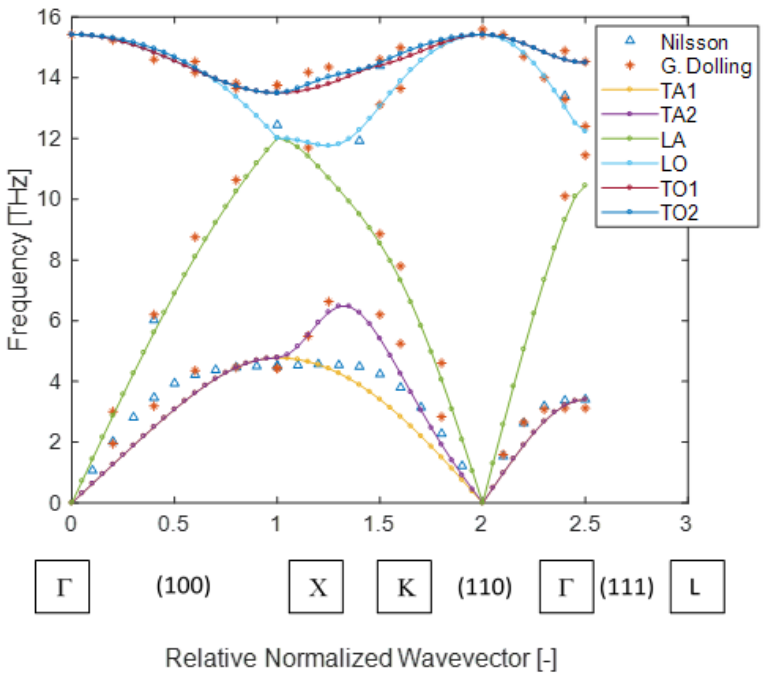

Fig. 49. Predicted dispersion results for lattice dynamics model (with up to second nearest neighbor interactions and force constants calculated from first principles DFT) compared to experimental. The predictions are for 500 K and the data was taken at 300 K. The triangles are from Nilsson and Nelin [70] and the stars are from G. Dolling [98].

There is much better agreement in the high symmetry directions with the enhanced dispersion calculation of the SPTM. At the worst case location, the model predictions are only off by 19%. In addition to results in high symmetry directions, the SPTM calculations produce dispersion relations in all directions within the FBZ. This is in contrast to many MC simulations such as those of Pop et al. [90], Mittal et al. [99], and Hao et al. [100], where dispersion relations are assumed to be isotropic and are developed from either fits of experimental data in high symmetry directions or from simple sin-shaped functions. The results of the complete anisotropic dispersion calculation of the SPTM are shown in Fig. 50.

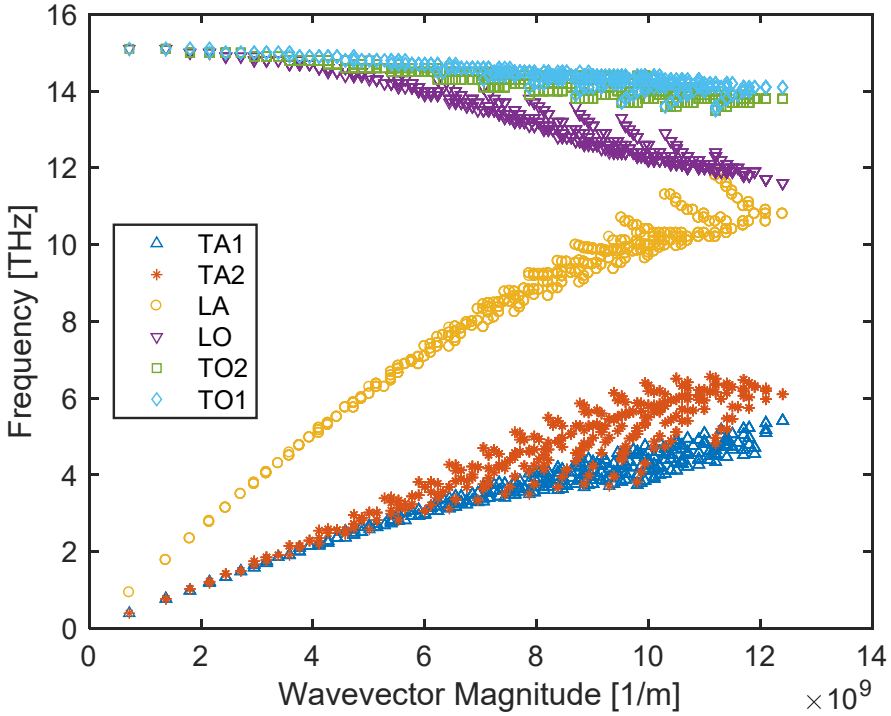

Fig. 50. Predicted dispersion results from lattice dynamics with second nearest neighbor interactions in all modeled directions in the FBZ. Mesh size of 14. Temperature of 500 K.

The results of Fig. 50 illustrate the dispersion relations for the standard modes including both acoustic and optical modes. Each mode shows a range of frequency results over a specific wavevector due to the modeling of the entire FBZ.

5.2 Three Phonon Scattering Results

Results of the implementation of the three phonon scattering model through the algorithm described in Section 4.4 will demonstrate that physically accurate results are produced. These include the facts that the phonon population returns to the Bose Einstein equilibrium [68] distribution if it is initially displaced from that condition and the rate at which the phonons representing a given condition decay back to equilibrium is physically reasonable and comparable to prior literature results. The single mode decay is shown by displacing single modes from equilibrium (one at a time) and allowing them to decay back to equilibrium. This is illustrated for a single representative pseudostate with Fig. 51,

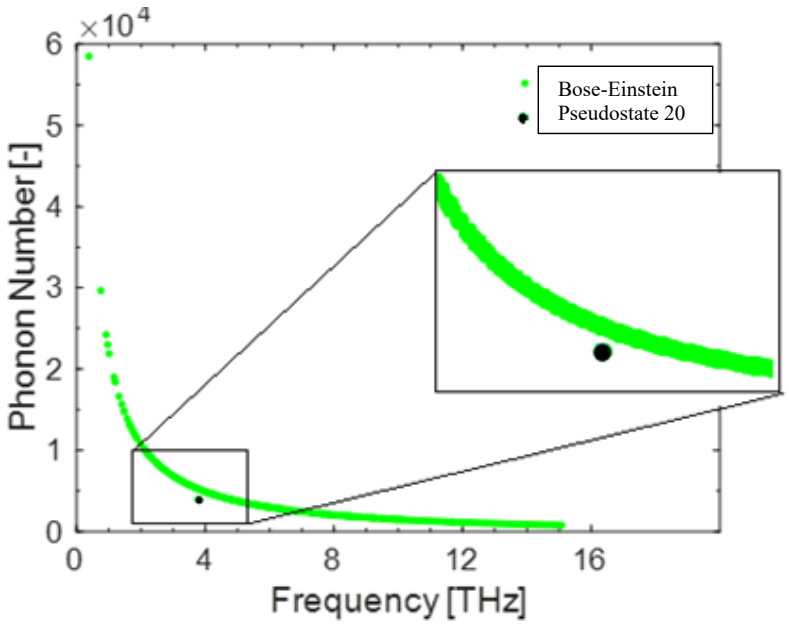

Fig. 51. Deviation of a single phonon pseudostate from equilibrium. Pseudostate 20, frequency of 3.7879 THz, equilibrium population of 5183, initial population of 3891.

where the figure shows pseudostate number 20 in black, artificially deviated from the Bose-Einstein distribution (green) by 25 %. The transient response of the population of this state is shown with Fig. 52.

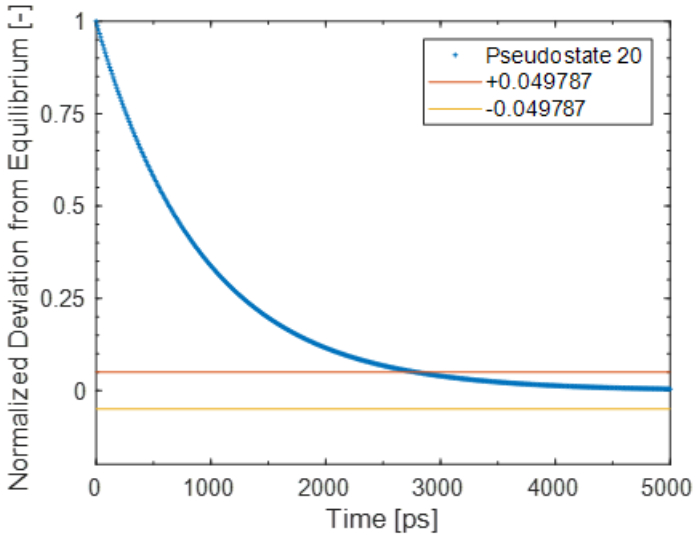

Fig. 52. Normalized single mode phonon population decay for pseudostate 20 due to three phonon scattering. The red and yellow lines indicate bounds of +- 4.9787 % around zero. For an exponential decay, the response should return to within these bounds within three time constants.

Fig. 52 is exemplar of a critically damped case. An underdamped case is shown below in Fig. 55. As stated, since all other states are at equilibrium in this scattering simulation, this is representative of the single mode decay rate. Typically within the literature, phonon state

dynamics are illustrated in this manner with the Single-Mode Relaxation Time (SMRT) concept. The SMRT is defined as the representative time over which a given state decays to equilibrium if it is the only state perturbed from equilibrium. It is illustrated with equation 129 [27],

$$-\frac{\partial n_{ks}}{\partial t}\Big|_{scattering} = \frac{n_{ks}-\bar{n}_{ks}}{\tau_{ks}} \tag{129}$$

where n_{ks} is the time dependent phonon distribution function, $\bar{n}_{ks}$ is the Bose Einstein distribution function, and τ_{ks} is the relaxation time associate with the mode ks. This concept inherently assumes that the decay curve is exponential in nature and this is not always a good fit. To determine a metric that is comparable to the SMRT this work uses the idea of a time constant. The time constant is determined by assuming that the population of a given mode will have decayed to within 4.9787 percent of equilibrium within a time equal to three time constants. Thus, a SMRT is determined for this work by finding the time constant and dividing that result by three. For pseudostate 20, this concept would give a SMRT of 2810/3 ps or 937 ps. SMRT values are illustrated as a function of pseudostate frequency for all of the acoustic and optical modes in the (100) direction in Fig. 53.

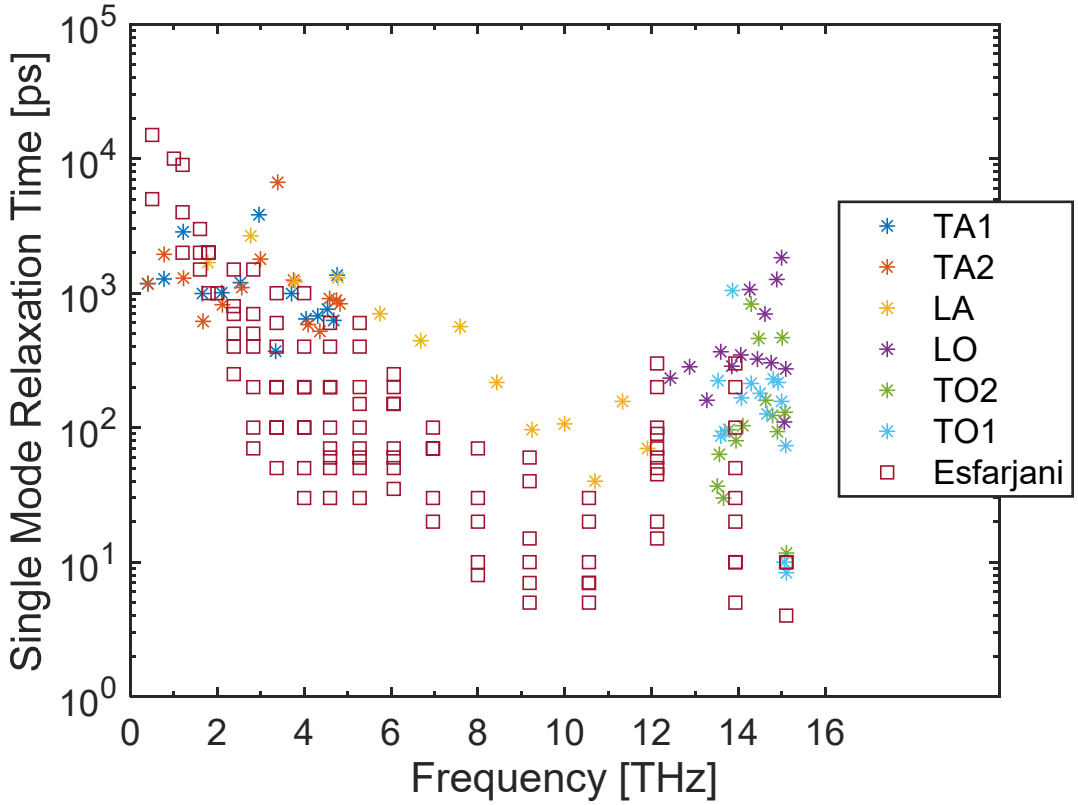

Fig. 53. Single Mode Relaxation Times. Predictions in (100) direction, Gruneisen of 1.1 and T= 500K. Note that the data from Esfarjani [57]is for all directions and at 277K.

Fig. 53 compares the values computed from this work to those of Esfarjani et al. [57]. The Esfarjani computations are consider to be higher fidelity due to the computation of the third order interatomic force constants from DFT. The general range of values and trends are in agreement. It is noted that this is not exactly a 1:1 comparison as the Esfarjani data is for all directions and differs in temperature from those of this work. In addition, it is also noted that SMRT values computed from the SPTM may overpredict some of the relaxation times and

underpredict the scattering rates for certain pseudostates. This observation and its effects are expanded upon in additional analysis and results further on in this section.

Single mode decay as characterized with the SMRT is not a realistic scenario. A transient that would have a tendency to perturb one state from equilibrium will perturb many other state from equilibrium. An example of this is phonon generation from electron-phonon scattering discussed in section 4.6. As such, the phonon population dynamics are studied in a condition where all pseudostates are displaced from equilibrium. This is simulated by randomly displacing all pseudostates from equilibrium by at most positive thirty-five percent or negative thirty-five percent. The scattering algorithm is then implemented and the phonon population is allowed to relax due to three phonon interactions back to equilibrium. The initial phonon population relative to equilibrium for this simulation is shown in Fig. 54,

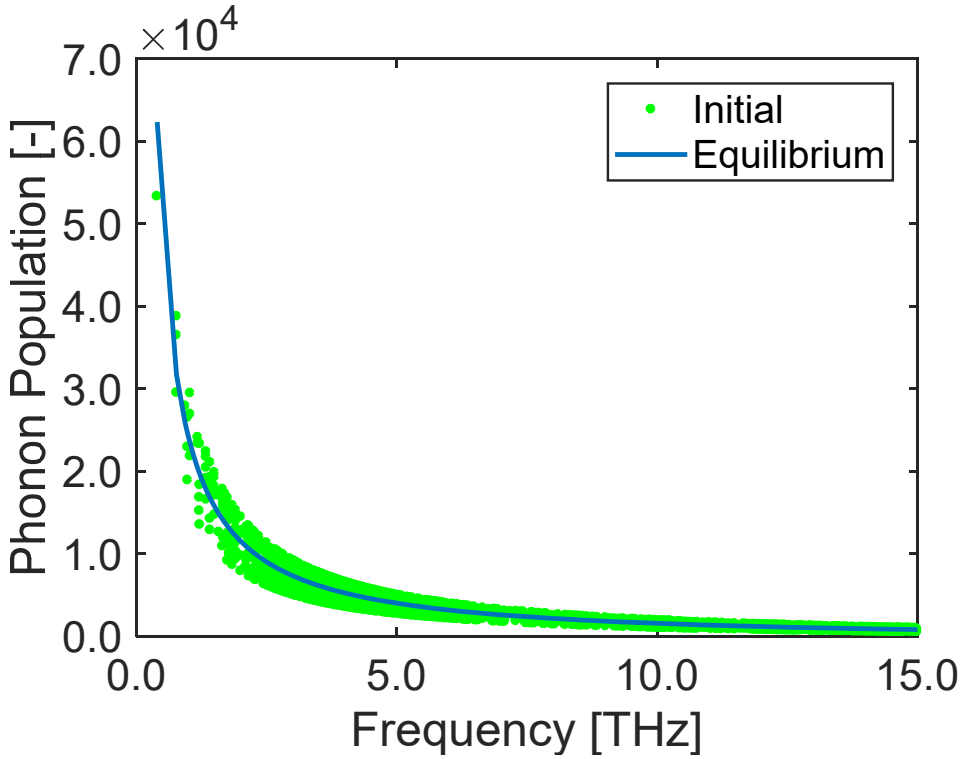

Fig. 54. Initial phonon population for scattering testing relative to equilibrium where all pseudostates are displaced from their equilibrium populations. Isothermal 100 nm cell at a temperature of 500 K.

where the solid blue line represents the equilibrium number of phonons expected in a 100 nm cell of silicon at 500 K as a function of frequency in THz. The solid green circles show the artificially displaced phonon population at time zero. As the calculation proceeds over a given amount of time, the relaxation of the population to equilibrium is evident with Fig. 55. The convergence of the population to equilibrium as a relative deviation from equilibrium is illustrated at three times.

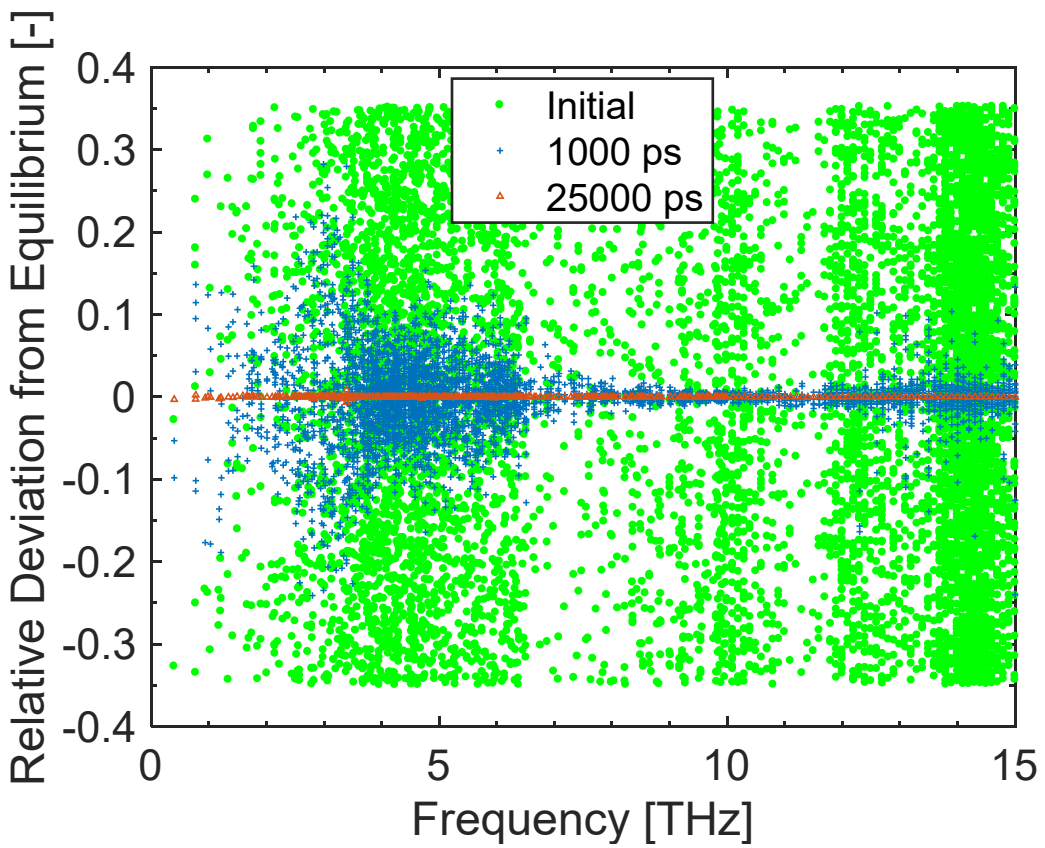

Fig. 55. Relative deviation of the phonon population from equilibrium shown at three times after initially being displaced by up to 35% and subject to the action of three phonon scattering.

The solid green circles are the initial phonon population, the blue plus signs indicate the relative deviation after 1000 ps, and the red triangles after 25000 ps. The results demonstrate that absent any external influences, there is a tendency for the phonon population to be driven toward equilibrium by three phonon scattering. This is physically reasonable behavior and expected from the formulation of the scattering algorithm.

The results from Fig. 55 show the overall phonon population dynamics but, it is also of interest to examine individual pseudostate dynamics. This can be shown with the specific phonon populations as a function of time for a select number of pseudostates. The relaxation of the six pseudostates (at six different frequencies) corresponding to a given wavevector are considered in Fig. 56. This relaxation rate is referred to as the Multi-Mode Relaxation Time (MMRT) to distinguish it from the SMRT.

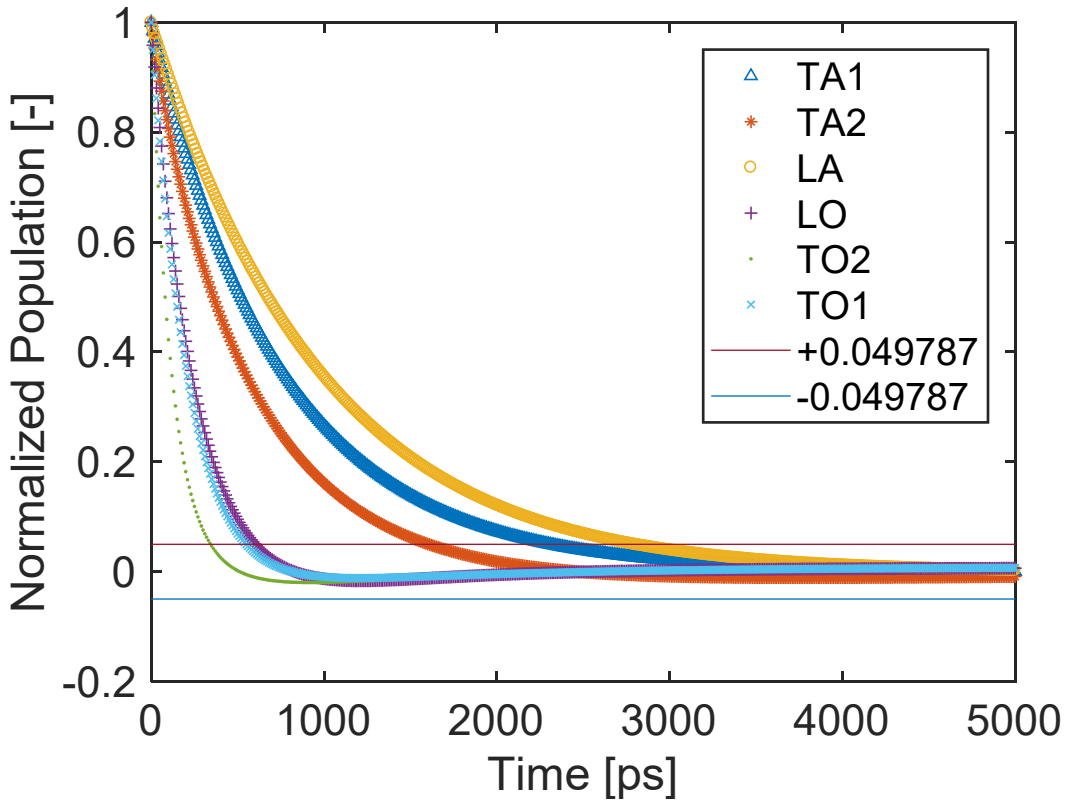

Fig. 56. Normalized phonon population decay due to three phonon scattering for six pseudostates at a wavevector of 3.76E9 1/m. The frequencies range from approximately 2 THz for TA1 to 14.9 THz for TO1. The +- 4.9787 % bounds used to determine the time constant and thus the MMRT are also shown for reference.

The different markers illustrate the decay curves of the acoustic and optical modes at a wavevector of 3.76E9 1/m in the (100) direction. All curves show the normalized deviation in the phonon population from equilibrium as a function of time. As each curve represents a different phonon pseudostate at a given wave vector, they are all at different frequencies. In general, the higher frequency optical modes have smaller MMRT than the relatively lower frequency acoustic modes. This is due to the fact that the scattering strength is directly related to the frequency of the mode as well as the fact that the higher frequency modes have a larger number of scattering partners as they can decay into many different combinations of pseudostates.

The implementation of scattering within the SPTM allows investigation into a phenomenon that may not be available in other models. This phenomenon is the sensitivity of the MMRT to the initial deviation and condition of partner pseudostates from equilibrium. The symmetry of the FBZ in the SPTM and the random nature of the initial artificial perturbation from equilibrium allows this to be determined as multiple samples of decay from a given pseudostate are available within a given simulation. This is shown with Fig. 57.

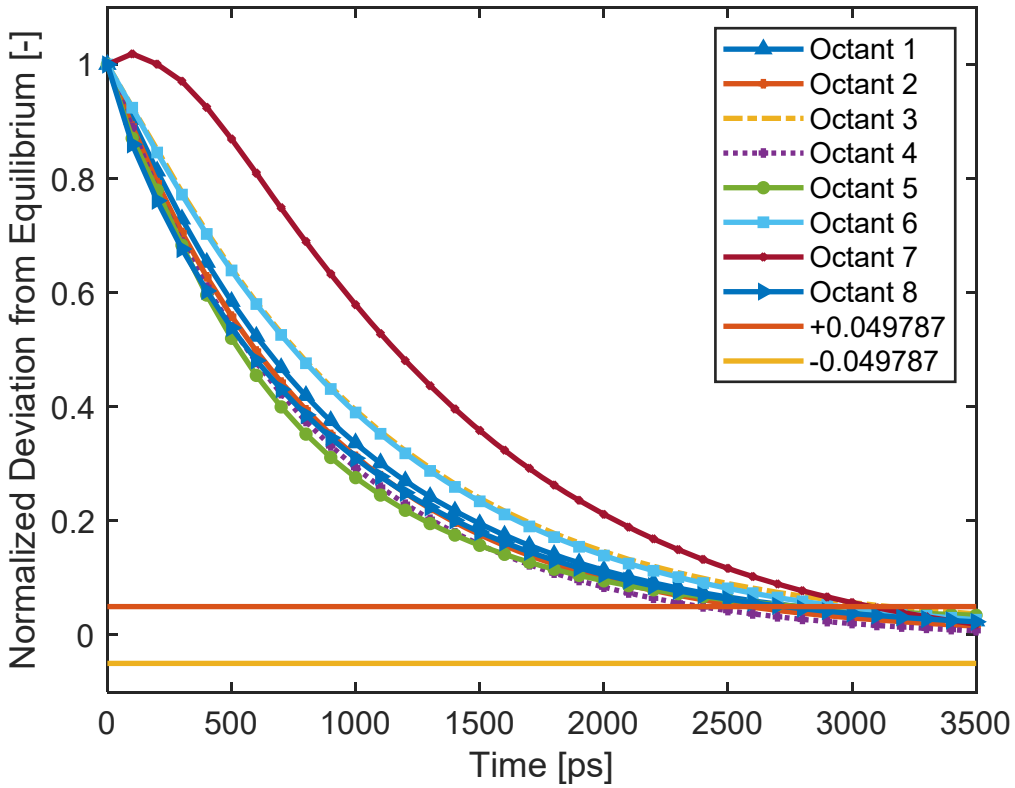

Fig. 57. Normalized population decay for the eight replicates of a given pseudostate in their respective octants.. LA, (100) direction, ω = 3.7879 THz. The +- 4.9787 % bounds used to determine the time constant and thus the MMRT are also shown for reference.

The symmetry of the FBZ (divided into octants) dictates that each phonon pseudostate is replicated eightfold. Each pseudostate has exactly the same characteristics (wavevector magnitude, frequency, and population) represented in the SPTM but occur at different wavevector directions. This implies that the three phonon partner states associated with the above pseudostates share the same characteristics of wavevector and frequency but differ in the relative initial deviation of those states from equilibrium due to the random initial condition. The different initial conditions of partner states leads to the eight different decay curves in Fig. 57. One may postulate that the random nature of the displacement from equilibrium would produce a net zero effect on the scattering rates. This is not the case as all interactions are not equally weighted in regards to the overall effect on the population of a given state. Some have a larger affect due to the characteristics of the interacting phonons. The occupancy of the partner states has a direct effect on the computed scattering rates for a given interaction and thus has a direct effect on the relaxation of the state to equilibrium despite all other factors being equal. That is, the rate of decay of any given pseudostate to equilibrium is directly affected by the state of the entire system. This leads to variability in computation of the MMRT. This variability is shown for all the longitudinal acoustic pseudostates in the (100) direction with Fig. 58.

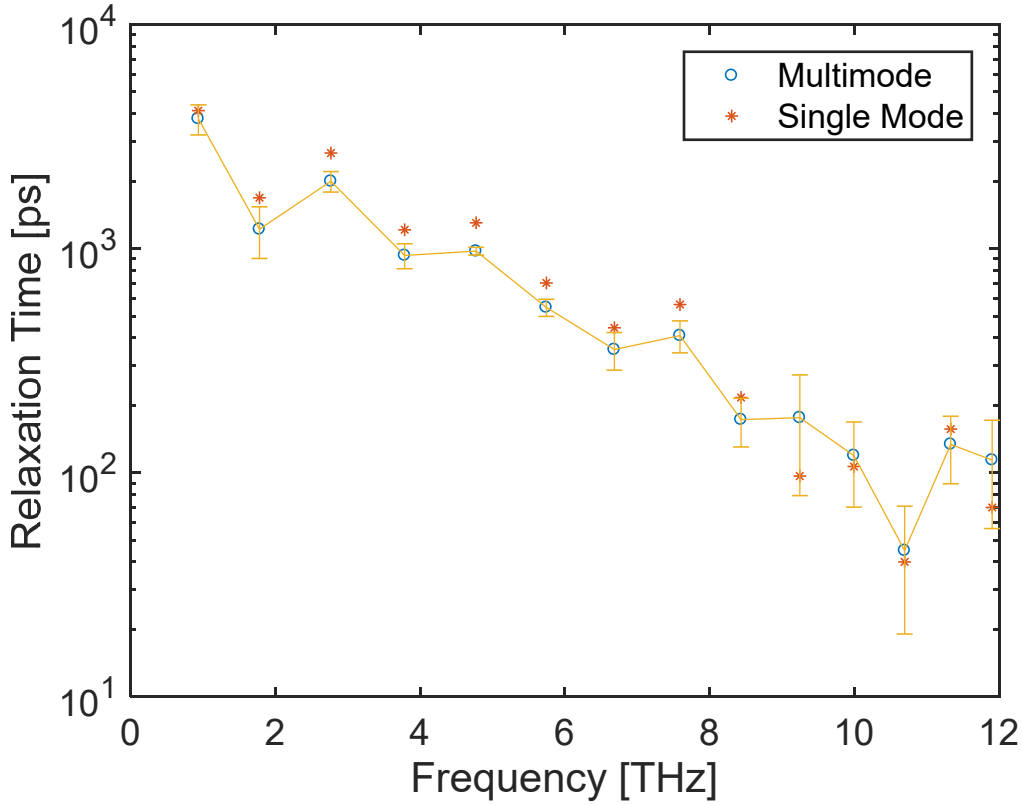

Fig. 58. Longitudinal acoustic MMRT as a function of frequency with error bars compared to SMRT in the (100) direction with a Guneisen parameter of 1.1, and T= 500K. The error bars indicate a symmetric 95% confidence interval. They appear unsymmetrical due to the logarithmic scale.

Fig. 58 shows the average MMRT for the longitudinal acoustic states in the (100) direction computed from decay rates of the eight symmetric states in the FBZ. It demonstrates that significant variability in the MMRT can occur due to the exact initial configuration of all partner pseudostates.

Initial comparisons of the relaxation times predicted with the SPTM to those of prior published work indicated an under-prediction of the three phonon scattering rates associated with some pseudostates. The effects of this on the overall performance of the SPTM became apparent when running 1-d simulations of a silicon nanowire with both the drift models and three phonon scattering were implemented. The results indicated that the SPTM was over-predicting thermal conductivities at Fourier length scales. This is directly attributed to the under-prediction of three phonon scattering rates. As such, the Gruneisen parameter (directly related to the strength of the three phonon interaction and the scattering rate) is treated as an adjustable parameter to allow the SPTM to better predict physically expected results in the Fourier regime. A sensitivity of the Gruneisen parameter to thermal conductivity at Fourier length scales was performed to select the appropriate value to use. The results of the sensitivity are illustrated with the Fig. 59.

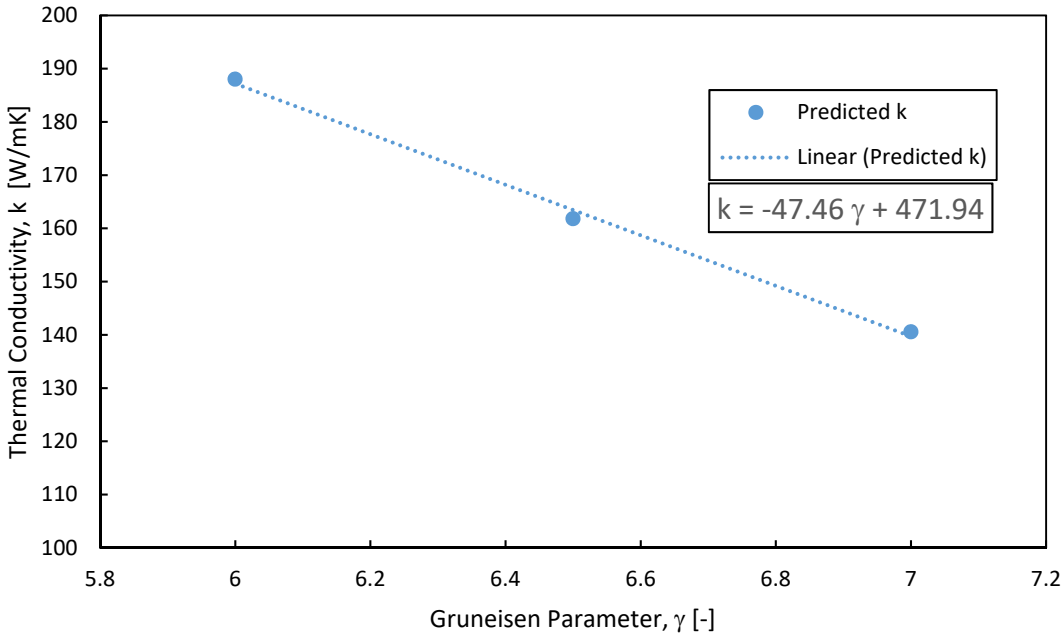

Fig. 59. Effect of the Gruneisen parameter on the resulting thermal conductivity of a 4000 nm long section of silicon with the left boundary temperature of 282 K and right boundary temperature of 272 K. The dashed line indicates a linear fit to the three data points shown with the equation in the text box where k is the thermal conductivity and γ is the Gruneisen parameter.

The results of Fig. 59 show the predicted thermal conductivity in a 1-d calculation of a section of silicon 4000 nm long for various values of the Gruneisen parameter from 6.0 to 7.0. The simulations were performed with isothermal boundary conditions of 282 K on the left boundary and 272 K on the right boundary. At an average temperature of 277 K, the published experimental value of bulk silicon thermal conductivity is approximately 177 W/mK [101]. Thus, the Gruneisen parameter was set to a value of 6.2 using the linear fit to reproduce this result.

Using this value of the Gruneisen parameter, the MMRT predicted by the SPTM are in better agreement with the prior published work of Esfarjani [57]. The comparison of the MMRT using of Gruneisen of 6.2 to the Esfarjani data is illustrated in Fig. 60.

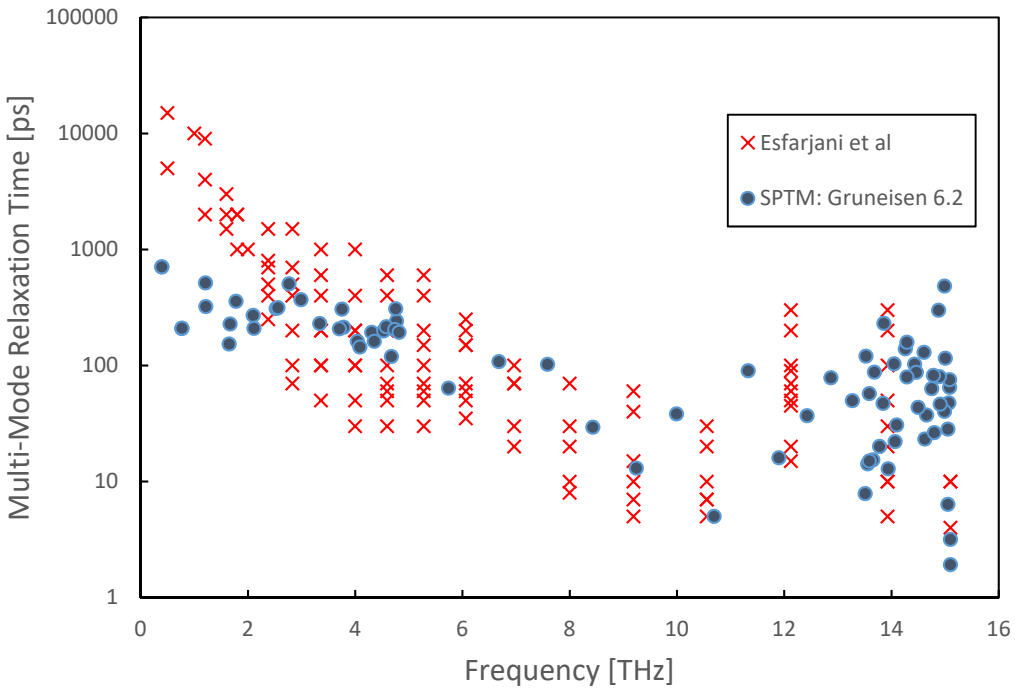

Fig. 60. Comparison of relaxation times as a function of frequency predicted using the SPTM with a Gruneisen of 6.2 to those of Esfarjani [57]. SPTM predictions are for all of the pseudostates in the (100) direction.

The results of the comparison indicate that the adjustment of the Gruneisen parameter to reproduce physically expected results at Fourier length scales leads to a better representation of the three phonon scattering strength. This will ensure that the SPTM is appropriately treating the effect of the three phonon interaction from the ballistic to the Fourier regime.

5.3 Heat Generation Results

Implementation of the electron phonon scattering algorithm results in a computation of the number of phonons generated in a given geometric domain in a given amount of time as a result of the heat generation produced from this interaction. Results of this computation will show that the energy input rate will be shown to be equal to the integrated energy of the phonon modes, the modal dependent phonon generation rates are physically reasonable and consistent with other published work, and heat generation computations at Fourier length scales will show that effective temperatures meet theoretical predictions.

Volumetric heat generation leads to a given amount of energy input to a geometric cell for a given size cell and simulation timestep. A heat generation rate of 2.6E12 W/cm^3 will lead to an energy input of 7.02E-21 J for a cubic cell size of 2.7E-20 cm^3 and a timestep of 1.0E-13 s. The energy input is distributed among the pseudostates. As energy conservation is met, the cumulative energy added to each pseudostate should equal the overall energy input. This is verified with Table 7 below.

Table 7. Verification of conservation of energy for heat generation calculations

Pseudostate	Frequency [THz]	Energy Added [J]	Cumulative Energy [J]
65846	10.79	7.75E-26	7.02E-21
65847	11.73	6.62E-26	7.02E-21
65848	13.81	2.79E-25	7.02E-21
65849	14.10	2.85E-25	7.02E-21
65850	5.41	2.81E-26	7.02E-21
65851	6.10	1.59E-27	7.02E-21
65852	10.82	8.16E-26	7.02E-21
65853	11.60	6.54E-26	7.02E-21
65854	13.80	2.78E-25	7.02E-21
65855	14.10	2.85E-25	7.02E-21

The table illustrates the last ten entries of the 65856 pseudostates modeled and demonstrates that the cumulative energy calculated is equal to the cellular energy input.

The distribution of the heat generated among the phonon modes is determined based off of the combination of the strength dependent parameter and an estimate of the interaction density as is detailed in section 4.6. The net phonon generation rate in geometric cell subject to a heat generation rate of 2.6E12 W/cm^3 is illustrated with Fig. 61.

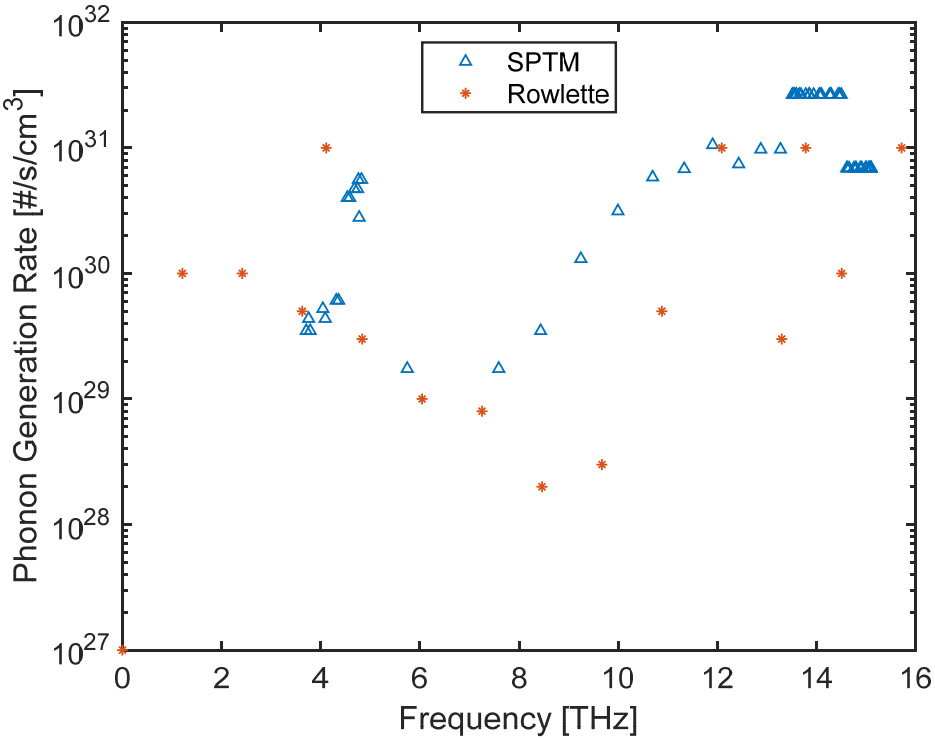

Fig. 61. Phonon generation rate as a result of electron-phonon interactions. Cell heating rate of 2.6E12 W/cm^3. SPTM comparisons to those of Rowlette and Goodson [73].

Fig. 61 shows the phonon generation rate plotted against the phonon frequency in THz for both the SPTM prediction and those of Rowlette and Goodson [73]. The results for the SPTM prediction are only plotted for the first 84 phonon pseudostates in the (100) direction. Both computations use the volumetric heat generation rate of 2.6E12 W/cm^3. The SPTM model predictions appear reasonable relative to the published work. Rowlette and Goodson use electron-phonon scattering rates computed from Fermi's Golden Rule for both intra-valley and inter-valley scattering. The deformation potential approximation is used to estimate the change in potential produced from the phonon deformation of the atomic lattice. The electron-phonon scattering rates are integrated over the wavevector space to determine the number of phonons emitted or absorbed of a given wavevector and mode. Electron transport is modeled using the Monte Carlo technique and the phonon distribution function is computed from the phonon Boltzmann Transport Equation. In general the modal specific phonon generation rates predicted by the SPTM illustrate physically expended trends based on knowledge of the momentum and energy selection rules for the electron-phonon interaction and the manner in which both acoustic and optical phonons distort the silicon lattice.

At Fourier length scales, the effect of internal heat generation on the material temperature distribution is known to be parabolic. The SPTM was used to simulate conditions approaching this to validate the heat generation model. The simulation results are compared to the continuum predictions using the Heat Conduction Equation with Fig. 62.

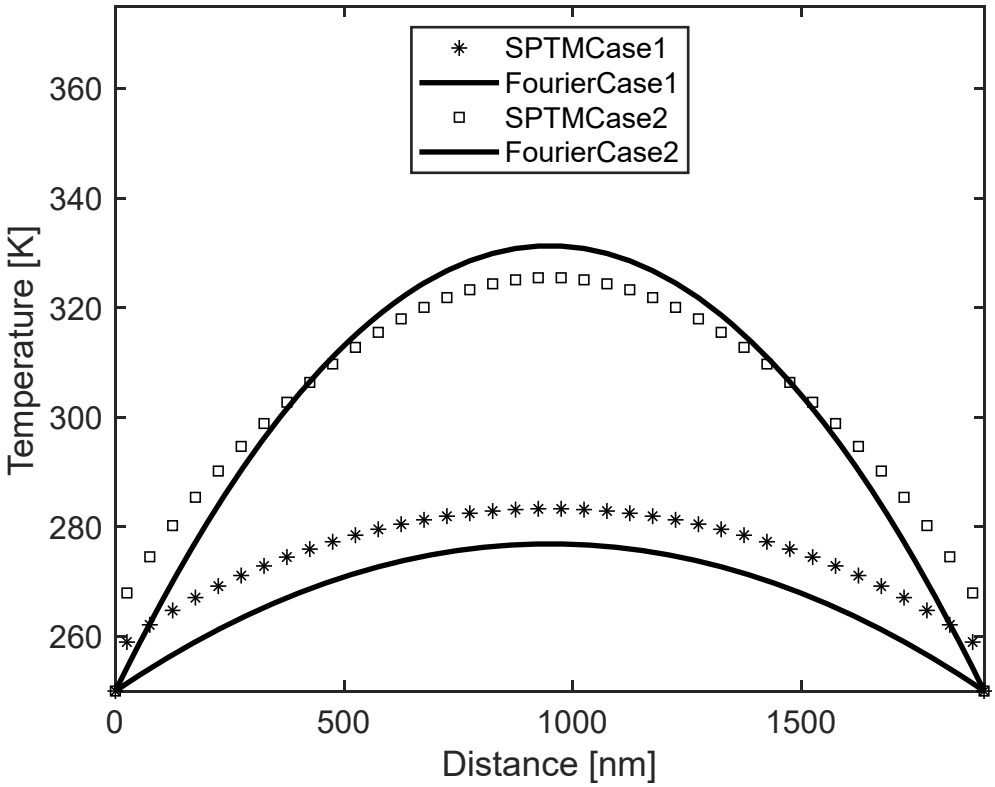

Fig. 62. Comparison of 1-d results with heat generation to that predicted with the Fourier heat conduction equation. Length of domain is 2000 nm. Heating rates of 1.0E10 W/cm^3 and 2.0E10 W/cm^3 are simulated.

Fig. 62 shows the 1-d temperature distribution in a silicon domain that is 2 μm in length when it is subject to uniform heat generation rates of 1.0E10 W/cm^3 and 2.0E10 W/cm^3. The SPTM predictions are shown against the Fourier prediction. The Fourier predictions are plotted with the constant thermal conductivity values shown in the plot. In general, the SPTM predictions are within 10% of the Fourier values. There is evidence of some ballistic jump at the boundary cells and it is possible that refinement of the three phonon scattering models could yield improved results but, the current model is able to represent the appropriate physical phenomena for continued use. It should also be noted that that the heat generation model inputs energy into specific modes meant to represent heat generation from electron phonon scattering. This could skew result comparisons to the Fourier results as the Fourier model assumes local thermodynamic equilibrium.

5.4 Drift Results

Verification of the drift model shows thermally expected behavior of phonon transport in silicon from the ballistic to the diffuse regime, across different temperature ranges, and in one, two, and three dimensions. Drift results encompass the results of the computational implementation of both the drift algorithm and three phonon scattering algorithms.

One-dimensional simulations demonstrate physically expected behavior at both the ballistic limit and the purely diffusive regime. At the ballistic limit, three phonon scattering is essentially unimportant and thus, drift is unimpeded without scattering. This implies that the temperature profile vs. length should mimic the theoretical limit given by Stefan-Boltzmann which is shown in the following equation,

$$T^4 = \frac{1}{2}(T_L^4 + T_R^4), \tag{130}$$

where T_L is the left boundary temperature and T_R is the right boundary temperature. The SPTM prediction for a length of 200 nm between left and right boundary temperatures of 25 K and 15 K is illustrated against the theoretical limit with Fig. 63.

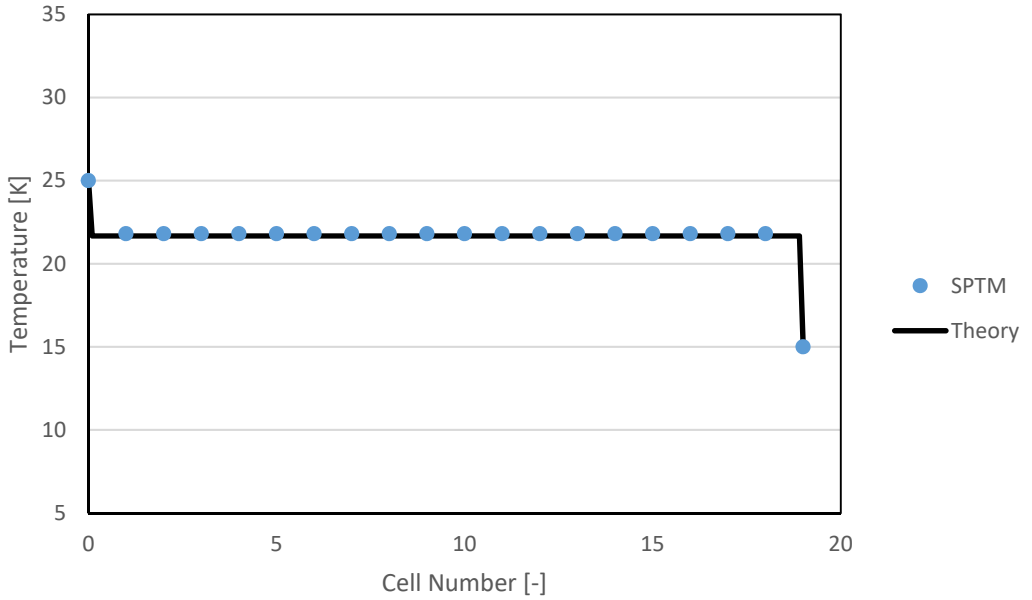

Fig. 63. Drift prediction of the SPTM against the theoretical limit in the Ballistic regime [9].

At higher temperatures three phonon scattering becomes more important and as the length increases thermal behavior should approach the Fourier limit. Predicted effective lattice temperatures as a function of length from 20 nm to 2000 nm with a left and right boundary temperature of 505 K and 495 K respectively is illustrated with the Fig. 64.

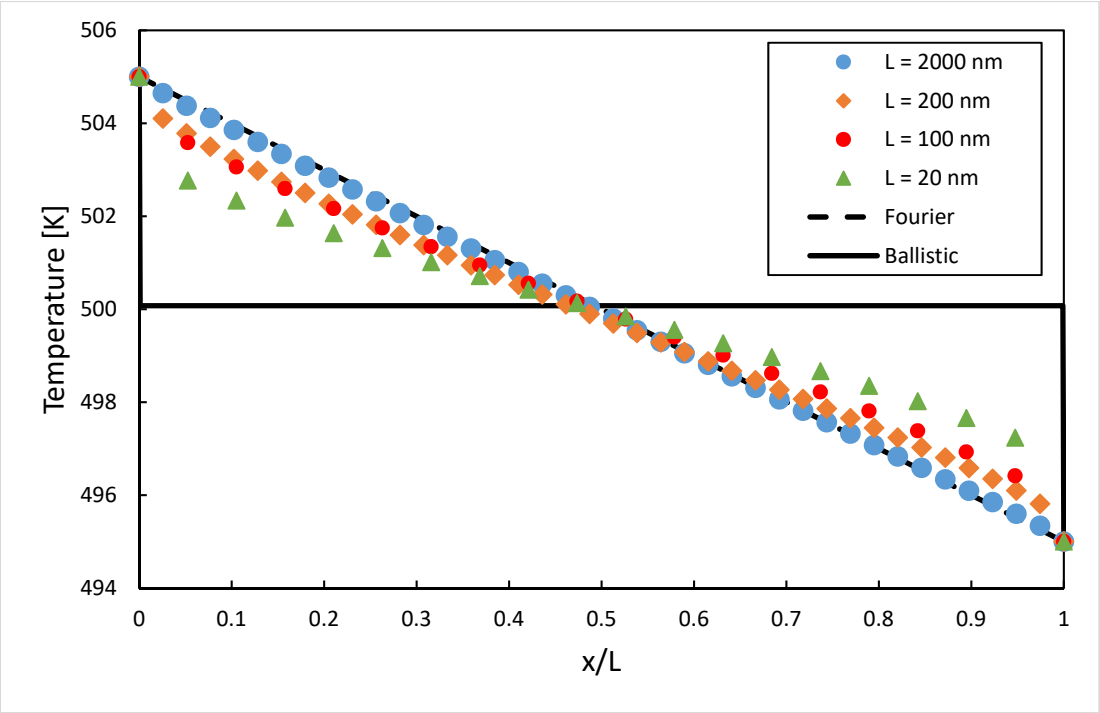

Fig. 64. SPTM predicted temperature distributions to illustrate the size effect. Domain lengths of 2000 nm, 200 nm, 100 nm, and 20 nm are shown. Theoretical predictions at both the ballistic and Fourier regimes are plotted for comparison.

Fig. 64 shows the approach from Fourier to ballistic behavior. As the total length decreases, some phonons can transport across the domain without experiencing a scattering event and leading to more ballistic behavior. However, at the elevated temperatures of the simulation, three phonon scattering still impedes phonon transport to preclude fully ballistic behavior.

At Fourier length scales, thermal conductivity should approach the bulk values for silicon at the various temperature. As part of the implemntation of the three phonon scattering algorithm, the scattering strength parameter (Gruneisen parameter) was adjusted such that the thermal conductivity met bulk silicon values at a tempature of 277 K. Thus, it will be expected that the model predicts the appropriate thermal conductivity at this temperature. Fig. 65 demonstrates the model predictions at other temperatures.

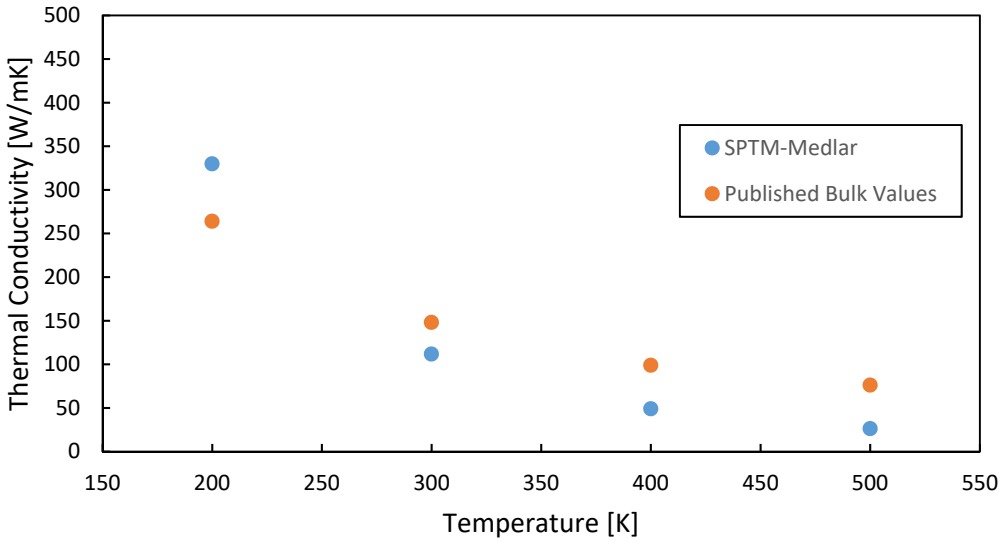

Fig. 65. SPTM prediction of thermal conductivity in a 1D silicon domain of 2000 nm in length with 40 cell compared to published bulk values [101].

The SPTM model predictions of thermal conductivity are within the range of expectations. They demonstrate the correct trends with temperature. Deviations may indicate that adjustments could be made to improve the effect of scattering with changes in temperature. In comparison to the Brown III, the predicted values of thermal conductivity for the Medlar SPTM for a domain of 40 cells is 26 W/mK whereas the Brown III prediction is 222 W/mK. The published values is approximately 75 W/mK [101].

Transient model predictions against the expected behavior at Fourier length scales are shown in Fig. 66. Fig. 66 illustrates the transient change in temperature of the center cell in a 2000 nm long, 1-d domain of silicon. It is compared against the Fourier prediction using equation 3. Also for comparison, the results of the Brown III implementation of the SPTM are shown.

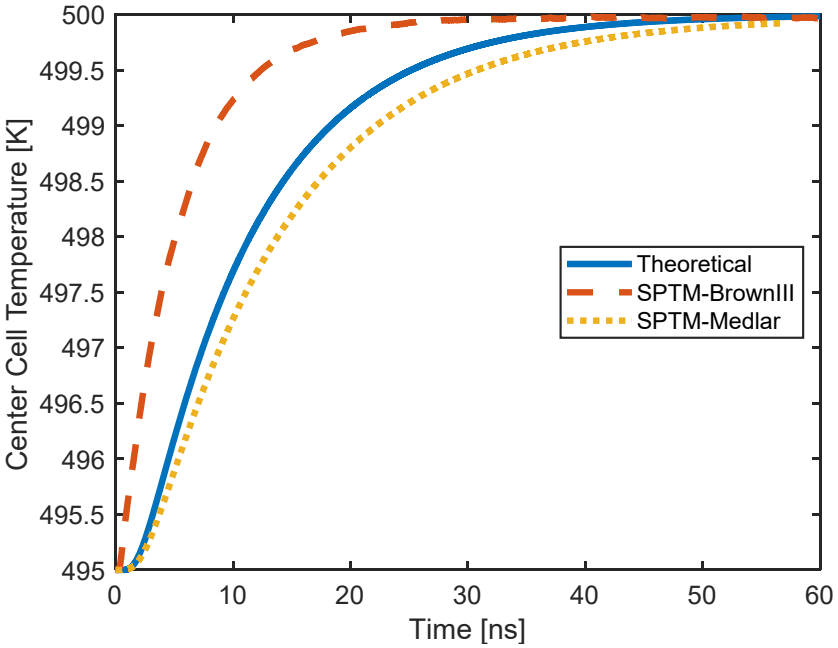

Fig. 66. Transient, 1-d comparison of SPTM predictions to heat conduction equation (equation 3) at Fourier length scales. Domain is 2000 nm divided into 40 cells. The SPTM predicted temperatures is an average from cell 19 and 20 with cells 0 and 39 representing the boundaries. Thermal diffusivity of 3.7E-5 m^2/s was used in the heat conduction equation.

Compared to the Fourier expected results, the results indicate that the model is behaving as would be physically expected. Compared to the Brown III SPTM, the Medlar SPTM better predicts the theoretical results with the same geometric discretization of 40 cells.

The SPTM phonon polarization heat fluxes are compared against published results of Pascual-Gutierrez [66] and the prior published SPTM of Brown III. This is illustrated with Fig. 67.

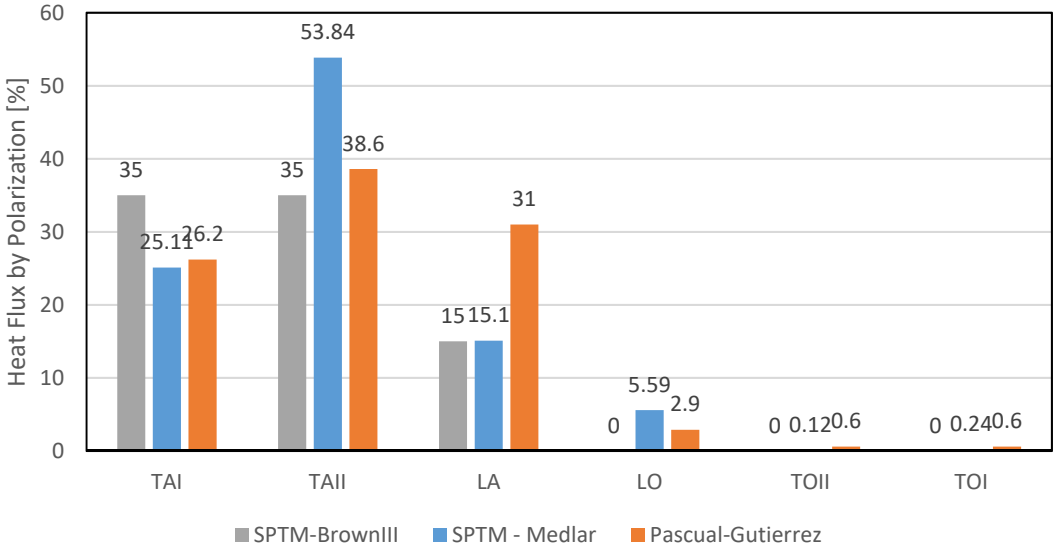

Fig. 67. Phonon polarization heat flux as a percentage of total heat flux for 1-d 4000 nm length with left and right boundaries of 305 K and 295 K respectively.

Results illustrate acoustic modes carry the majority of the heat. This is as expected due to their larger numbers and higher group velocities. The model of Brown III produced identical results for both of the transverse acoustic modes and did not include optical modes. The current SPTM shows better agreement with the results of Pascual-Gutierrez. Despite the lower overall heat fluxes of optical modes they are still important for thermal transport because most heat generation occurs within these modes and they often decay into acoustic modes.

The geometric space discretization was investigated with a 1-d grid sensitivity. A 100 nm domain was simulated with a step change in the temperature at the left boundary condition from 300 K to 400 K at time zero. The right boundary was maintained at 300 K. Cell numbers ranging from 10 to 50 were used and the transient results are illustrated with Fig. 68.

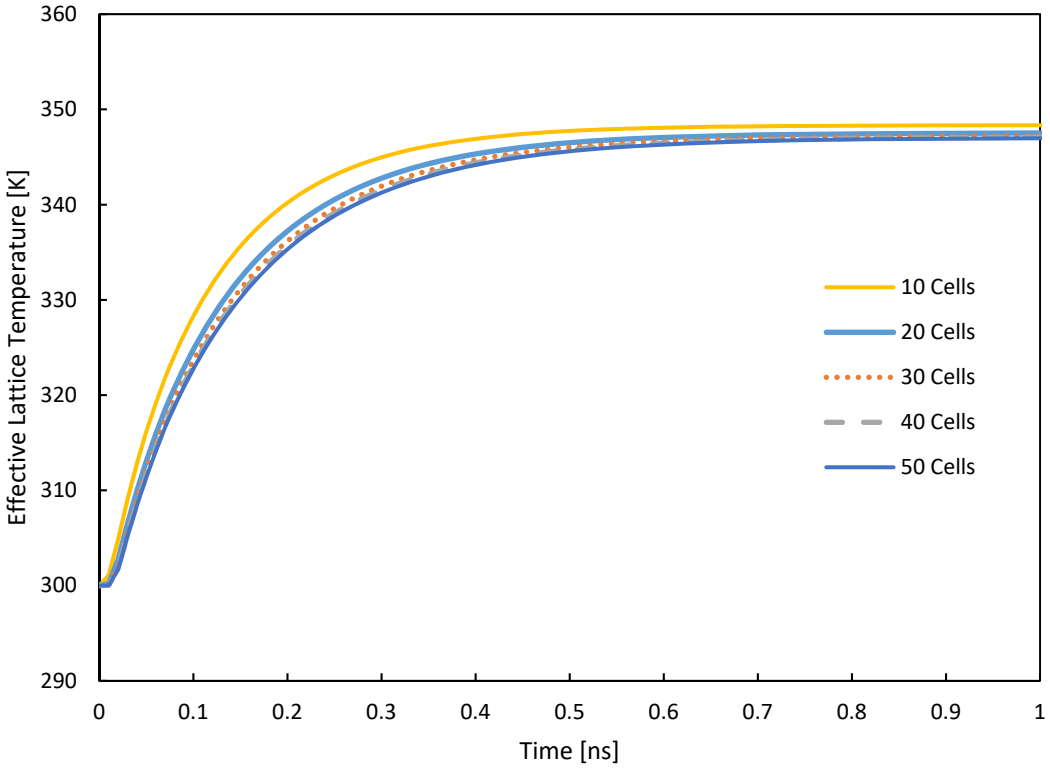

Fig. 68. Transient, 1-d grid sensitivity for the SPTM with a domain length of 100 nm. The left boundary jumps to 400 K at time zero and the right boundary is held at 300 K. Effective lattice temperature are shown at the center of the domain as a function of time for cell numbers from 10 to 50.

The results of Fig. 68 illustrate a relatively small sensitivity of the SPTM results to the computational grid size. At the largest difference, the effective lattice temperature rise of the 10 cell case differs by approximately 10% to the 50 cell case. If 20 cells are used, this difference becomes approximately 4%.

Drift simulations and results are also performed in two and three dimensions. Selected results are meant to highlight the capability of the SPTM and demonstrate physically expected behavior. As an example of a two dimensional simulation, Fig. 69 shows a two dimensional domain consisting of 50 cells. The length of the domain in the x direction is 500 nm and the length in the

z direction is 250 nm. The cells in the upper left and upper right are held at isothermal values of 300 K and 200 K respectively. All other boundaries are purely specular.

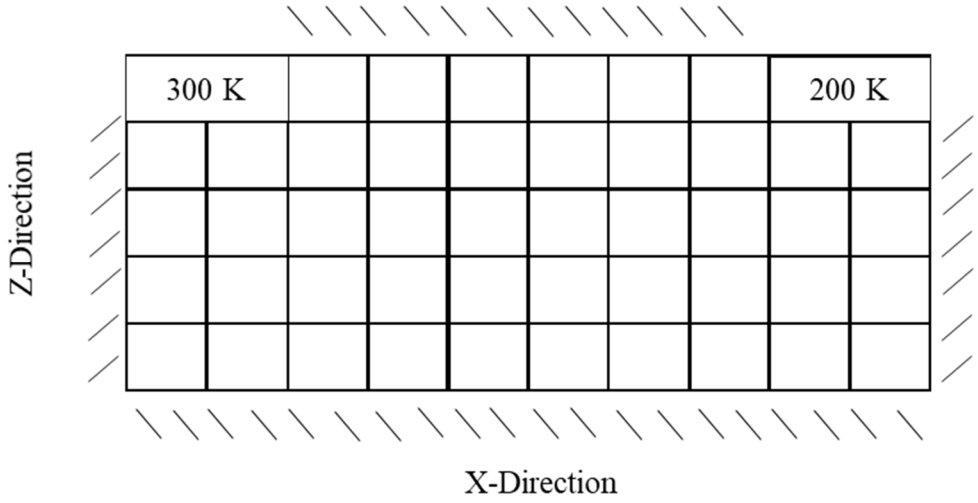

Fig. 69. Simulation domain for the illustration of drift in two dimensions. Cell dimensions are 50 nm by 50 nm. All boundaries except those illustrated as temperature boundaries are purely specular as indicated by the cross hatching.

Fig. 70 shows the predicted surface plot of effective lattice temperatures after a steady state simulation is reached.

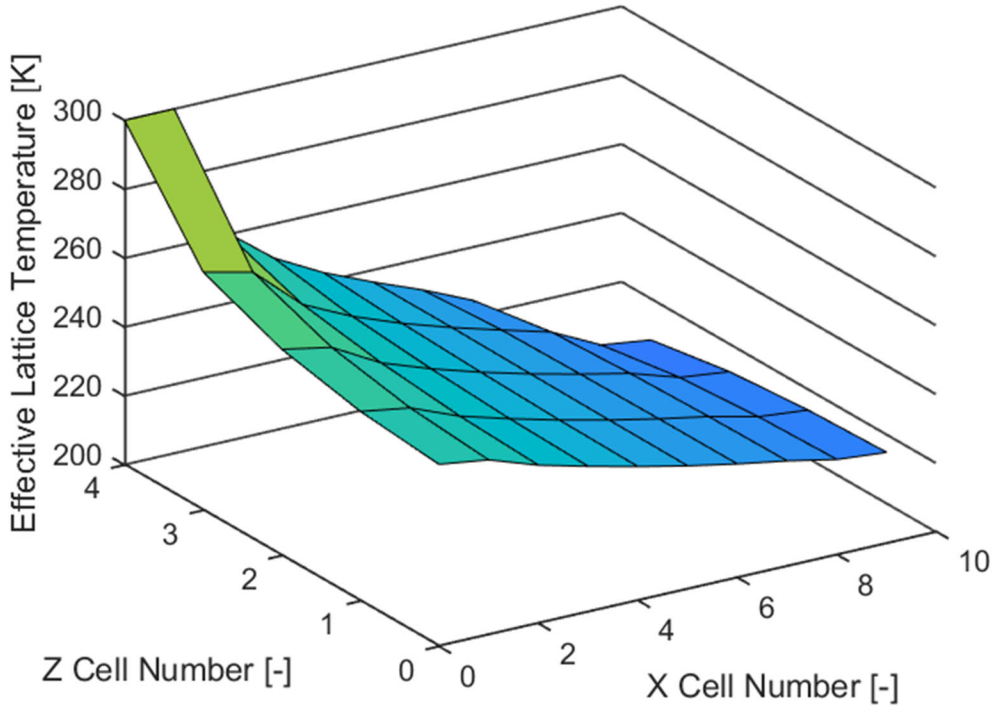

Fig. 70. Surface of effective lattice temperatures for the illustration of drift in two dimensions.

The temperature distributions from the simulation illustrated in Fig. 70 demonstrate physically expected behavior for two dimensional drift.

5.5 Device Modeling Results and Discussion

The device modeling incorporates all of the model enhancements discussed previously and shows that the improved SPTM can be an accurate, flexible, and efficient thermal transport tool to inform thermal design.

5.5.1 Comparison to Prior Published Works

Section 4.9.1 detailed the modeling approaches chosen for comparison. This section will demonstrate the results of the SPTM simulations compared to those cases.

5.5.1.1 Case 1: DAS - Rhyner and Luisier Simulation Results

Rhyner et al [41-43] demonstrated the relationship between the maximum effective lattice temperature and the power dissipation in a silicon nanowire transistor as well as the effective lattice temperature profile from the source to the drain of the transistor using a NEGF formulation. The SPTM was applied to similar conditions as was specified in their model and the results of peak effective lattice temperature as a function of total power dissipation in the nanowire are demonstrated in Fig. 71.

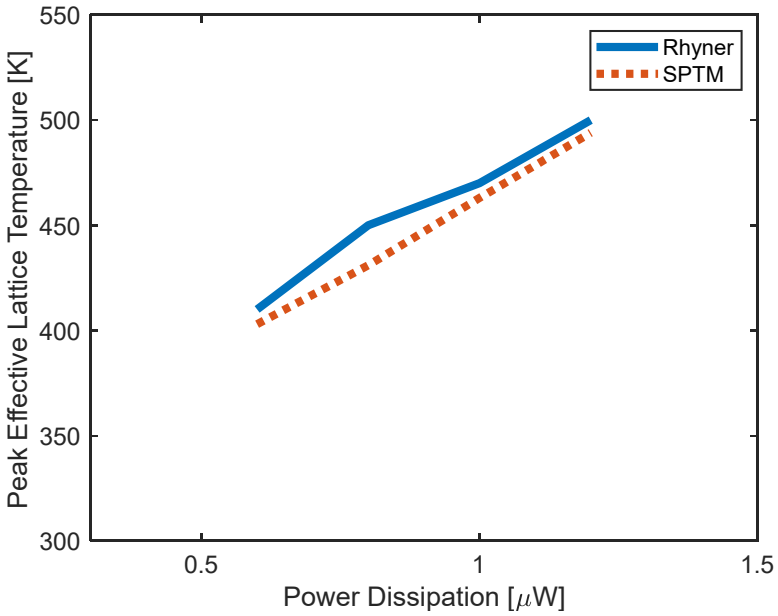

Fig. 71. Effect of power dissipation on peak effective lattice temperature. Comparison of SPTM to Rhyner [41-43].

Fig. 71 illustrates the direct and approximately linear relationship between peak effective lattice temperatures and overall power dissipation predicted using both simulation methodologies. The SPTM results differ from the Rhyner results by at most 4%.

Fig. 72 illustrates the comparison of the effective lattice temperature distribution along the length of the nanowire transistor from the source to the drain at the peak overall power simulated of 1.2 μW.

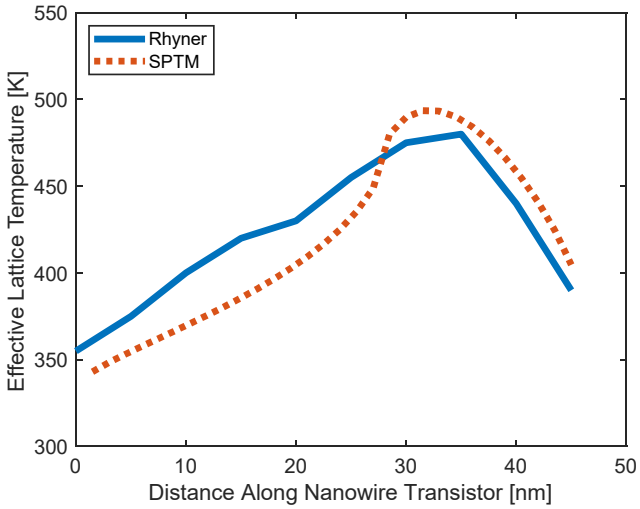

Fig. 72. Effect of power dissipation on peak effective lattice temperature. Comparison of SPTM to Rhyner [41-43] at an overall power dissipation of 1.2 μW.

The results of Fig. 72 show that the SPTM prediction is within approximately 8% of Rhyner. The results of Fig. 71 and 72 show that the SPTM predictions of effective lattice temperatures compare well with the higher fidelity, more fundamental simulations of Rhyner [41-43]. Effective lattice temperatures in any region of the domain are effected by the processes of phonon generation, three phonon scattering, and drift. Thus, this comparison provides confidence in the models and implementation of the SPTM and the ability to predict nanoscale thermal behavior.

5.5.1.2 Case 2: 1D Monte Carlo - Rowlette and Goodson Simulation Results

Comparisons of the SPTM to Rowlette and Goodson [73] indicate a much larger effective temperature rise than their predictions. This is illustrated with predicted effective lattice temperatures as a function of position with the maximum heating profile (1.0 V bias condition) in Fig. 73.

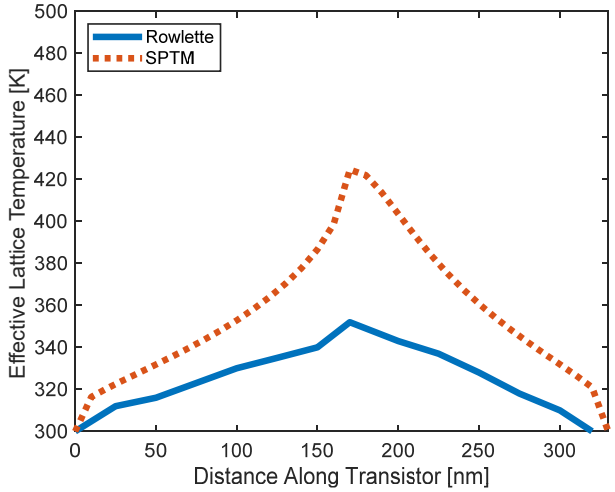

Fig. 73. Predicted effective lattice temperatures along the length of a 1-d transistor. Comparison of SPTM to Rowlette [73].

The overall power dissipation rate is estimated from the heating profiles to be similar in both cases. The SPTM predicts a larger build-up of energy before a steady state energy flux is reached. This would be indicative of longer lived optical phonons and lower drift velocity. Confidence in the thermal predictions of the SPTM are gained when one considers that the Rowlette and Goodson phonon transport model includes simplifying assumptions that the SPTM does not make. The split flux form of the BTE breaks the phonon population into two pieces. One that is near the equilibrium distribution that follows Fourier's law. The other is subject to local deviations from equilibrium. Isotropic dispersion based on the use of simple quadratics is implemented. In addition, energy is not conserved with local scattering events and constant relaxation times are assumed for optical phonons which are important for joule heating. The SPTM offers a more detailed modeling approach for phonon transport where the entire phonon population is modeled in an anisotropic manner. It is noted that the Rowlette and Goodson model electron transport and electron phonon interactions in a more detailed approach. This is taken into account with the direct use of their heat generation rates.

5.5.1.3 Case 3: 3D Monte Carlo - Shomali Simulation Results

Shomali et al [92] predicted effective lattice temperatures for two different boundary conditions with the heat generation profile detailed in section 4.9.1.3. The initial case (Case I) set the bottom boundary to an isothermal value of 300 K. The predicted temperatures after 500 ps of simulation are shown in Fig. 74.

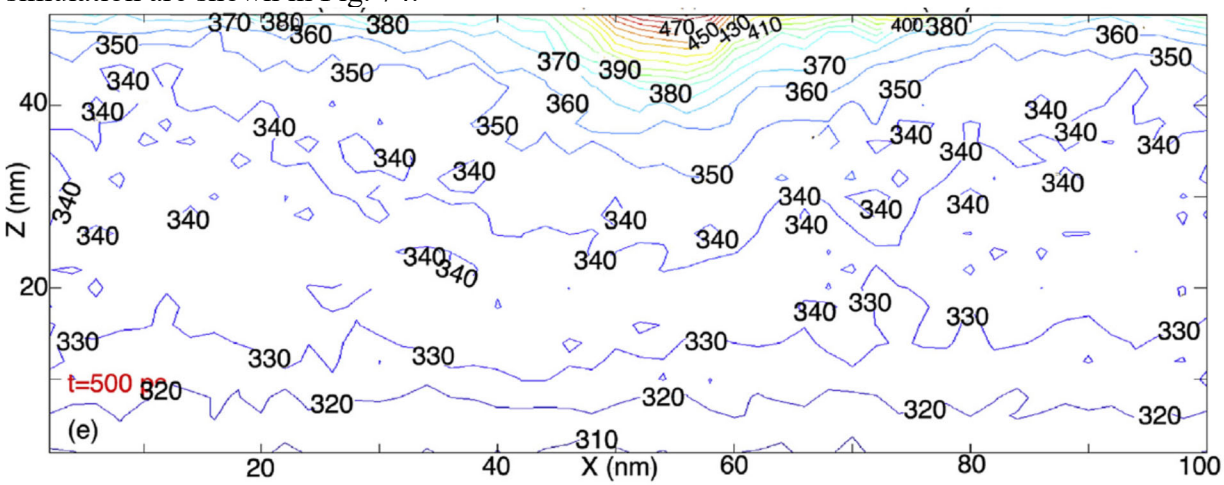

Fig. 74. Shomali contour plot of effective lattice temperatures with open bottom boundary. Reproduced from [92].

The contour plot of Fig. 74 illustrates highest temperatures near the maximum heat generation location. The peak temperature is show to be approximately 470 K. The SPTM was applied to predict phonon transport under similar conditions to this simulation. A contour plot of the peak effective lattice temperatures predicted by the SPTM for the same condition is shown in Fig. 75.

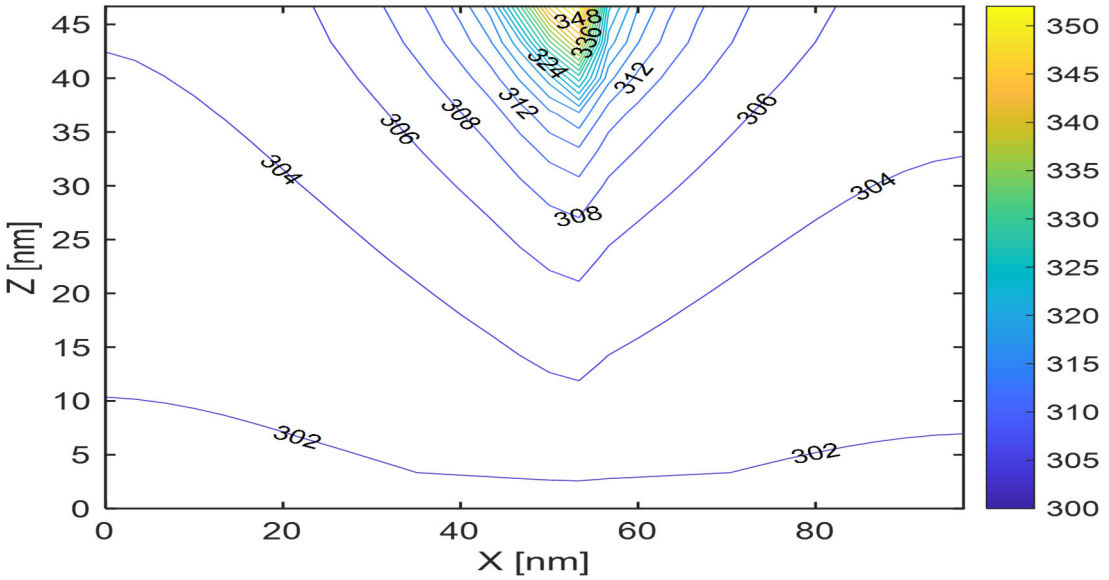

Fig. 75. SPTM predictions of effective lattice temperatures to match Shomali Case I.

The SPTM simulation predicts a lower overall effective peak temperature than the Shomali simulation. Also, Shomali states that a large temperature jump occurs in the simulation at approximately 22 ps from around 400 K to 470 K. The SPTM does not predict any large temperature excursions and no discontinuities in the effective temperature vs. time profile.

Shomali et al [92] also simulated effective temperatures with an isothermal bottom boundary and isothermal locations to represent source and drain contacts. The effective temperatures after 500 ps of simulation time are illustrated with Fig. 76.

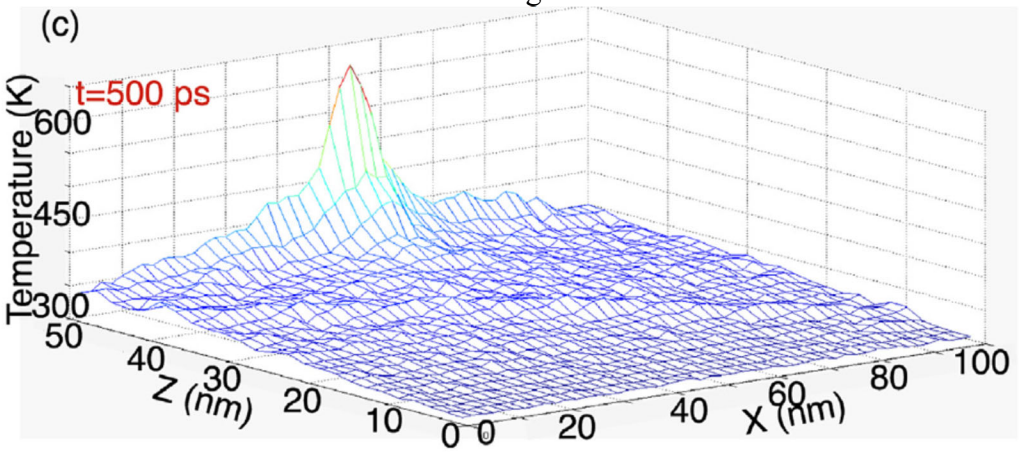

Fig. 76. Shomali mesh plot of effective lattice temperatures with isothermal bottom and source and drain boundaries. Reproduced from [92].

The SPTM was applied to predict effective lattice temperatures at a scenario similar to Case II. The SPTM predicted effective lattice temperatures are illustrated with Fig. 77.

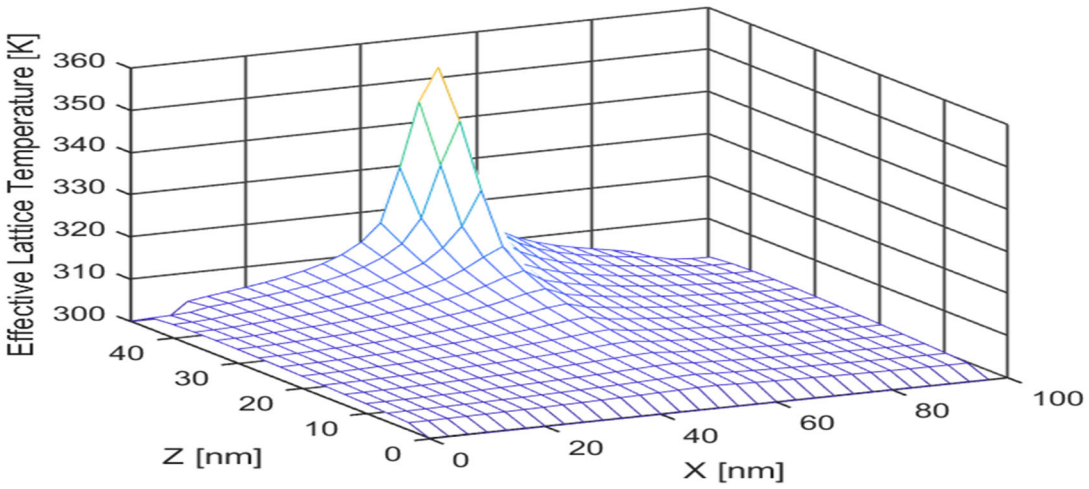

Fig. 77. SPTM predictions of effective lattice temperatures to match Shomali Case II.

Shomali states that the presence of two open boundaries in addition to the bottom open boundary strengthens the effect of the hot spot. That is, the maximum effective lattice temperature rises more quickly and reaches a larger value than in Case I. Shomali states that this is due to the fact that the presence of the side open boundaries reduced the temperature gradient in the z direction and leads to a larger temperature before a steady state is reached. The SPTM simulations do not agree with the Shomali simulations. The presence of the side boundaries reduces the peak lattice temperature slightly. These factors along with the lower phonon fidelity of the MC approach indicate little confidence in the Shomali results when compared to those of the SPTM simulations.

5.5.1.4 Case 4: Fourier – Chhabria Simulation Results

The results of Chhabria's Fourier simulations of a FinFET array transistor is illustrated with the filled contour plot of Fig. 78.

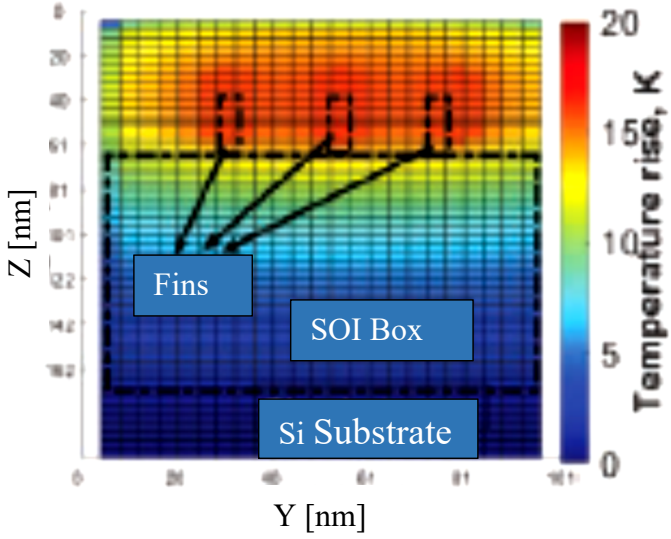

Fig. 78. Chhabria temperature contours in a Y-Z plane for a 3 fin FinFET array transistor at the end of the channel region. Reproduced from [94].

Fig. 78 show approximately a 12 K maximum temperature rise in the channel region of the center fin for the FinFET array transistor. The SPTM results for a 2-d simulation of a FinFET are illustrated with a filled contour plot in an X-Z plane in Fig. 79.

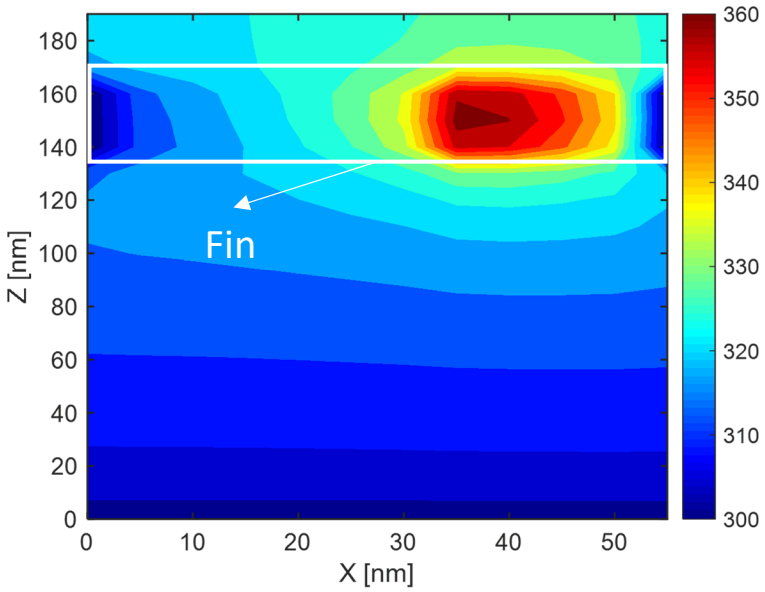

Fig. 79. SPTM contours of effective lattice temperatures in an X-Z plane for a 2-d simulation of a FinFET transistor.

The SPTM results illustrate a peak effective lattice temperature of approximately 360 K at the end of the channel region of the FinFET. The SPTM results were produced with a more realistic heating profile and heating rate. The use of Fourier's law at the length and time scales of the FinFET array is not appropriate for the prediction of local thermal conditions due to the breakdown of local thermodynamic equilibrium that was illustrated in section 1.3. Phonon transport modeling with the SPTM is a better tool for the prediction of the non-equilibrium local phonon conditions that occur in FinFET array transistors and this will be detailed further with the results of the design tool demonstrations of section 5.5.2.

5.5.1.5 Comparison Method Summary

The comparison method rubric defined in Table 6 of section 4.9.1 was used to rate the SPTM to the representative cases that span the range of modeling approaches. The results of the ratings are illustrated with the bar chart of Fig. 80.

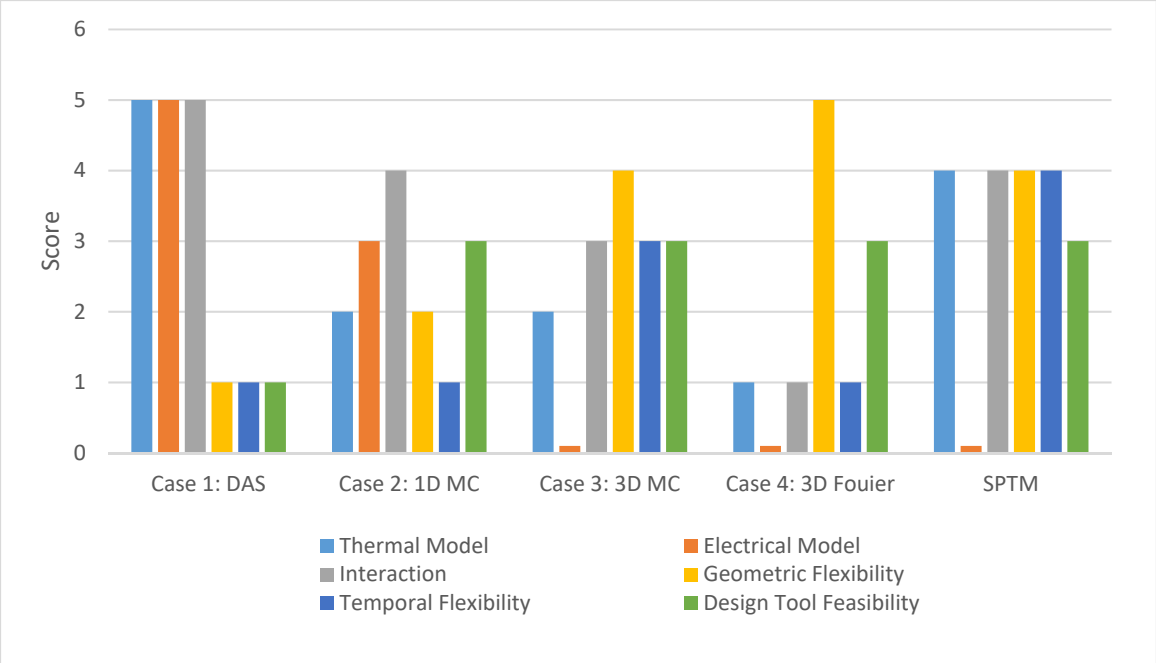

Fig. 80. Comparison of SPTM to state of the art simulations.

Fig. 80 demonstrates that the SPTM has the highest overall combination of accuracy and flexibility when compared to the other methodologies. As an additional measure of flexibility, the SPTM was able to simulate all of the other geometries/conditions presented in the four cases studied whereas the other modeling approaches would be limited in their ability to do the same.

5.5.2 Design Tool Demonstration Results

5.5.2.1 Silicon Nanowire Transistor

The initial devices modeled with the SPTM consist of silicon nanowire transistors detailed previously. As mentioned in section 4.9.2.1, studies to the effect of peak heat generation rates on thermal transport conditions were be performed. Fig. 81 illustrates the resulting effective lattice temperature along the length of the transistor as a function of peak heat generation rates ranging from 5E12 W/cm^3 to 7.5E13 W/cm^3.

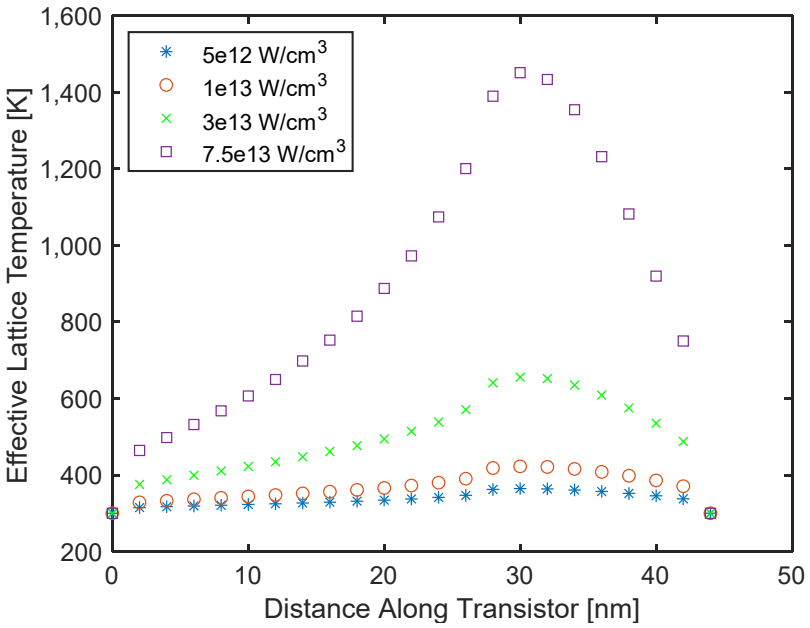

Fig. 81. Effect of peak heat generation rate on effective lattice temperature along a nanowire transistor.

The results of Fig. 81 show significant peaking of lattice temperatures in the drain region of the transistor as the heating profile is most pronounced in this region. This suggest that drain design is important for thermal considerations.

The peak effective lattice temperature is plotted as a function of the aforementioned peak heat generation rates with Fig. 82.

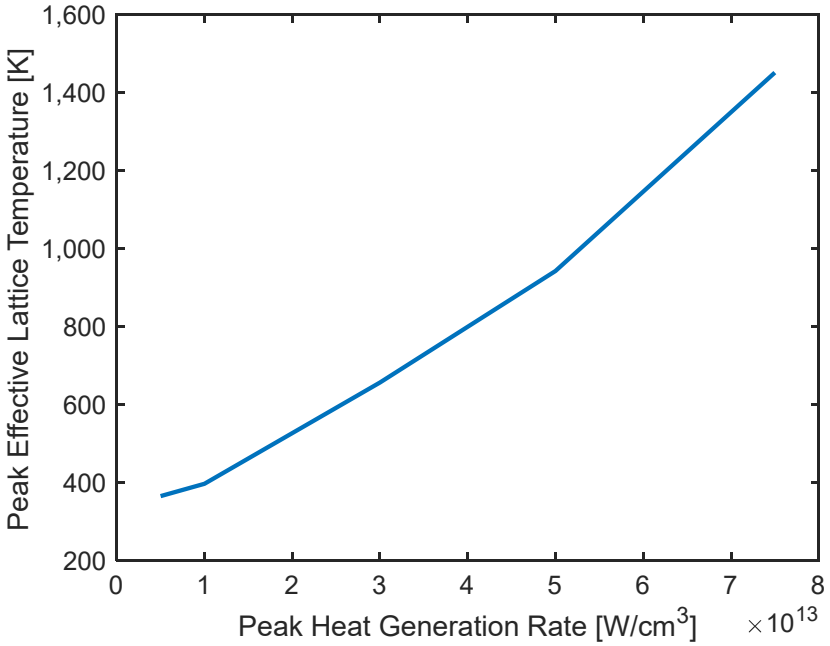

Fig. 82. Effect of peak heat generation rate on peak effective lattice temperature.

The results of Fig. 82 illustrate non-linear relationships between these two variables. In addition, effective lattice temperatures approach the melting point of silicon (1687 K) for heating rates that are achievable for these devices.

Effective lattice temperatures are important thermal design information however, they do not provide information on the local thermal conditions in regards to the phonon population and the deviation of the population from the equilibrium condition. Of particular importance is the build-up of optical phonons. Phonons of this nature have low drift velocities and preferentially scatter with higher energy electrons. Thus, they will not only impede thermal transport but impede electrical transport [73, 89]. Thus, the excess optical phonon ratio is proposed to as a measure to provide this detail. This number is the ratio of the number of optical phonons in a given geometric cell to that of the equilibrium Bose-Einstein condition at the effective local lattice temperature. The peak excess optical phonon ratio is plotted in Fig. 83 as a function of the peak heat generation rate in the transistor.

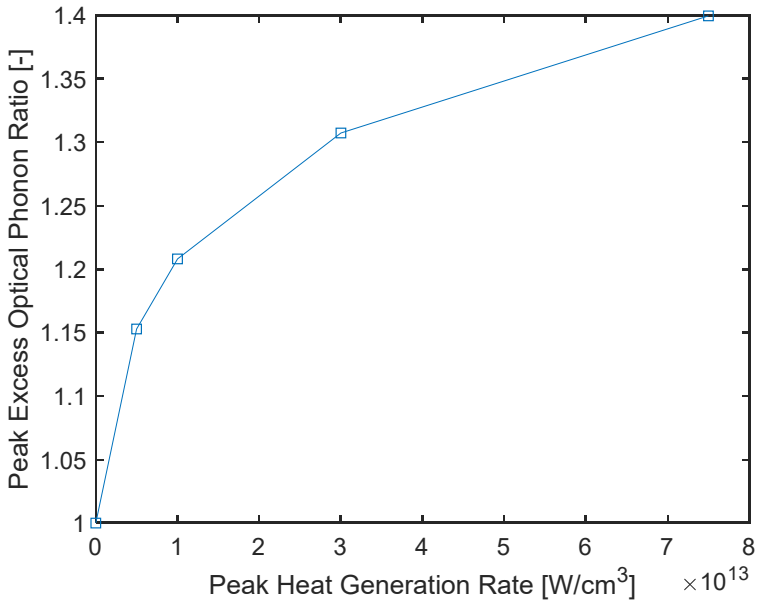

Fig. 83. Effect of peak heat generation rate on excess optical phonon ratio.

Fig. 83 above demonstrates significant deviation in the local optical phonon distribution from equilibrium at higher peak heat generation rates. Rhyner [41] illustrates that total power dissipation of 1 μW – 1.2 μW (corresponding to peak heat generation rates on the order of 1E13 W/cm^3) can reduce the ON current by up to 50% and is likely due to strong coupling between conduction electrons and optical phonons.

Relative to the time variation of thermal conditions, Fig. 84 demonstrates the transient response of the effective lattice temperature and excess optical phonon ratio for a location of 30 nm from the source of the transistor with a peak heat generation rate of 1E13 W/cm^3.

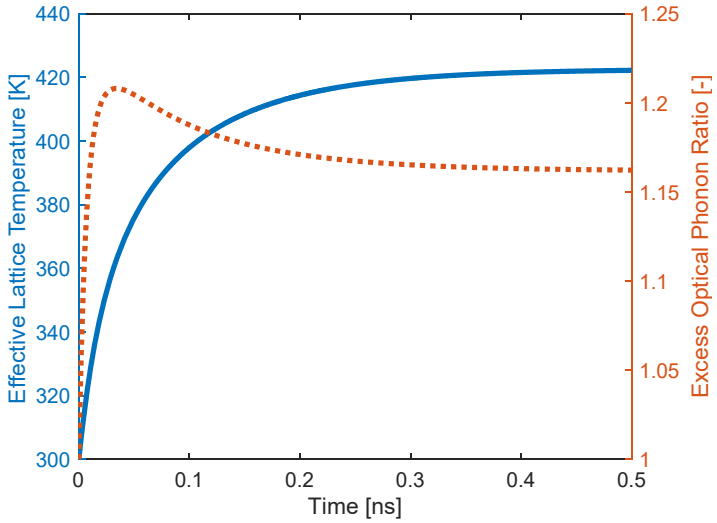

Fig. 84. Transient response of thermal conditions at an x location of 30 nm from the source in a prototypic nanowire transistor with a constant peak heat generation rate of 1E13 W/cm^3.

Fig. 84 demonstrates that the excess optical phonon ratio quickly builds up to the peak value when heat generation is initiated. This is consistent with the fact that much of the thermal energy is input to optical modes due to electron phonon scattering. The optical phonon modes never relax fully back to the equilibrium value of 1.0 even though a steady state is achieved.

The transient response to a constant heat generation rate in time provides valuable information relative to a "worst case" scenario, however; it is not representative of the ON/OFF switching of any transistor. To better represent this condition, a periodic heat generation rate with a given duty cycle was simulated. The transient response of the transistor to 10 ps period and a 50% duty cycle with a peak heat generation rate of 1E13 W/cm^3 is illustrated with Fig. 85.

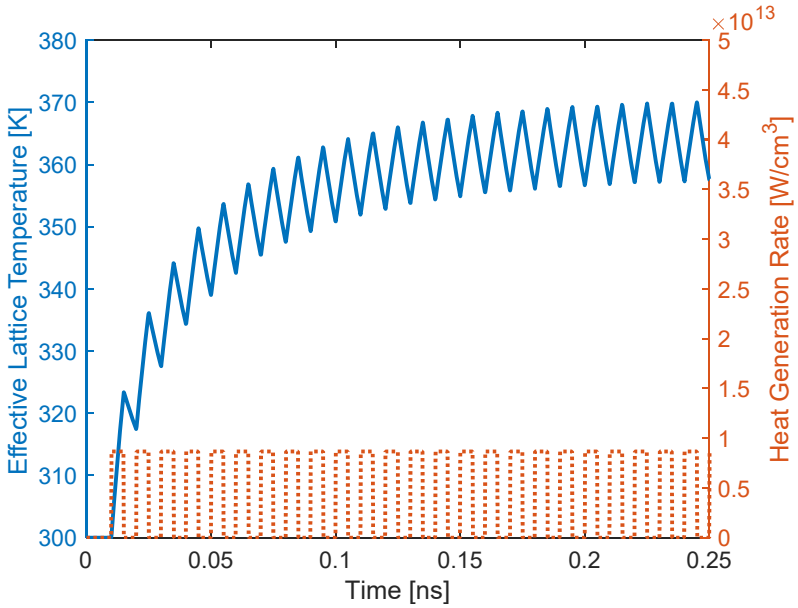

Fig. 85. Transient response of effective lattice temperature and heat generation rate at an x location of 30 nm from the source in a prototypic nanowire transistor with a period of 10 ps, 50% duty cycle, and peak heat generation rate of 1E13 W/cm^3.

Fig. 85 shows the transient response of the effective lattice temperature (left axis) at the channel/drain interface (30 nm from source) to the cyclic heat generation rate (right axis). A peak effective lattice temperature of approximately 370 K is reached during the transient and a pseudo steady state value of approximately 360 k is reached after about 0.25 ns.

Fig. 86 shows the response of the excess optical phonon ratio at the same location to the same cyclic heating rate.

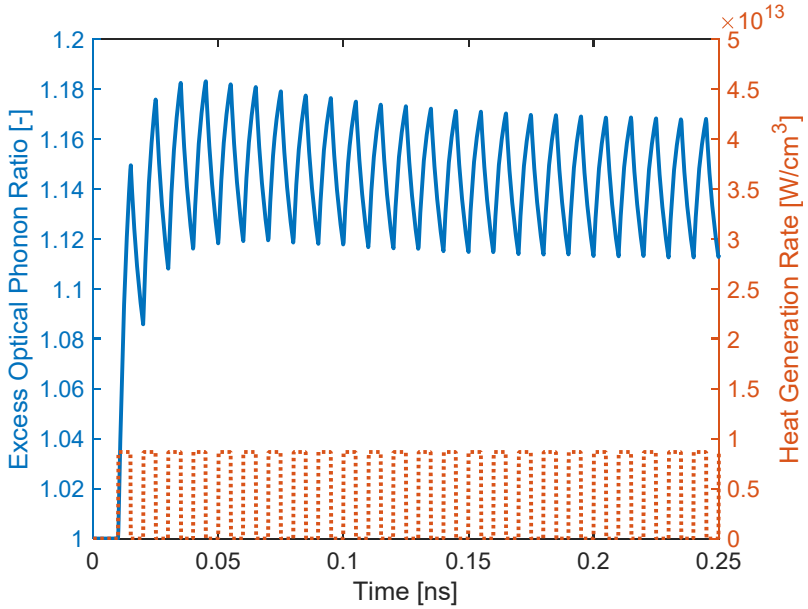

Fig. 86. Transient response of excess optical phonon ratio and heat generation rate at an x location of 30 nm from the source in a prototypic nanowire transistor with a period of 10 ps, 50% duty cycle, and peak heat generation rate of 1E13 W/cm^3.

Fig. 86 demonstrates that the excess optical phonon ratio builds up quickly to the peak value of approximately 1.18 after about 0.04 ns in the transient and decays slightly to a pseudo steady state value of approximately 1.14 after 0.25 ns. The processes of three phonon scattering and drift have a counteracting effect on the build-up of optical phonons due to heating. However, the excess optical phonon ratio doesn't decay to equilibrium at any point in the transient.

The transients can also be visualized using a six panel video shown at two snapshots in time with part a.) and part b.) of Fig. 87.

a.)

b.)

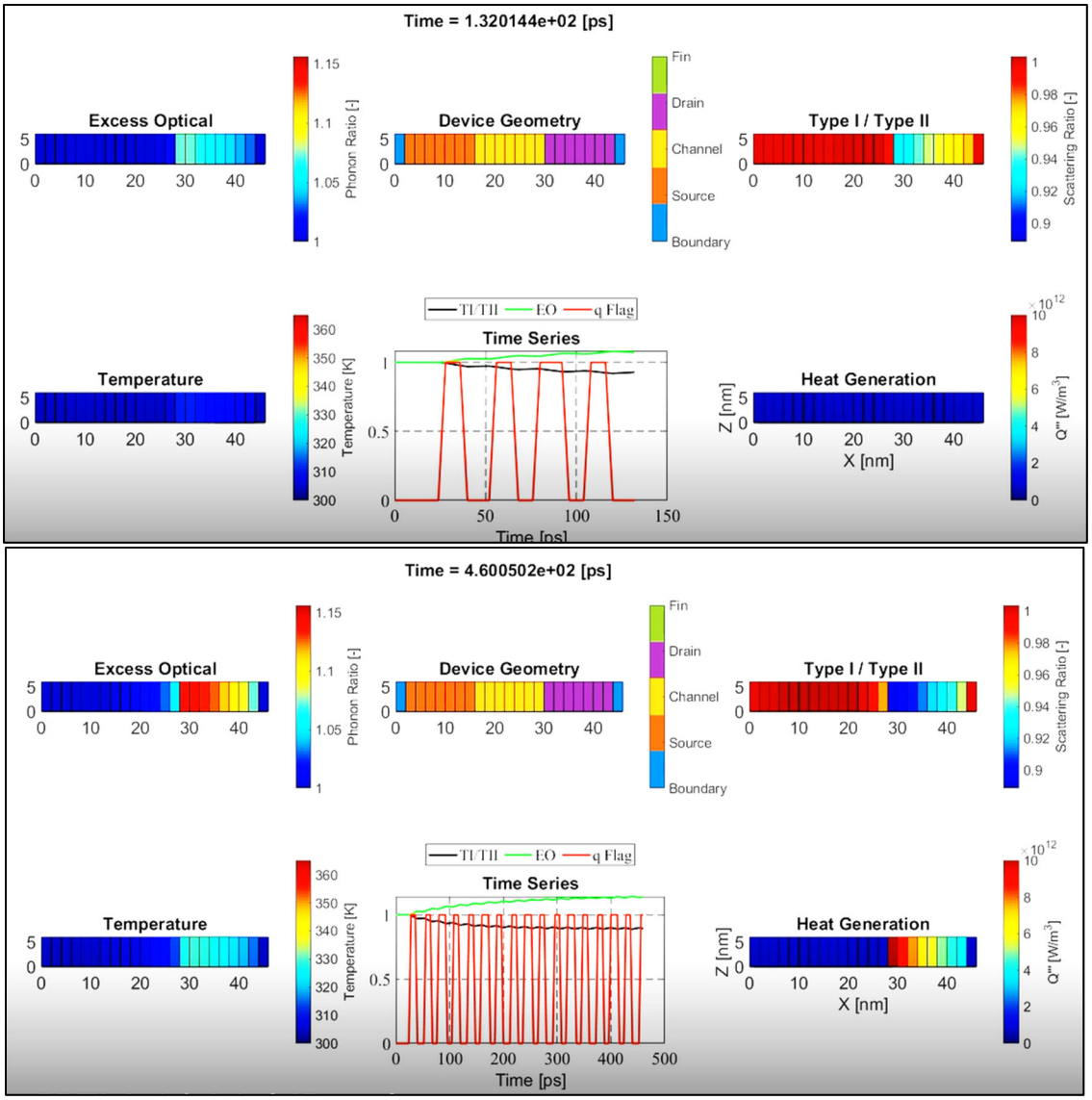

Fig. 87. Six panel movie of the transient response of silicon nanowire transistor. Part a.) shows the transient response at 132 ps and part b.) at 460 ps. Each part has six panels illustrating (from left to right) the Excess Optical, Device Geometry, Type I/Type II, Temperature, Time Series, and Heat Generation.

The top middle panel illustrates the 1-d geometry of the silicon nanowire transistor, the lower left is the heat generation rate, the lower right is the temperature, the upper left is the excess optical phonon ratio, and the upper right is the Type I/II ratio. The middle bottom section shows a strip chart with output for the heat generation rate, excess optical phonon ratio, and the Type I/II ratio. The Type I/II ratio refers to the process of three phonon scattering. As discussed in section 3.1.3, three phonon scattering involves three phonons. Two phonons can combine to produce a third with a Type I interaction or one phonon can decompose to two others in a Type II event. If a certain phonon has numbers higher than the equilibrium values, the Type II event will dominate in an effort to return the values to the equilibrium condition and the ratio will be less than 1.0. Thus, the Type I/II ratio is another measure of the non-equilibrium nature of the local conditions.

In addition to the 10 ps period and 50% duty cycle cyclic heat generation rate, other combinations of period and duty cycle were simulated. These combinations include a total of three periods (1 ps, 10 ps, and 100 ps) with three duty cycles (25%, 50%, and 75%). The maximum pseudo steady state effective lattice temperatures predicted as a function of period and duty cycle are shown in Fig. 88.

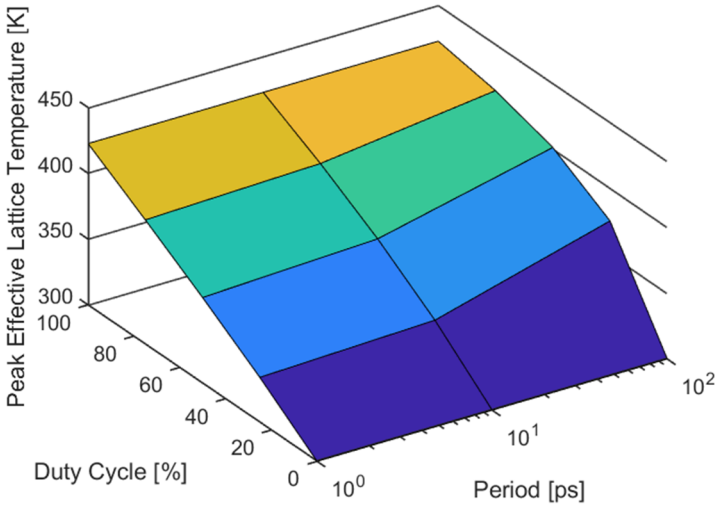

Fig. 88. Maximum pseudo steady state effective lattice temperature in a prototypic nanowire transistor as a function of period and duty cycle with a peak heat generation rate of 1E13 W/cm^3.

As is seen with the surface plot of Fig. 88, the peak effective lattice temperatures increase as the duty cycle increases and nearly reach the steady state values (100% duty cycle) even at longer periods due to the fact that the heat generation is in the ON state for longer periods of time and more thermal energy is input to the domain.

The minimum pseudo steady state excess optical phonon ratios are illustrated as a function of the three periods and three duty cycle combinations with the surface plot of Fig. 89.

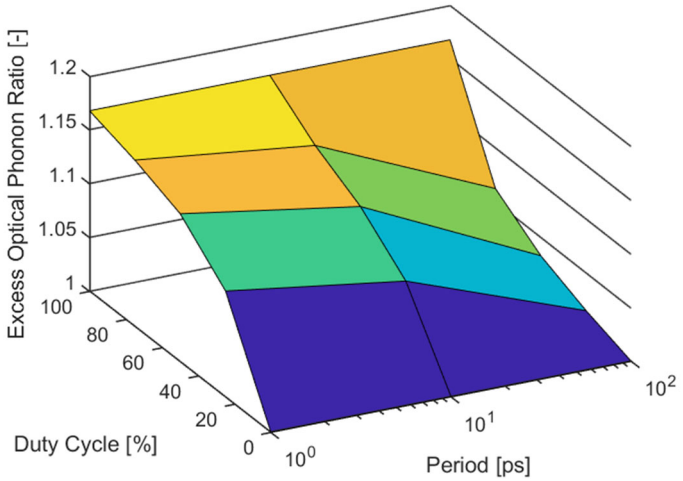

Fig. 89. Minimum pseudo steady state excess optical phonon ratio in a prototypic nanowire transistor as a function of period and duty cycle with a peak heat generation rate of 1E13 W/cm^3.

As is shown in Fig. 89, (and is evident from Fig. 86) optical phonons build up beyond the equilibrium value quickly and do not decay to equilibrium at any of the periods considered. Sinha et al [102] noted with Monte Carlo analysis that no phonon accumulation occurs for a period of 100 ps with a 30% duty cycle with a peak generation rate on the order of 5E12 W/cm^3. This work demonstrates that at a higher peak generation rate of 1E13 W/cm^3 and a shorter channel length (14 nm in this work compared to 20 nm) this is not the case. Optical phonon buildup can lead to phonon bottlenecks and reduction in electron mobility. Rhyner et al [41-43], for a steady state simulation of silicon nanowire transistors, demonstrated that the increased phonon population induced from self-heating leads to strong electron phonon coupling and an approximately 50% reduction in total current. They attributed that a portion of the reduction is due to phonons modes out of equilibrium. This effect is, in part, attributable to excess optical phonons.

Mitigation of the build-up of optical phonons and the detrimental thermal conditions could in theory be addressed with several transistor design changes. First, as the build-up occurs in the drain region, a flared drain geometry could reduce the optical phonon generation rates as the local current flux would be reduced. In addition, the phonon drift would be less confined with a larger cross sectional area. Second, the addition of specific paths for enhanced phonon drift away from the generation region could reduce this effect. These regions would act to guide optical phonons away from the drain. Third, as the build-up of optical phonons occurs from electron-phonon scattering, materials with lower scattering rates would be advantageous. Stronger interatomic bonds would lead to lower deformed potential due to the presence of phonons and thus lower coupling strength to transport electrons. The design of phonon dispersion relations with the use of confinement effects could act to eliminate modes that couple more strongly to electrons in the first place. Lastly, enhanced heat transfer to adjacent materials in the vicinity of the peak generation rates could ease the thermal conditions.

The effectiveness of the above design changes could be simulated with the enhanced SPTM or future enhancements to the SPTM. As a demonstration of this capability, the final design change involving enhanced heat transfer is simulated with this work directly as an absorptive boundary condition at a location of 28 nm from the source of the transistor. This type of boundary condition treats the cell boundaries as able to absorb some of the phonons that would be incident upon them in the timestep considered. In effect, this simulates energy transfer out of the domain to the surroundings. Reflectivity values from 1.0 to 0.7 were considered. A value of 1.0 represents the purely specular condition. The Resulting effects on the reduction in the peak effective lattice temperature are illustrated in Fig. 90.

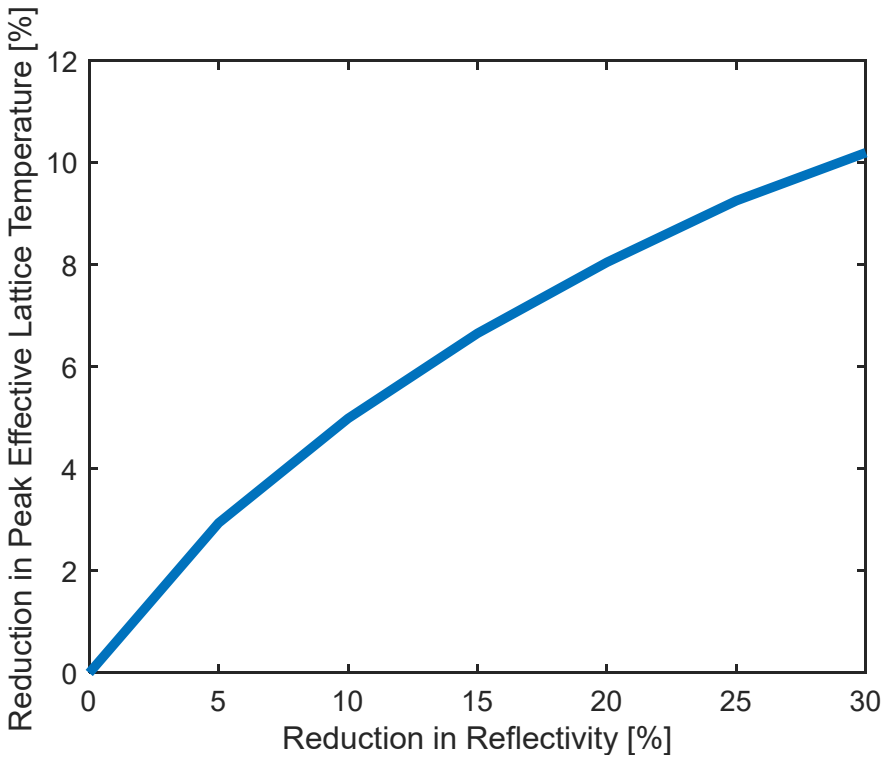

Fig. 90. Effect of reduced boundary reflectivity at an x location of 28 nm from the source in a prototypic nanowire transistor on peak effective lattice temperature for a peak heat generation rate of 1E13 W/cm^3.

As can be seen in Fig. 90, a reduction in peak effective lattice temperatures occur as a result of reduced boundary reflectivity. However, a 30% reduction in reflectivity is required for about a 10% reduction in the peak effective lattice temperature. This is a result of the fact that the majority of phonons incident on the cell boundary during the given timestep are acoustic in nature due to their higher drift velocities.

5.5.2.2 FinFET Array Transistor

The 3-d, transient simulation results for the FinFET array transistor are first shown with a case with a period of 10 ps and a duty cycle of 50%. The transient response of the effective lattice temperature at the channel to drain interface to the cyclic heating rate is illustrated in Fig. 91.

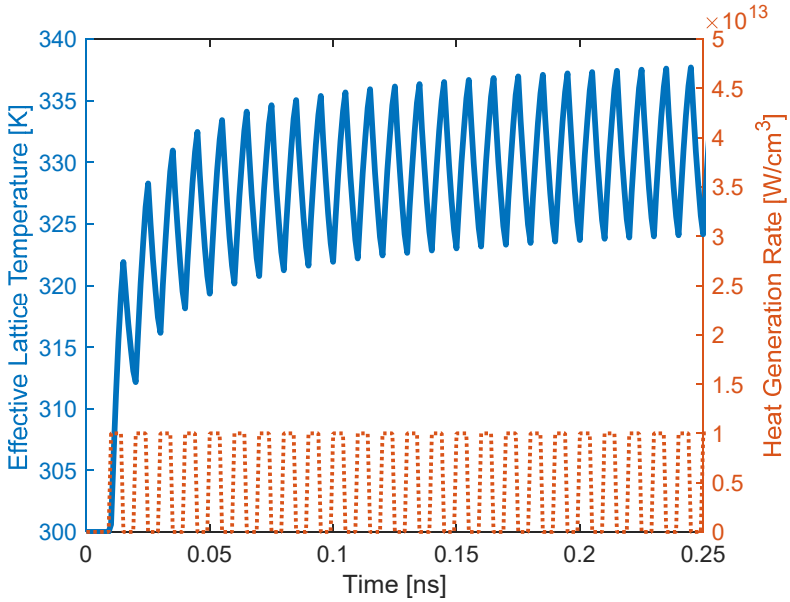

Fig. 91. Effective lattice temperature and heat generation rate as a function of time at the drain/channel interface for the 3-d, transient simulation of the FinFET geometry.

The effective lattice temperature rises relatively quickly to a pseudo steady state value after approximately 0.25 ns. The effective lattice temperature rises to a peak value of approximately 337 K.

The spatial distribution of effective lattice temperature is illustrated with Fig. 92. The distribution is shown with a cross section at the center of the simulation domain corresponding to the time of the peak effective lattice temperature. The location of the fin is illustrated with the white labeled rectangular region.

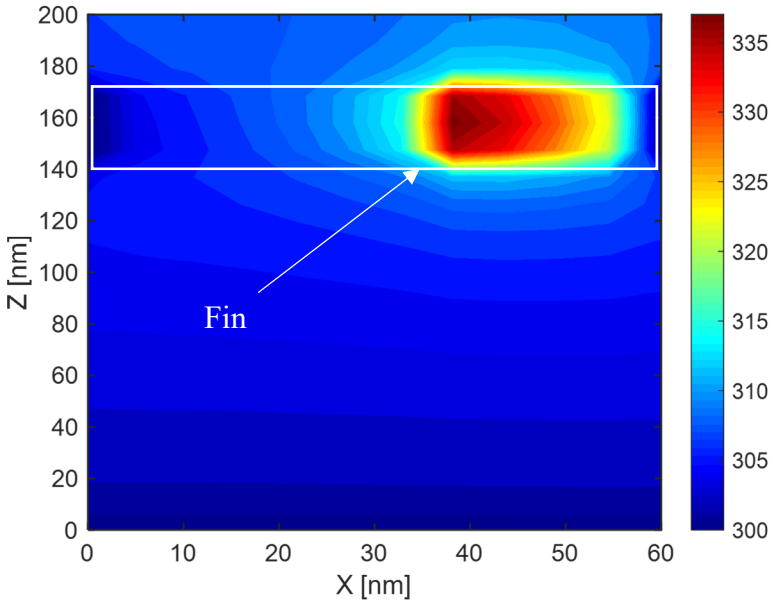

Fig. 92. Contours of effective lattice temperature in an X-Z plane at the center of the simulation domain at 0.624 ns for the 3D, transient simulation of the FinFET geometry.

Fig. 92 demonstrates the largest effective lattice temperatures occur in the regions of the highest heat generation rates and decrease more rapidly in the regions below the fin than above the fin. The overall temperature rise is modest in extent, but of more interest and insight is the change in the local thermal conditions from equilibrium. This is illustrated with the transient response of the aforementioned excess optical phonon ratio with Fig. 93.

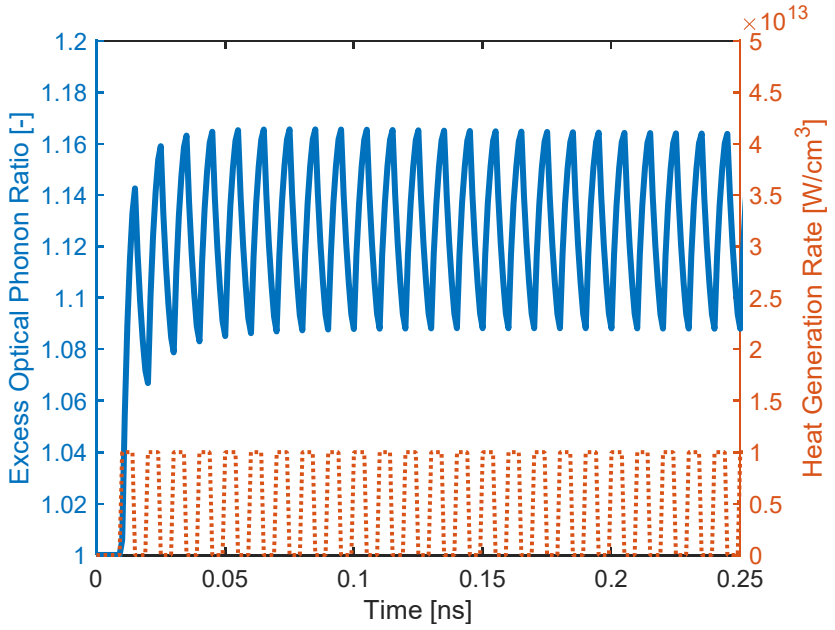

Fig. 93. Excess optical phonon ratio and heat generation rate as a function of time at the drain/channel interface for the 3D, transient simulation of the FinFET geometry with a period of 10 ps and 50% duty cycle.

The build-up of optical phonons to values beyond equilibrium occurs very quickly to a peak value of approximately 1.17 and reaches a pseudo steady state value of approximately 1.13 after only 0.1 ns. During the portion of operation where heating values are equal to zero, the number reduces to approximately 1.09 but never decays completely to the equilibrium value of 1.0. This occurs because the decay rate and drift rate of optical phonons is not sufficient to return the population to equilibrium in the time period illustrated. This indicates an excess of optical phonons remains for the duration of operation and can have consequences on reliability and operation.

The spatial distribution of excess optical phonons is illustrated with Fig. 94. The distribution is shown with a cross section at the center of the simulation domain corresponding to the time of the peak effective lattice temperature. The location of the fin is again illustrated with the white labeled rectangular region.

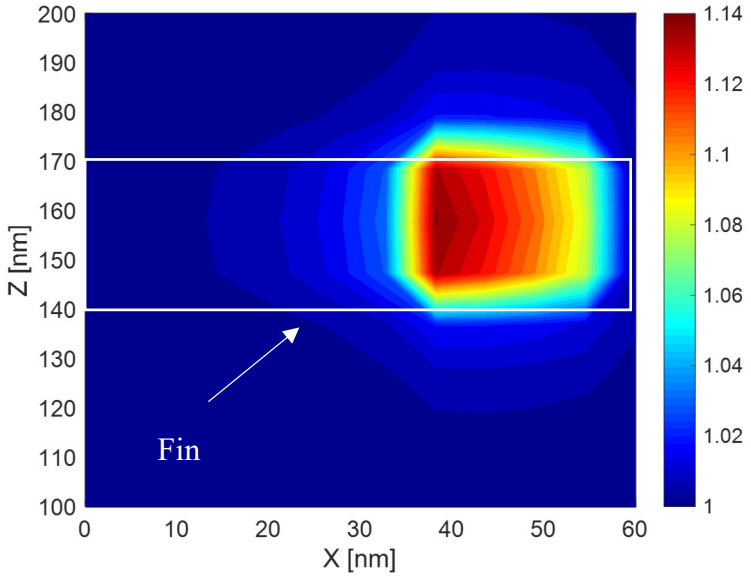

Fig. 94. Contours of excess optical phonon ratio in the X-Z plane at the center of the simulation domain at 0.052 ns for the 3D, transient simulation of the FinFET geometry with a 10 ps period and 50% duty cycle.

Fig. 94 demonstrates that optical phonons in excess of the equilibrium values persist through at least half of the geometric region representing the fin at the conditions simulated.

Two additional simulations were performed to investigate the effect of period length on thermal conditions. Periods of 50 ps and 100 ps were used with a 50% duty cycle. The transient response of the effective lattice temperature at the channel to drain interface to the cyclic heating rate is illustrated in Fig. 95.

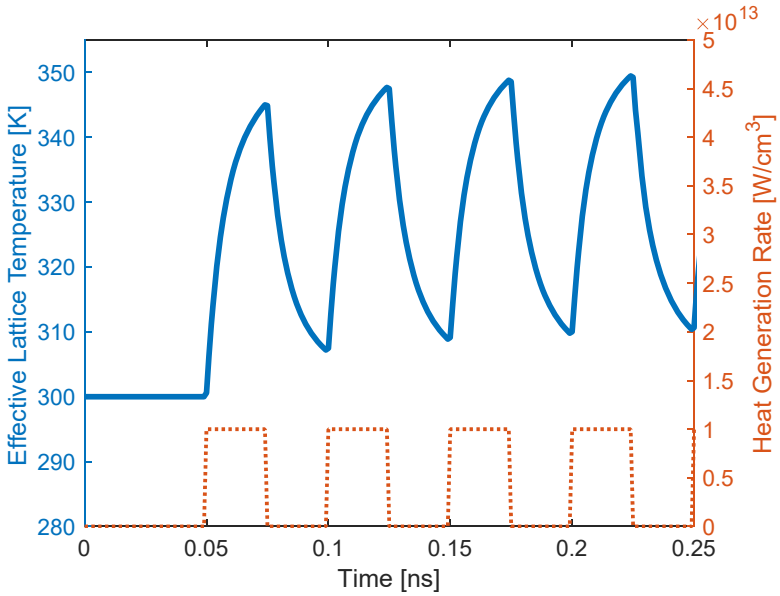

Fig. 95. Effective lattice temperature and heat generation rate as a function of time at the drain/channel interface for the 3D, transient simulation of the FinFET geometry with a period of 50 ps and duty cycle of 50%.

The results of Fig. 95 indicated that a slightly higher peak effective lattice temperature is reached during the transient. This is a result of the fact that heat generation is occurring for a longer time during the "ON" state of the transistor. The excess optical phonon dynamics are illustrated with Fig. 96 for the same scenario.

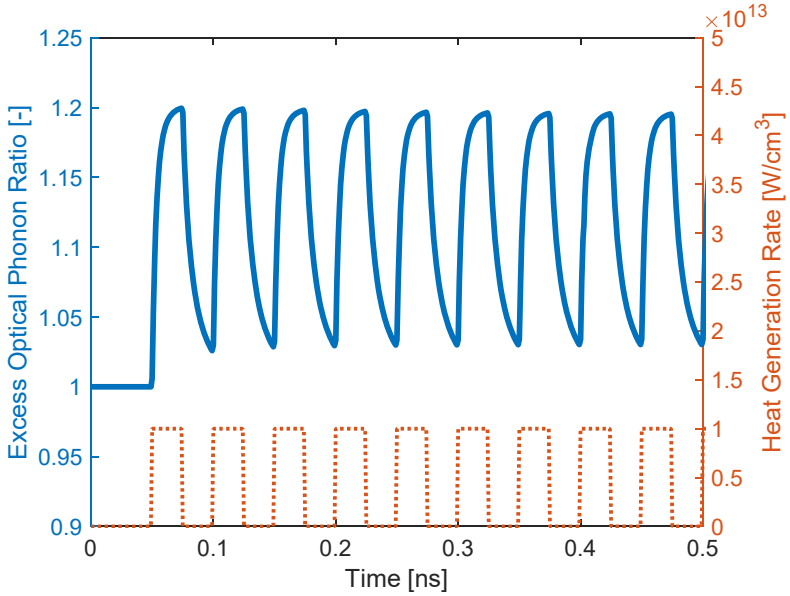

Fig. 96. Excess optical phonon ratio and heat generation rate as a function of time at the drain/channel interface for the 3D, transient simulation of the FinFET geometry with a period of 50 ps and 50% duty cycle.

As is seen in Fig. 96, the excess optical phonon ratio reaches a higher peak value of approximately 1.2 when compared to the case of a 10 ps period with a value of approximately 1.17. After approximately 10 ps of heating in any given "ON" cycle, the rate at which the excess optical phonon ratio increases begins to decrease or flatten. This indicates that at these beyond equilibrium values, the rate of three phonon scattering for the optical modes begins to counteract the effect of optical phonon generation thus limiting the peak values. It is still noted that the excess optical phonon ratio doesn't decay to the equilibrium value for the duration of the cycling events.

Similar results for a period of 100 ps are illustrated with Fig. 97 and 98.

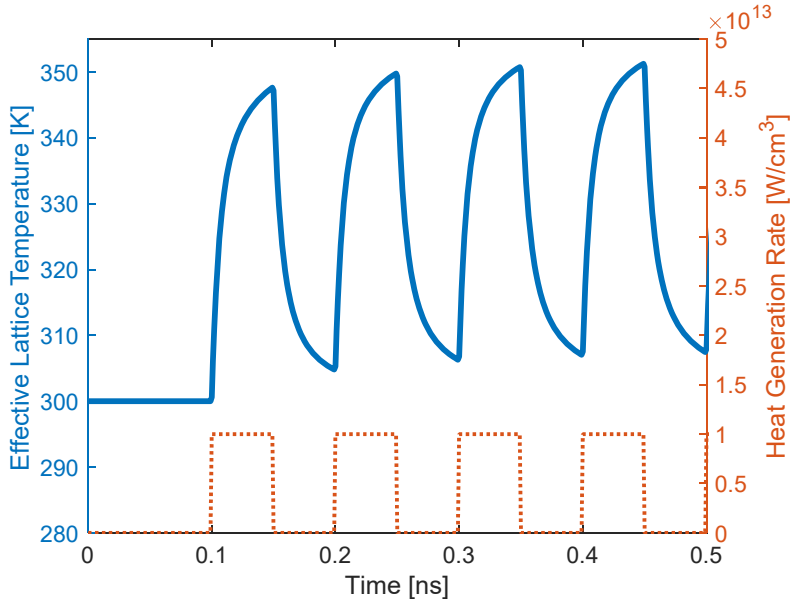

Fig. 97. Effective lattice temperature and heat generation rate as a function of time at the drain/channel interface for the 3D, transient simulation of the FinFET geometry with a period of 100 ps and duty cycle of 50%.

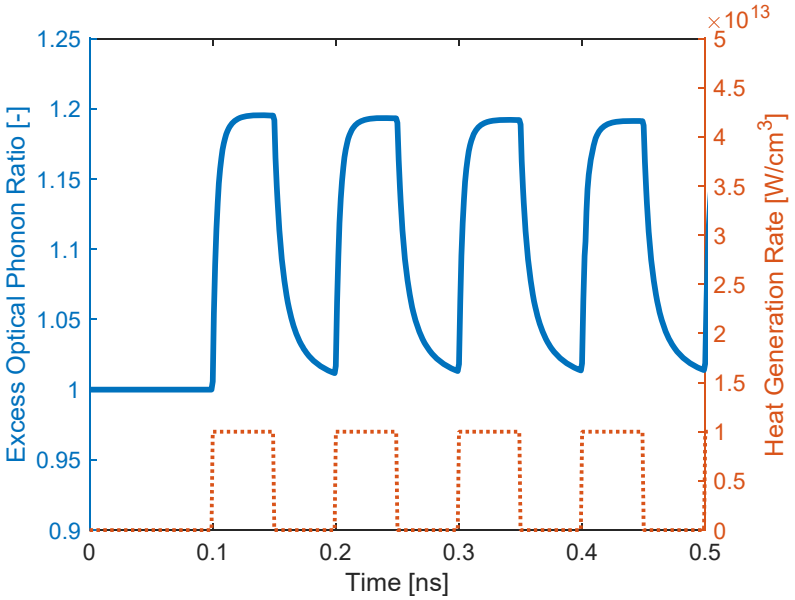

Fig. 98. Excess optical phonon ratio and heat generation rate as a function of time at the drain/channel interface for the 3D, transient simulation of the FinFET geometry with a period of 100 ps and 50% duty cycle.

The results of Fig. 98 illustrate that a steady state value of the excess optical phonon ratio is reached after approximately 25 ps of heat generation occurring in any given cycle. Thus, for this geometry and peak generation rate, a maximum excess optical phonon ratio is observed to be approximately 20%.

The effect of the size of the unheated region surrounding the fin was investigated illustrating the effect of fin to fin spacing on the thermal conditions. Results of effective lattice temperature and

excess optical phonon ratio for the three different conditions simulated are shown with Fig. 99 and 100 respectively.

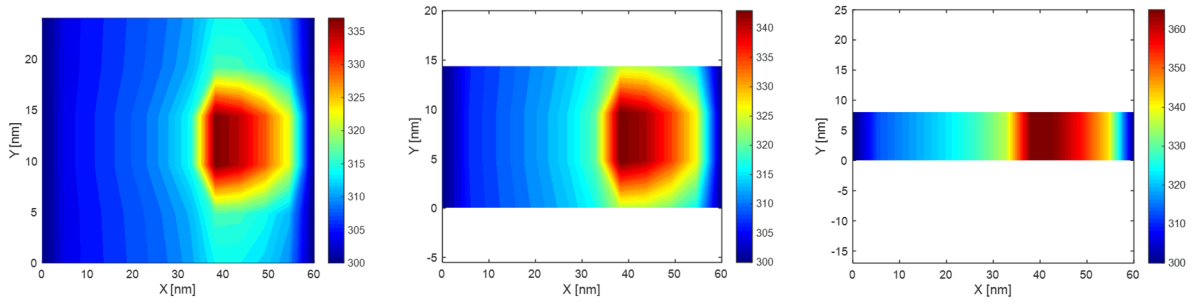

a) 8 nm gap b) 4 nm gap c) 0 nm gap

Fig. 99. Contours of effective lattice temperature in the X-Y plane at the center of the simulation domain at the time of peak effective lattice temperature for the 3D, transient simulation of the FinFET geometry with a 10 ps period and 50% duty cycle. Panel a. is with an 8 nm region on either side of the fin at 0.624 ns, panel b. is with 4 nm, and panel c. is with 0 nm at 0.994 ns.

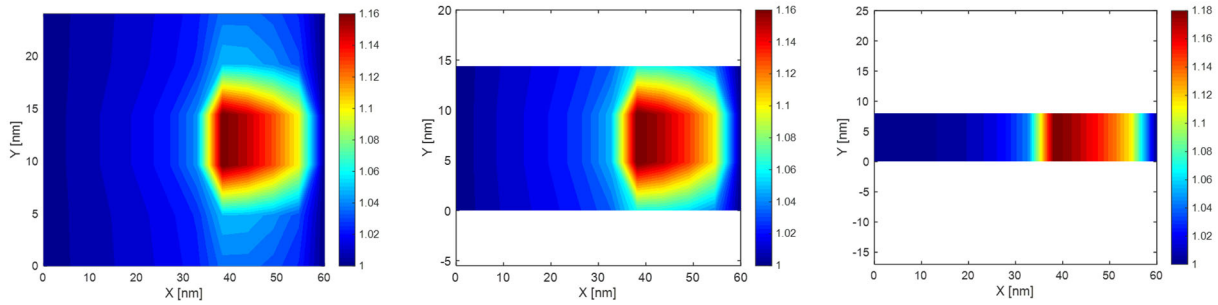

a) 8 nm gap b) 4 nm gap c) 0 nm gap

Fig. 100. Contours of excess optical phonon ratio in the X-Y plane at the center of the simulation domain for the 3D, transient simulation of the FinFET geometry with a 10 ps period and 50% duty cycle. Panel a. is with an 8 nm region on either side of the fin at 0.624 ns, panel b. is with 4 nm, and panel c. is with 0 nm at 0.034 ns.

As physically expected, as the geometry becomes more confined peak effective lattice temperatures increase. However, the excess optical phonon ratio is only slightly increased by reducing the unheated region surrounding the fin until the fin is completely confined. This peak excess optical phonon ratio occurs early in the heating cycle as the rate at which optical phonons are input to the domain is greater than the rate at which they are either transported away or decompose into other modes. As such, geometry of the unheated region has a lesser effect on this phenomena. When the fin is completely confined, the optical phonons build up to a slightly higher level as there is only one geometric direction for phonon drift to occur.

6 Summary, Conclusions, and Future Work

6.1 Summary

The work presented in this dissertation has been motivated by the following research question:

Is it possible to conduct high-fidelity, 3-d, phonon transport simulations of nanoscale electronic devices operating under transient switching conditions which reflect the non-equilibrium thermal phenomena associated with electron-phonon scattering induced heat generation?

This research question was addressed through enhancements to the physical models and computational algorithms of the Statistical Phonon Transport Model (SPTM) and subsequent application to current and emergent nanoscale transistor devices. Four major individual model enhancements were incorporated into the SPTM. These included improvements to the physical representation of the most important physical phenomenon, namely, phonon dispersion, three phonon scattering, phonon drift, and phonon generation to represent the effect of electron-phonon scattering.

First, the lattice dynamics calculation of phonon dispersion relations was extended to use first and second nearest neighbor interactions, based on published interatomic force constants computed with first principles Density Functional Theory (DFT). The use of first and second nearest neighbor lattice dynamics better predicted dispersion when compared to experimental results and resulted in a higher fidelity representation of phonon group velocities and three phonon scattering partners in an anisotropic manner.

Second, the computation of three phonon scattering partners (that explicitly conserve energy and momentum) with the inclusion of the three optical phonon branches was applied using scattering rates computed from Fermi's Golden Rule. The scattering strength for a given interaction was represented with the use of a modified Gruneisen parameter. This resulted in enhanced fidelity in the prediction of phonon modal decay rates across the wavevector space and thus better representation of non-equilibrium behavior.

Third, the prediction of phonon drift was extended to three dimensions within the framework of the previously established methods of the SPTM. This allowed for the representation of the transport of phonons to different geometric regions with an accounting for all phonons in the domain and thus a more realistic representation of phonon dynamics in nanoscale electronic devices.

And fourth, Joule heating as a result of electron-phonon scattering in nanoscale electronic devices was represented using a modal specific phonon source. The phonon source differed within the computation cells of the geometric domain and was cycled on and off at periods ranging from 1 ps – 100 ps with a 50% duty cycle. This model enhancement produced a phonon source that represented the preferential generation of phonons over the wavevector space, the typical spatial variation in heat generation as a result of carrier movement from the source to the drain of transistors, and the transient switching of transistor devices.

The individual model enhancements were verified and validated against theoretical or physically expected behavior. The SPTM was compared to representative simulations from literature that span the range of device modeling methods/approaches for nanoscale thermal transport. The results indicated that fidelity and flexibility. The SPTM was applied to both a 1-d silicon nanowire transistor and a 3-d FinFET array transistor in a transient manner. The results illustrated the design capability of the SPTM.

6.2 Conclusions

The SPTM has been elevated to fill the gap between lower phonon fidelity Monte Carol (MC) models and high fidelity, inflexible direct quantum simulations (or Direct Atomic Simulations (DAS)) within the field of phonon transport modeling for nanoscale electronic devices. Within this overall contribution to the field of research, several novel individual items can be identified. These include the following:

- Representation of the entire phonon population in drift and scattering events.
- Heat generation algorithm that represents the effect of joule heating without the direct calculation of electron-phonon scattering rates.
- Transient switching to investigate the effect of period and duty cycle on local phonon conditions
- Ability to model devices across the range of dimensions from 1-d to 2-d to 3-d.
- Introduction of valuable metrics that describe the non-equilibrium nature of local thermal conditions including the excess optical phonon ratio and Type I/II ratio.

The SPTM has produced high fidelity device level non-equilibrium phonon information in a 3-d, transient manner. This information is required due to the fact that effective lattice temperatures are not adequate to describe the local thermal conditions. Knowledge of local phonon distributions, which can't be determined from application of Fourier's law, is important because of effects on electron mobility, device speed, leakage, and reliability.

6.3 Recommendations for Future Work

The work presented in this dissertation illustrates significant enhancements to the SPTM; however, a number of additional extensions can be suggested for future work. The comparison of the SPTM to the range of modeling approaches available from literature has illuminated a gap in the area of full fidelity electrical transport modeling and the coupling of this transport to the thermal conditions with full fidelity electron-phonon interactions. This can be represented with the following research question:

Can high fidelity, 3-d, transient simulations of nanoscale electronic devices be performed with fully coupled, full fidelity electron and phonon transport to predict the effect of design parameters such as dopant, voltage biases, geometry, and enhanced heat transfer on device performance and reliability, specifically drain current, maximum switching speed, and thermal failure?

The initial extensions of the SPTM beyond this dissertation should focus on answering the above research question. Additional proposed future work can continue to enhance the fidelity, flexibility, and/or computationally efficiency of the model. These might include (but are not limited to) the following items.

- Fidelity
    - Three phonon scattering enhancements
        - The current calculation of the three phonon scattering strength uses a single Gruneisen-like parameter that was adjusted to reproduce the thermal conductivity of silicon at 277 K. Despite this fact, there is evidence that the effect of three phonon scattering could be enhanced further. This could include a mode specific Gruneisen-like parameter to

lead to better predictions of the MMRT and therefore thermal conductivities over the applicable temperature range.

- Impurity scattering
  - Nanoscale electronic devices primarily consist of regions of doped silicon placed together to form junctions. The addition of these impurity atoms to the silicon lattice effect phonon transport and should be included for a higher fidelity simulation.
- Additional materials with interface transmission and scattering
  - The SPTM is currently able to model phonon transport in silicon. Current and emergent nanoscale electronic devices consist of regions of doped silicon surrounded by insulating oxide materials and a conductive gate. Higher fidelity modeling would be obtained with inclusion of phonon transport within and between these different material regions.
- Phonon confinement and coherent effects
  - The quasi-particle based phonon transport modeling of the SPTM is directly applicable above length scales where phonon wavepackets can be treated as separate entities that interact with scattering events. As characteristic length scales become even smaller, wave effects due to interference can have a significant effect on phonon transport and would need to be accounted for.
- Enhanced boundary conditions, namely diffuse boundary scattering
  - As geometric length scales are reduced, boundary scattering will impede phonon transport due to the diffuse nature of this event. Currently, boundary scattering is treated as purely specular so fidelity will be improved by incorporating this phenomenon.

- Flexibility
  - Non-linear Cartesian cells with variable cell dimensions will allow for more accurate representation of geometries.
  - Non-Cartesian coordinates will allow for better representation of cylindrical geometries such as those of silicon nanowire devices.
  - Multi-scale modeling could allow for the merger of local phonon transport models with larger scale models of groups of transistors where Fourier's law is appropriate.
- Computational Efficiency
  - Algorithm enhancements for increased speed
  - Expand parallelism from one node and multiple CPU's to multiple nodes/CPU's to take advantage of larger computing clusters.

The improvements of the SPTM made in this dissertation and suggested with the future work will contribute to enhanced nanoscale device designs and better understanding of local thermal conditions. It is the hope of the author that this will lead to the betterment of society and the enhancement of the world at least in some small way.

7 References

[1] Huang, W., Allen-Ware, M., Carter, J. B., Cheng, E., Skadron, K., and Stan, M. R., 2011, "Temperature-Aware Architecture: Lessons and Opportunities," IEEE Micro, 31(3), pp. 82-86.
[2] Iranfar, A., Kamal, M., Afzali-Kusha, A., Pedram, M., and Atienza, D., "Thespot: Thermal Stress-Aware Power and Temperature Management for Multiprocessor Systems-on-Chip," IEEE Transactions on Computer-Aided Design of Integrated Circuits and Systems, PP(99), pp. 1-1.
[3] Danowitz, A., Kelley, K., Mao, J., Stevenson, J., and Horowitz, M., 2012, "Cpu Db: Recording Microprocessor History," ACM.
[4] Ieee, 2017, "International Roadmap for Devices and Systems Executive Summary."
[5] Moore, G. E., 1998, "Cramming More Components onto Integrated Circuits," Proceedings of the IEEE, 86(1), pp. 82-85.
[6] Mack, C. A., 2011, "Fifty Years of Moore's Law," IEEE Transactions on Semiconductor Manufacturing, 24(2), pp. 202-207.
[7] Rupp, K., 42 Years of Microprocessor Trend Data, https://www.karlrupp.net/2018/02/42-years-of-microprocessor-trend-data/
[8] Itrs, 2014, "The International Technology Roadmap for Semiconductors (Itrs), Itrs 2.0 System Integration Whitepaper."
[9] Brown Iii, T. W., 2012, "A Statistical Phonon Transport Model for Thermal Transport in Crystalline Materials from the Diffuse to Ballistic Regime," Doctor of Philosophy Rochester Institute of Technology, Rochester, NY.
[10] Brown, T. W., and Hensel, E., 2012, "Statistical Phonon Transport Model for Multiscale Simulation of Thermal Transport in Silicon: Part I – Presentation of the Model," International Journal of Heat and Mass Transfer, 55(25-26), pp. 7444-7452.
[11] Brown, T. W., and Hensel, E., 2012, "Statistical Phonon Transport Model for Multiscale Simulation of Thermal Transport in Silicon: Part Ii – Model Verification and Validation," International Journal of Heat and Mass Transfer, 55(25-26), pp. 7453-7459.
[12] Korec, J., 2011, Low Voltage Power Mosfets: Design, Performance and Applications, Springer New York, New York, NY.
[13] Bhoir, M. S., and Mohapatra, N. R., "Impact of Box Thickness and Ground-Plane on Non-Linearity of Utbb Fd-Soi Mos Transistors," pp. 1-4.
[14] Incropera, F. P., and Dewitt, D. P., 1996, Fundamentals of Heat and Mass Transfer, Wiley, New York.
[15] Hahn, D. W., ÖZłşŁk, M. N., and Proquest, 2012, Heat Conduction, Wiley, Hoboken, N.J.
[16] Pop, E., Dutton, R., and Goodson, K., 2005, "Monte Carlo Simulation of Joule Heating in Bulk and Strained Silicon," Applied Physics Letters, 86(8), pp. 082101-082101-3.
[17] Crank, J., 1979, The Mathematics of Diffusion, Clarendon Press, Oxford.
[18] Carslaw, H. S., 1947, Conduction of Heat in Solids, England;United Kingdom
[19] Hensel, E., 1991, Inverse Theory and Applications for Engineers, United States.
[20] Fox, R. W., and Mcdonald, A. T., 1998, Introduction to Fluid Mechanics, John Wiley, New York.
[21] D., A.-J.-. 1995, Computational Fluid Dynamics : The Basics with Applications.
[22] Modest, M. F., 2013, Radiative Heat Transfer, Elsevier Science, San Diego.
[23] Chang, C. W., Okawa, D., Garcia, H., Majumdar, A., and Zettl, A., 2008, "Breakdown of Fourier's Law in Nanotube Thermal Conductors," Physical Review Letters.
[24] Yang, N., Zhang, G., and Li, B., 2010, "Violation of Fourier's Law and Anomalous Heat Diffusion in Silicon Nanowires," Nano Today.
[25] Hsiao, T.-K., Huang, B.-W., Chang, H.-K., Liou, S.-C., Chu, M.-W., Lee, S.-C., and Chang, C.-W., 2015, "Micron-Scale Ballistic Thermal Conductivity and Suppressed Thermal Conductivity in Heterogeneously Interfaced Nanowires," Physical Review B.

[26] Chen, G., 2005, Nanoscale Energy Transport and Conversion : A Parallel Treatment of Electrons, Molecules, Phonons, and Photons, England;United Kingdom;.
[27] Shinde, S. L., and Srivastava, G. P., 2014, Length Scale Dependent Phonon Interactions, Springer Science + Business Media, New York.
[28] Corporation, I., 1990, I486 Processor Hardware Reference Manual, United States.
[29] Sholl, D., and Steckel, J. A., 2009, Density Functional Theory: A Practical Introduction, Wiley-Interscience, Hoboken.
[30] Stillinger, F. H., and Weber, T. A., 1985, "Computer Simulation of Local Order in Condensed Phases of Silicon," Physical review. B, Condensed matter, 31(8), pp. 5262-5271.
[31] Tersoff, J., 1988, "Empirical Interatomic Potential for Silicon with Improved Elastic Properties," Physical review. B, Condensed matter, 38(14), pp. 9902-9905.
[32] Tewary, V. K., 2011, "Phenomenological Interatomic Potentials for Silicon, Germanium and Their Binary Alloy," Physics Letters A, 375(43), pp. 3811-3816.
[33] Bazant, M. Z., Kaxiras, E., and Justo, J. F., 1997, "Environment-Dependent Interatomic Potential for Bulk Silicon," Physical Review B, 56(14), pp. 8542-8552.
[34] Esfarjani, K., and Stokes, H. T., 2008, "Method to Extract Anharmonic Force Constants from First Principles Calculations," Physical Review B, 77(14).
[35] Romero, N. A., Nakano, A., Riley, K. M., Shimojo, F., Kalia, R. K., Vashishta, P., and Messina, P. C., 2015, "Quantum Molecular Dynamics in the Post-Petaflops Era," Computer, 48(11), pp. 33-41.
[36] Proshchenko, V. S., Dholabhai, P. P., Sterling, T. C., and Neogi, S., 2019, "Heat and Charge Transport in Bulk Semiconductors with Interstitial Defects," Physical Review B, 99(1).
[37] Meem, A. U. H., Chowdhury, O., and Morshed, A. K. M. M., 2018, "Effect of Vacancy Defects on Thermal Conductivity of Silicon Nanowire: A Molecular Dynamics Study," AIP Conference Proceedings, 1980(1).
[38] Sun, L., and Murthy, J. Y., 2010, "Molecular Dynamics Simulation of Phonon Scattering at Silicon/Germanium Interfaces," Journal of Heat Transfer, 132(10), pp. 102403.
[39] Fan, Z., Pereira, L. F. C., Wang, H.-Q., Zheng, J.-C., Donadio, D., and Harju, A., 2015, "Force and Heat Current Formulas for Many-Body Potentials in Molecular Dynamics Simulations with Applications to Thermal Conductivity Calculations," Physical Review B, 92(9).
[40] Suzuki, A., Watanabe, T., Kamakura, Y., and Kamioka, T., "Full-Scale Whole Device Emc/Md Simulation of Si Nanowire Transistor Including Source and Drain Regions by Utilizing Graphic Processing Units," pp. 357-360.
[41] Rhyner, R., and Luisier, M., 2014, "Atomistic Modeling of Coupled Electron-Phonon Transport in Nanowire Transistors," Physical review. B, Condensed matter and materials physics, 89(23).
[42] Rhyner, R., and Luisier, M., 2016, "Minimizing Self-Heating and Heat Dissipation in Ultrascaled Nanowire Transistors," Nano letters, 16(2), pp. 1022-1026.
[43] Rhyner, R., and Luisier, M., 2017, "Influence of Thermal Losses at the Gate Contact of Si Nanowire Transistors: A Phenomenological Treatment in Quantum Transport Theory," Applied physics letters, 110(10), pp. 103508.
[44] Peterson, R. B., 1994, "Direct Simulation of Phonon-Mediated Heat Transfer in a Debye Crystal," Journal of Heat Transfer, 116(4), pp. 815.
[45] Peterson, R. B., 1994, "Direct Simulation of Phonon-Mediated Heat-Transfer in a Debye Crystal," JOURNAL OF HEAT TRANSFER-TRANSACTIONS OF THE ASME, 116(4), pp. 815-822.
[46] Mazumder, S., and Majumdar, A., 2001, "Monte Carlo Study of Phonon Transport in Solid Thin Films Including Dispersion and Polarization," JOURNAL OF HEAT TRANSFER-TRANSACTIONS OF THE ASME, 123(4), pp. 749-759.

[47] Mittal, A., and Mazumder, S., 2010, "Monte Carlo Study of Phonon Heat Conduction in Silicon Thin Films Including Contributions of Optical Phonons," JOURNAL OF HEAT TRANSFER-TRANSACTIONS OF THE ASME, 132(5), pp. 52402.
[48] Kukita, K., and Kamakura, Y., 2013, "Monte Carlo Simulation of Phonon Transport in Silicon Including a Realistic Dispersion Relation," JOURNAL OF APPLIED PHYSICS, 114(15), pp. 154312.
[49] Wu, R., Hu, R., and Luo, X., 2016, "First-Principle-Based Full-Dispersion Monte Carlo Simulation of the Anisotropic Phonon Transport in the Wurtzite Gan Thin Film," Journal of Applied Physics, 119(14), pp. 145706.
[50] Klemens, P. G., 1958, Elsevier Science & Technology.
[51] Holland, M. G., 1963, "Analysis of Lattice Thermal Conductivity," Physical Review, 132(6), pp. 2461-2471.
[52] Ziman, J. M., 1960, Electrons and Phonons, Oxford, Great Britain.
[53] Reissland, J. A., 1973, The Physics of Phonons, Wiley, London;New York;.
[54] Srivastava, G. P., The Physics of Phonons.
[55] Han, Y., and Klemens, P. G., 1993, "Anharmonic Thermal Resistivity of Dielectric Crystals at Low Temperatures," Physical review. B, Condensed matter, 48(9), pp. 6033-6042.
[56] Wang, T., and Murthy, J. Y., 2006, "Solution of the Phonon Boltzmann Transport Equation Employing Rigorous Implementation of Phonon Conservation Rules," Proc. ASME International Mechanical Engineering Congress and Exposition, Chicago, Illinois, USA.
[57] Esfarjani, K., Chen, G., and Stokes, H. T., 2011, "Heat Transport in Silicon from First-Principles Calculations," Physical Review B, pp. 11.
[58] Narumanchi, S. V. J., Murthy, J. Y., and Amon, C. H., 2004, "Submicron Heat Transport Model in Silicon Accounting for Phonon Dispersion and Polarization," Journal of Heat Transfer, 126(6), pp. 946.
[59] Ward, A., and Broido, D. A., 2010, "Intrinsic Phonon Relaxation Times from First-Principles Studies of the Thermal Conductivities of Si and Ge," Physical Review B.
[60] Pascual-Gutiérrez, J. A., Murthy, J. Y., and Viskonta, R., 2009, "Thermal Conductivity and Phonon Transport Properties of Silicon Using Perturbation," Journal of Applied Physics 106.
[61] Sabatti, F. F. M., Goodnick, S. M., and Saraniti, M., 2017, "Simulation of Phonon Transport in Semiconductors Using a Population-Dependent Many-Body Cellular Monte Carlo Approach," Journal of Heat Transfer, 139(3), pp. 032002-032002-10.
[62] Li, W., Carrete, J., A. Katcho, N., and Mingo, N., 2014, "Shengbte: A Solver of the Boltzmann Transport Equation for Phonons," Computer Physics Communications, 185(6), pp. 1747-1758.
[63] Kukita, K., Adisusilo, I. N., and Kamakura, Y., 2014, "Monte Carlo Simulation of Diffusive-to-Ballistic Transition in Phonon Transport," Journal of Computational Electronics, 13(1), pp. 264-270.
[64] Nur Adisusilo, I., Kukita, K., and Kamakura, Y., "Analysis of Heat Conduction Property in Finfets Using Phonon Monte Carlo Simulation," pp. 17-20.
[65] Plimpton, S., 1995, "Fast Parallel Algorithms for Short-Range Molecular Dynamics," Journal of Computational Physics, 117(1), pp. 1-19.
[66] Pascual-Gutierrez, J. A., 2010, "On the Theory of Phonons: A Journey from Their Origins to the Intricate Mechanisms of Their Transport," ProQuest Dissertations Publishing.
[67] Sakurai, J. J., and Napolitano, J., Modern Quantum Mechanics.
[68] Kittel, C., Introduction to Solid State Physics, 8th Edition.
[69] Simon, S. H., 2013, The Oxford Solid State Basics, Oxford University Press, Oxford.
[70] Nelin, G., and Nilsson, G., 1972, "Phonon Density of States in Germanium at 80 K Measured by Neutron Spectrometry," Physical Review B, 5(8), pp. 3151-3160.
[71] Dolling, G., and Cowley, A., 1966, "The Thermodynamic and Optical Properties of Germanium, Silicon, Diamond and Gallium Arsenide.," Proc. Proc. Phys. Soc. London.

[72] Xie, J. C., Xie, R.-H., Mishra, S. K., and Kar, T., 2014, "Generalized Interatomic Pair-Potential Function," Chemical Physics Letters, 605-606(pp. 137-146.
[73] Rowlette, J. A., and Goodson, K. E., 2008, "Fully Coupled Nonequilibirum Electron-Phonon Transport in Nanometer-Scale Silicon Fets," IEEE Transactions on Electron Devices, 55(1).
[74] Yu, P. Y., and Cardona, M., 2010, Fundamentals of Semiconductors: Physics and Materials Properties, Springer.
[75] Carruthers, P., 1961, "Theory of Thermal Conductivity of Solids at Low Temperatures," Reviews of Modern Physics, 33(1), pp. 92-138.
[76] Luo, T., and Chen, G., 2013, "Nanoscale Heat Transfer - from Computation to Experiment," PHYSICAL CHEMISTRY CHEMICAL PHYSICS, 15(1), pp. 3389-3412.
[77] Herman, F., 1959, "Lattice Vibrational Spectrum of Germanium," Journal of Physics and Chemistry of Solids, 8(pp. 405-418.
[78] Van Zeghbroeck, B. J., 1996, https://ecee.colorado.edu/~bart/book/eband3.htm
[79] Aouissi, M., Hamdi, I., Meskini, N., and Qteish, A., 2006, "Phonon Spectra of Diamond, Si, Ge, and Alpha-Sn: Calculations with Real-Space Interatomic Force Constants," PHYSICAL REVIEW B, 74(5).
[80] Galassi, M., and Gough, B., 2001, Gnu Scientific Library: Reference Manual, Network Theory, Bristol, UK.
[81] Vandebril, R., Barel, M. V., Mastronardi, N., and Proquest, 2008, Matrix Computations and Semiseparable Matrices, Johns Hopkins University Press, Baltimore.
[82] Aouissi, M., Hamdi, I., Meskini, N., and Qteish, A., 2006, "Phonon Spectra of Diamond, Si, Ge, Andα−Sn: Calculations with Real-Space Interatomic Force Constants," Physical Review B, 74(5).
[83] Sakurai, J. J., and Napolitano, J., 2011, Modern Quantum Mechanics, Addison-Wesley, Boston.
[84] Griffiths, D. J., 2013, Introduction to Quantum Mechanics, Pearson Education.
[85] Gautreau, P., Chu, Y., Ragab, T., and Basaran, C., 2015, "Phonon-Phonon Scattering Rates in Single Walled Carbon Nanotubes," Computational Materials Science.
[86] Pop, E., Sinha, S., and Goodson, K. E., 2006, "Heat Generation and Transport in Nanometer-Scale Transistors," Proceedings of the IEEE, 94(8), pp. 1587-1601.
[87] Lundstrom, M., 2011, Fundamentals of Carrier Transport (2nd Edition), Cambridge University Press, Cambridge, GBR.
[88] Giustino, F., 2016, "Electron-Phonon Interactions from First Principles."
[89] Liao, B., Qiu, B., Zhou, J., Huberman, S., Esfarjani, K., Chen, G., and Energy Frontier Research Centers . Solid-State Solar-Thermal Energy Conversion, C., 2015, "Significant Reduction of Lattice Thermal Conductivity by the Electron-Phonon Interaction in Silicon with High Carrier Concentrations: A First-Principles Study," Physical Review Letters, 114(11).
[90] Pop, E., Dutton, R. W., and Goodson, K. E., 2004, "Analytic Band Monte Carlo Model for Electron Transport in Si Including Acoustic and Optical Phonon Dispersion," Journal of Applied Physics, 96(9), pp. 4998-5005.
[91] Wang, J.-S., Agarwalla, B. K., Li, H., and Thingna, J., 2013, "Nonequilibrium Green's Function Method for Quantum Thermal Transport," Frontiers of physics, 9(6), pp. 673-697.
[92] Shomali, Z., Pedar, B., Ghazanfarian, J., and Abbassi, A., 2017, "Monte-Carlo Parallel Simulation of Phonon Transport for 3d Silicon Nano-Devices," International journal of thermal sciences, 114(pp. 139-154.
[93] Mittal, A., 2011, "Prediction of Non-Equilibrium Heat Conduction in Crystalline Materials Using the Boltzmann Transport Equation for Phonons," The Ohio State University / OhioLINK Dissertation.
[94] Chhabria, V. A., and Sapatnekar, S. S., "Impact of Self-Heating on Performance and Reliability in Finfet and Gaafet Designs," pp. 235-240.

[95] Pop, E., Dutton, R., and Goodson, K., "Thermal Analysis of Ultra-Thin Body Device Scaling [Soi and Finfet Devices]," pp. 36.6.1-36.6.4.
[96] Pop, E., 2014, "Monte Carlo Transport and Heat Generation in Semiconductors," Annual Review of Heat Transfer, 17(N/A), pp. 385-423.
[97] Ghatak, A. K., and Kothari, L. S., 1972, An Introduction to Lattice Dynamics, Addison-Wesley, London, Reading, Mass.,.
[98] Dolling, G., and Cowley, A., 1966, Proc. Proc. Phys. Soc. London.
[99] Mittal, A., and Mazumder, S., 2010, "Monte Carlo Study of Phonon Heat Conduction in Silicon Thin Films Including Contributions of Optical Phonons," Journal of Heat Transfer, 132(5), pp. 52402.
[100] Hao, Q., Zhao, H., and Xiao, Y., 2017, "A Hybrid Simulation Technique for Electrothermal Studies of Two-Dimensional Gan-on-Sic High Electron Mobility Transistors," Journal of Applied Physics, 121(20), pp. 204501.
[101] Glassbrenner, C. J., and Slack, G. A., 1964, "Thermal Conductivity of Silicon and Germanium from 3°K to the Melting Point," Physical review, 134(4A), pp. A1058-A1069.
[102] E, P., S, S., Dutton, R. W., and Goodson, K. E., 2006, "Non-Equilibrium Phonon Distributions in Sub-100 Nm Silicon Transistors," Journal of heat transfer, 128(7), pp. 638.